FIRST MEASUREMENT OF THE ISOSPIN-DEPENDENCE OF NUCLEAR STRUCTURE FUNCTIONS AT 12 GEV JEFFERSON LAB

Cameron William Cotton

Leesburg, Virginia

Bachelor of Science, University of Texas at Austin, 2019

A Dissertation presented to the Graduate Faculty

of the University of Virginia in Candidacy for the Degree of

Doctor of Philosophy

Department of Physics

University of Virginia

December 2024

Xiaochao Zheng, Chair

Alan Bergland

David Gaskell

Kent Paschke

First Measurement of the Isospin-Dependence of Nuclear Structure Functions at 12 GeV Jefferson Lab

Cameron William Cotton

(ABSTRACT)

The structure functions of protons and neutrons provide crucial insight into how the strong nuclear force, as described by Quantum Chromodynamics (QCD), manifests at everyday energies, allowing us to better understand precisely how quarks and gluons interact to form the basic building blocks of almost all visible mass in our universe. Despite more than 40 years of experimental and theoretical effort, the EMC effect – the observation that nuclear structure functions appear to be modified from those of free nucleons – is still not fully understood. One open question that remains is whether or not the modification of quark distributions is the same for all quark flavors. Determining the flavor (isospin) dependence of the EMC effect, which is predicted by several models, is essential for coming to a complete understanding of how QCD manifests in nuclei. To this end, inclusive electron Deep Inelastic Scattering (DIS) from nuclei with approximately constant atomic mass number A and variable proton-to-neutron ratio N/Z was measured in Jefferson Lab experiment E12-10-008 to look for isospin-dependent modification of nuclear structure functions. The preliminary EMC ratios presented here cover a kinematic range of $2.8 < Q^2 < 8.1$ GeV^2 and $0.18 < x_{Bj} < 1.0$. The size of the EMC effect in these nuclei is extracted by calculating the slope of the EMC ratio as a function of Bjorken x (x_{Bj}) over the ranges $0.3 < x_{Bj} < 0.6$ and $0.3 < x_{Bj} < 0.7$; these slopes then are compared with existing world data. Our preliminary results do not appear to indicate significant

isospin-dependence of the EMC effect, though a more careful study is needed once all results are confirmed.

Acknowledgments

This dissertation would not have been possible without the support of the many individuals who contributed both their time and expertise to its success. Therefore, I would like to start my dissertation by mentioning those individuals who have had a particularly large impact on me during my time as a physics student.

First, I would like to thank my parents, Neil and Sandra Cotton. For as long as I can remember, they have supported me and emphasized the importance of education, shaping me into the intellectually curious person I am today. I am also extremely grateful for having a wonderful high school physics teacher, Mr. Archie McHarg, whose passion for teaching physics inspired me to set out on this difficult yet rewarding path.

I would like to thank my Ph.D. advisor Prof. Xiaochao Zheng for the opportunity to join her research group and for allowing me to work on this exciting research topic. She was always available to give constructive feedback on my work and point me in the right direction. I would also like to thank my research committee members, Prof. Stefan Baessler and Prof. Dustin Keller, for providing valuable feedback on my progress and asking insightful questions about my research these past three years. I would also like to express my appreciation for my defense committee members, Prof. Alan Bergland and Prof. Kent Paschke, for their time and constructive feedback on my dissertation.

During my time at Jefferson Lab, which started in the wake of the COVID-19 pandemic in the summer of 2021, there were numerous individuals with whom I had the pleasure of working. I am thankful for everyone who took shifts during the XEM2 collaboration run period from Fall 2022 to Spring 2023, and all those who worked behind the scenes to keep CEBAF and Hall C up and running during that time. I had the good fortune to interact with many excellent graduate students, postdocs, staff scientists, and faculty from various institutions while at Jefferson Lab. I would like to thank the XEM2 postdocs, Burcu Duran, Tyler Hague, and Shujie Li for their contributions to ensuring the successful running of the XEM2 experiments.

I am grateful to have met Casey Morean and Bill Henry, who acted as my guides to Jefferson Lab and the surrounding area amid COVID-19. I would also like to thank Sebastian Seeds, with whom I enjoyed numerous thought-provoking discussions about physics, philosophy, and everything in between. I had the genuine pleasure of working alongside Dave Gaskell, who carried the burden of being my local mentor. I also had the privilege to work with John Arrington, who provided insightful and detailed feedback on my work throughout the analysis process. I would also like to thank Nadia Fomin for her many contributions during the running of the XEM2 experiments and analysis of our data. The input I have received from Dave, John, and Nadia, the XEM2 spokespeople, has undoubtedly saved me from weeks of going down countless rabbit holes and getting stuck at numerous dead-ends.

I have to stop somewhere, so finally I would like to thank my wife Gloria Kwon. For helping me pull my head out of a physics textbook every once in a while, I have her to thank for showing me that there is more to life outside of physics.

Contents

List of Figures

List of Tables

Chapter 1

Introduction

1.1 Overview

In 1983, the European Muon Collaboration (EMC) published results from their muon scattering measurements on ^{2}H and ^{56}Fe that were conducted at CERN. These results suggested that the internal structures of protons and neutrons (together referred to as nucleons) bound in nuclei are different than those of free nucleons [1]. This observation, now known as the EMC effect, was largely unexpected due to the relatively small energies that bind nucleons together. Consequently, this effect has been the subject of significant theoretical and experimental efforts to determine its underlying cause. Despite this effort, there is still no universally accepted fundamental explanation for the EMC effect. The work described in this dissertation details Jefferson Lab experiment E12-10-008 [2], which studied the EMC effect across a large number of nuclei by measuring inclusive electron scattering cross sections.

This dissertation is organized as follows: In Chapter 1 I provide an introduction to the physics of Deep Inelastic Scattering (DIS) in general, and the EMC effect in particular, with emphasis on providing brief historical and theoretical backgrounds for the EMC effect and highlighting several of the key goals of E12-10-008. Chapter 2 describes Jefferson Lab's Continuous Electron Beam Accelerator Facility (CEBAF), its experimental Hall C, and the High Momentum Spectrometer (HMS), which were used to carry out E12-10-008. Chapter 3 presents the data analysis procedure which consists of, but is not limited to, performing detector calibrations, executing Monte Carlo simulations, and extracting experimental cross sections. Chapter 4 presents a selection of preliminary results obtained from analysis of the data collected during this experiment. These include measurements of EMC ratios covering a kinematic range of $0.18 < x_{Bj} < 1.0$ and $2.8 < Q^2 < 8.1$ GeV^2 for ^{2}H, ^{12}C, ^{27}Al, ^{40}Ca, ^{48}Ca, ^{48}Ti, ^{54}Fe, ^{58}Ni, ^{64}Ni, and ^{197}Au. These results are then discussed, and several potential future measurements of the EMC effect are outlined.

1.2 Electron Scattering from Nuclei

Our universe is largely composed of protons and neutrons, which together account for over 99% of all visible mass. These subatomic particles, together referred to as "nucleons", are the building blocks of the atomic nucleus. These nucleons are in turn composed of even more fundamental particles known as quarks. Quarks possess color charge as well as conventional electric charge in units of 1/3 of the electron charge. Color charge is the charge of the strong interaction that binds quarks together into nucleons, with gluons acting as the force carrier. Unlike photons, which are the force carriers of the electromagnetic force but do not carry electric charge themselves, gluons carry color charge. This property of gluons causes the magnitude of the strong force between a pair of color-charged particles such as quarks to not diminish with distance like the Coulomb force. Rather, the energy contained in the gluon field between two color-charged particles continues to increase without leveling off as the separation increases between them. At some point, the energy contained in the gluon field becomes so great that a quark-antiquark pair is produced, with each new quark now pairing with one of the existing quarks. Due to this phenomenon, individual quarks cannot be observed in isolation under normal conditions, only being accessible at very high energy densities such as those present in the early universe or at high-energy colliders, where quark-gluon plasma (QGP) can be formed. The observation that quarks cannot be observed in isolation under “normal” conditions is one of the defining qualitative features of the strong interaction and is often referred to as color confinement, or simply confinement. Understanding confinement is one of the major unsolved problems of quantum chromodynamics (QCD), the fundamental theory that describes the strong interaction. Because of confinement, QCD at lower temperatures must be studied by looking into nucleons using methods such as muon or electron scattering.

Leptons, such as electrons and muons, are invaluable tools to study nuclear structure. As electrically charged point-like particles that do not participate in the strong interaction, a lepton’s interactions with nucleons and quarks are well described by quantum electrodynamics (QED) alone. Therefore, a high-energy electron beam such as the one produced by the Continuous Electron Beam Accelerator Facility (CEBAF) provides physicists with a surgical way to probe the internal structure of the atomic nucleus.

In typical electron scattering experiments such as those conducted at CEBAF, an electron from a high-energy beam interacts with an individual quark, nucleon, or nucleus in a given target material through the exchange of off-shell (virtual) photons or Z^0 bosons. In semi-inclusive or exclusive scattering experiments, some or all of the final state particles are measured. This includes the primary electron, the recoiling nucleus, and any other particles either created in the process or expelled from the nucleus during the interaction. In an inclusive scattering experiment, only the scattered electron is measured in the final state, effectively integrating over all possible final states of the recoiling nucleus and any other final state particles. The experiment discussed here primarily utilizes inclusive scattering measurements, so semi-inclusive

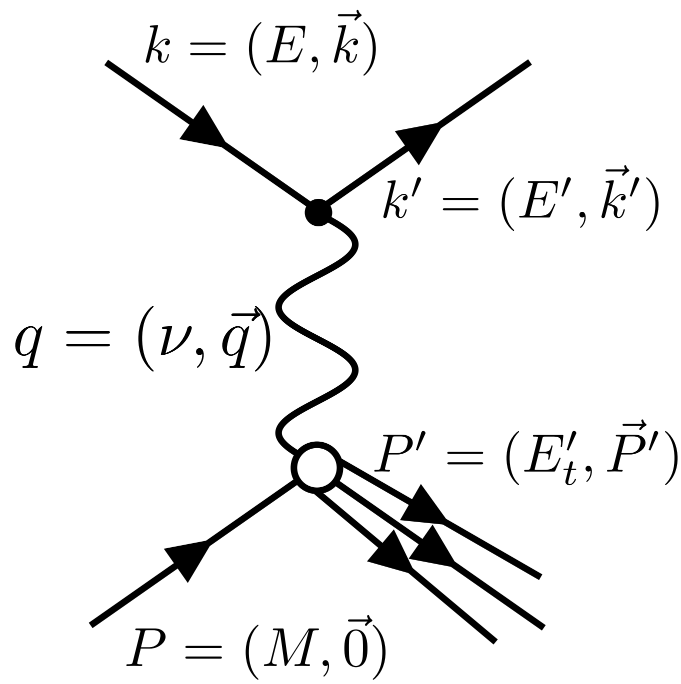

Figure 1.1: Leading order Feynman diagram for lepton scattering in the lab frame. Particles are labeled with their 4-vectors in the lab frame, where the target nucleon is taken to be at rest in the initial state.

and exclusive scattering will not be addressed further.

To the first order, electron scattering is well described by the Single Photon Exchange (SPE) approximation as illustrated in Fig. 1.1. The success of this approximation is due to the relatively weak strength of the electromagnetic (EM) interaction, which is quantified by the Sommerfeld or fine-structure constant $\alpha \approx \frac{1}{137}$. This causes all higher-order Feynman diagrams involving multiple photon exchanges to be heavily suppressed. Figure 1.1 also shows the momentum 4-vectors for the initial and final state particles in the lab (target-at-rest) frame. In this frame, the electron initially has 4-momentum k with energy E and 3-momentum $\vec{k}$ as it leaves the accelerator track and approaches the target. The electron then exchanges a virtual photon that has 4-momentum q with energy $\nu = E - E'$ and 3-momentum $\vec{q}$. The final state electron then moves off having a 4-momentum given by k' with energy E' and 3-momentum $\vec{k}'$. On the hadronic line of the Feynman diagram, the target nucleon starts at rest with a 4-momentum given by P, with a 3-momentum of $\vec{0}$, and energy equal to its rest mass M. The scattering may be elastic, in which case the recoiling hadron stays intact after the collision, or it may be inelastic, causing the hadron to fragment into multiple pieces. For the inclusive scattering experiment discussed here, we do not directly measure the final hadronic state; therefore, hadronic observables will not be covered in more detail.

Several important Lorentz invariant quantities can be derived from the 4-vectors shown in Fig. 1.1. First, Q^2 is the negative square of the 4-momentum of the exchanged virtual photon ($Q^2 \equiv -q^2$) and is known as its off-shellness or virtuality. This quantity is related to the spatial resolution of the interaction. Because Q^2 is related to spacial resolution and quarks are, to the best of our knowledge, point-like particles with no spacial structure, measured quantities such as quark momentum distributions exhibit little Q^2 dependence above a certain value. This is known as Bjorken Scaling and will be discussed in more detail later in this chapter. In the lab frame, Q^2 can be calculated using the equation

$$Q^2 = 2EE'(1 - \cos(\theta)) \ , \tag{1.1}$$

where θ is the scattering angle of the beam electron. Another key Lorentz invariant quantity is W^2, the square of the invariant mass of the final hadronic system, which includes all final state particles apart from the primary electron. W^2 loosely tells us whether our electron interacted with an individual quark, nucleon, or the target nucleus as a whole. It can be calculated using measured quantities from the electron

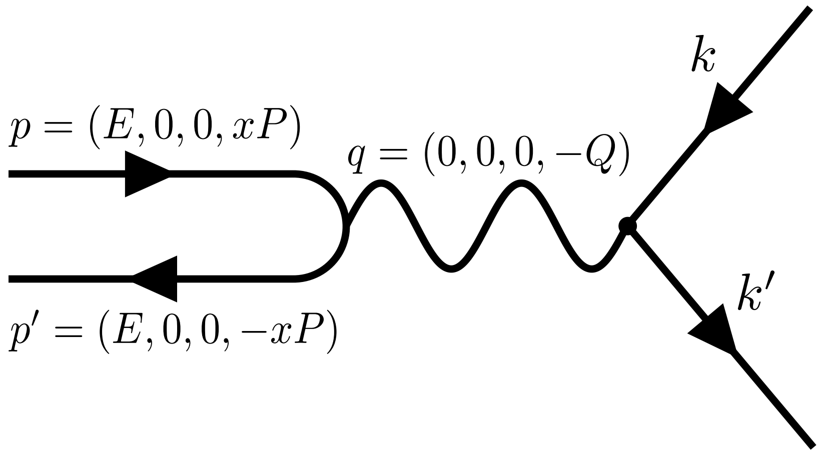

Figure 1.2: Leading order Feynman diagram for lepton scattering in the Breit frame. Particles are labeled with their 4-vectors in the Breit frame where the struck quark p has 3-momentum of magnitude xP along the z-axis, where $x = x_{Bj}$ is the fraction of the proton's total momentum carried by the struck quark, P is the total momentum of the proton, and E is the energy of the quark.

line of the Feynman diagram as

$$W^2 \equiv (P + q)^2 = M^2 + 2M\nu - Q^2. \tag{1.2}$$

Another reference frame that is useful for extracting meaningful physics quantities is known as the Breit frame, shown in Fig. 1.2. The Breit frame is the frame of reference in which the exchanged virtual photon only carries a 3-momentum vector and does not have any energy. This is a consequence of the exchanged virtual photon being space-like rather than time-like. Just as there is a rest (0-momentum) frame for every time-like ($Q^2 < 0$) particle, there is a 0-energy frame for every space-like ($Q^2 > 0$) particle. In this frame, there is an interesting variable known as Bjorken x (x or x_{Bj}). x_{Bj} can be interpreted as the fraction of the total momentum of a composite object (such as a nucleon) carried by the struck constituent (such as a quark) in the Breit frame.

Taking quarks to be point-like particles, the scattering process shown in Fig. 1.2 must be elastic. The equation for x_{Bj} can then be derived by first enforcing the elastic scattering condition

$$p'^2 = (p+q)^2 = p^2 + 2p \cdot q - Q^2 \rightarrow Q^2 = 2p \cdot q \ , \tag{1.3}$$

where where we used $p'^2 = p^2$ in the last step, as the invariant mass of the struck quark is constant. We now compare $p \cdot q$ to $x_{Bj} P \cdot q$, where P is the proton 4-momentum, E is the energy carried by the quark, and E_p is the total energy of the proton in the Breit frame:

$$p \cdot q = (E, 0, 0, x_{Bj} P) \cdot (0, 0, 0, -Q) = x_{Bj} PQ, \tag{1.4}$$

$$x_{Bj} P \cdot q = x_{Bj}(E_P, 0, 0, P) \cdot (0, 0, 0, -Q) = x_{Bj} PQ. \tag{1.5}$$

Noting that $p \cdot q$ is equivalent to $x_{Bj} P \cdot q$ in the Breit frame, we can insert $x_{Bj} P \cdot q$ into what we found in Eq. 1.3 and solve for x_{Bj}:

$$Q^2 = 2x_{Bj} P \cdot q \rightarrow x_{Bj} = \frac{Q^2}{2P \cdot q}. \tag{1.6}$$

In the fixed-target (lab) frame, this reduces to

$$x_{Bj} = \frac{Q^2}{2M\nu}. \tag{1.7}$$

In electron scattering experiments such as those carried out at CEBAF, four unique types of scattering processes are observed: Elastic, Quasielastic, Resonance, and Deep Inelastic (DIS). Depending on which region of kinematic space (see Fig. 1.3)

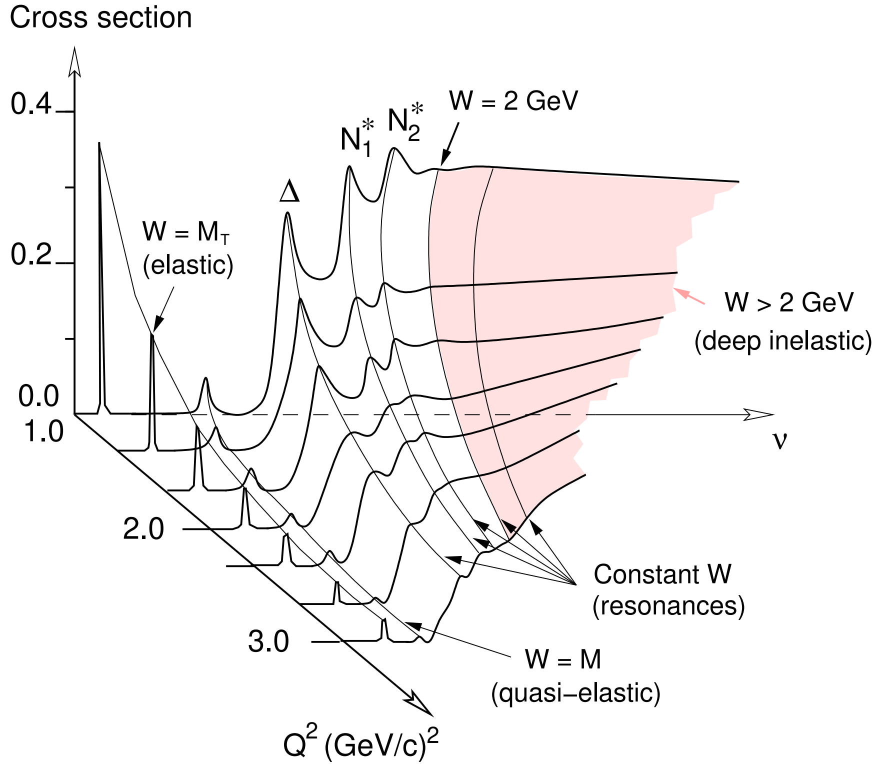

Figure 1.3: Figure from [3]. In arbitrary units, the inclusive electron scattering cross section parameterized as a function of ν and Q^2.

is being probed, one of the four processes will contribute the most to the measured cross section.

Elastic scattering describes the process in which an incoming electron interacts with the target nucleus as a whole, resulting in a scattered electron and an intact nucleus in the final state. This process predominantly occurs at low ν and Q^2, where the exchanged virtual photon does not carry enough energy to kick the bound nucleons out of the nucleus, and where the spatial resolution of the virtual photon is too coarse to discern individual nucleons.

On the other hand, quasielastic scattering occurs when the energy carried by the virtual photon exceeds the nuclear binding energy (but is not enough to put the nucleon's wave function into an excited state), allowing it to resolve individual nucleons. In this type of scattering, the incoming electron interacts with a nucleon in the target nucleus, kicking it out and causing the target nucleus to break into two or more fragments. Because nucleons are not at rest and exhibit significant motion about the nucleus's center of mass – known as Fermi Motion – the quasielastic peak shown in Fig. 1.3 is broadened relative to the elastic peak.

Resonance scattering occurs when the virtual photon transfers enough energy to an individual quark to put its nucleon's wave function into an excited state, causing the original nucleon to become a nuclear resonance. Resonance scattering can be identified by peaks in the cross section spectrum where the invariant mass of the final hadronic system is equal to the mass of one of these nuclear resonances (Δ, N_1^*, N_2^*, ...). These resonance peaks, shown in Fig. 1.3, sit on top of a large non-resonance inelastic background, which can make them difficult to identify amongst the growing inelastic cross section at larger W, especially at large Q^2. In addition, with only the final state of the electron measured, it is impossible to tell whether a particular electron was involved in a resonance or inelastic scattering process. Therefore, measurements of resonance scattering cross sections need to account for inelastically scattered electrons at the same kinematics, and vice versa. This cross-contamination of different scattering processes is present for all types of scattering when only inclusive measurements are made, as the final state of the hadronic system is not measured. However, the kinematic overlap between the resonance and inelastic contributions to the cross section is particularly significant.

Finally, DIS is typically defined by scattering at $W > 2$ GeV and $Q^2 > 1$ GeV^2. In this type of scattering, the exchanged virtual photon acts as a probe of the nucleon's internal structure, which is composed of partons (quarks and gluons). In this dissertation, we will be primarily concerned with quarks as they carry electric charge and therefore can interact with electrons via the electromagnetic interaction. Due to the large energies involved in DIS processes and the fact that the coupling strength of the strong interaction (α_s) decreases as the energy scale of the interaction increases, the quarks probed in these processes behave almost like free particles. This is a property of the strong interaction known as asymptotic freedom. Therefore, instead of being treated as a tightly bound object inside of a nucleon, the quark can be approximated as being "quasi-free" when dealing with high-energy scattering processes. Without asymptotic freedom, it would be much more difficult to interpret results from DIS data. As the focus of this dissertation is the EMC effect - the observation that quark momentum distributions appear to be modified in the nuclear environment - the remainder of this dissertation will be predominantly focused on DIS.

1.3 Deep Inelastic Scattering

Before delving further into DIS, it is beneficial to first briefly examine elastic scattering. Elastic scattering can be described in terms of a single degree of freedom. This means that given the initial state of a system, measuring just one kinematic parameter in the final state (e.g. θ or E') is sufficient to constrain all other final state parameters. Inclusive DIS is not as simple. Due to the unknown states of quarks inside the atomic nucleus, measurement of an additional degree of freedom is required in order to fully constrain the electron's final state. From an experimental point of view, this means that both the electron's scattering angle θ and energy E' must be measured to constrain all other kinematic parameters (Q^2, W^2). The DIS differential cross section can be written in natural units ($\hbar = c = 1$) as

$$\frac{d^2\sigma}{d\Omega dE'} = \frac{4\alpha^2 E'^2}{Q^4}\left[W_2(Q^2,\nu)\cos^2\left(\frac{\theta}{2}\right) + 2W_1(Q^2,\nu)\sin^2\left(\frac{\theta}{2}\right)\right] \ , \tag{1.8}$$

where α is the Sommerfeld (fine-structure) constant, and $W_1(Q^2, \nu)$ and $W_2(Q^2, \nu)$ are structure functions that contain information about the structure of the nucleon. This equation can also be written in terms of the Mott cross section,

$$\left(\frac{d^2\sigma}{d\Omega}\right)_{Mott} = \frac{4\alpha^2 E'^2 \cos^2\left(\frac{\theta}{2}\right)}{Q^4} , \tag{1.9}$$

which describes the scattering of relativistic electrons from a point-like and infinitely heavy target, as

$$\frac{d^2\sigma}{d\Omega dE'} = \left(\frac{d^2\sigma}{d\Omega}\right)_{Mott} \left[W_2(Q^2, \nu) + 2W_1(Q^2, \nu) \tan^2\left(\frac{\theta}{2}\right)\right] . \tag{1.10}$$

The structure functions $W_1(Q^2, \nu)$ and $W_2(Q^2, \nu)$ are commonly replaced by their dimensionless counterparts

$$F_1(x, Q^2) = MW_1(Q^2, \nu), \text{ and} \tag{1.11}$$

$$F_2(x, Q^2) = \nu W_2(Q^2, \nu), \tag{1.12}$$

which gives us

$$\frac{d^2\sigma}{d\Omega dE'} = \frac{4\alpha^2 E'^2}{Q^4} \left[\frac{1}{\nu} F_2(x, Q^2) \cos^2\left(\frac{\theta}{2}\right) + \frac{2}{M} F_1(x, Q^2) \sin^2\left(\frac{\theta}{2}\right)\right] . \tag{1.13}$$

As previously mentioned, for scattering in the limit of large ν and Q^2, one would expect that the participating quark can be treated as independent from the rest of the nucleon during the scattering process due to the large energies involved. This limit where $\nu,\ Q^2 \to \infty$ is known as the Bjorken limit. Therefore, in the Bjorken limit, we should be able to treat the quark as a "quasi-free" point-like spin 1/2 particle. It is then interesting to compare Eq. 1.13 to the equation for scattering from an independent point-like spin 1/2 particle

$$\frac{d^2\sigma}{d\Omega dE'} = \frac{4\alpha^2 E'^2}{Q^4}\left[\cos^2\left(\frac{\theta}{2}\right) + \frac{Q^2}{2M^2}\sin^2\left(\frac{\theta}{2}\right)\right]\delta\left(\nu - \frac{Q^2}{2M}\right), \tag{1.14}$$

where the delta function is introduced due to the differentiation with respect to E' and requiring the elastic scattering condition. Comparing Eqs. 1.13 and 1.14 and writing the delta functions in a more suggestive form, we find for an independent stationary spin 1/2 particle that the structure functions can be written as

$$F_2 = \delta\left(1 - \frac{Q^2}{2M\nu}\right) \text{ and} \tag{1.15}$$

$$2F_1 = \frac{Q^2}{2M\nu}\delta\left(1 - \frac{Q^2}{2M\nu}\right). \tag{1.16}$$

Using Eq. 1.7 to simplify Eqs. 1.15 and 1.16, we find that this "quasi-free" treatment of quarks allows the structure functions to be parameterized by a single variable, x_{Bj}, rather than by ν and Q^2 independently. In this framework, one also finds, for nucleons composed of spin 1/2 particles, that their F_1 and F_2 structure functions are no longer independent. Replacing the mass M of the point-like spin 1/2 particle with the nucleon mass M_N multiplied by the momentum fraction of the quark in the Breit frame ($M \to M_N \cdot x_{Bj}$, which also results in $F_1 \to F_1 \cdot x_{Bj}$), one finds that the F_1 and F_2 structure functions are connected by the Callan-Gross relation,

$$F_2 = 2x_{Bj}F_1. \tag{1.17}$$

Early results confirmed these predictions, showing that for a given value of x_{Bj}, the F_1 and F_2 structure functions are nearly constant at large Q^2 [4][5] as shown in Fig. 1.4, a phenomenon known as Bjorken Scaling [6], and that they satisfy the Callan-Gross

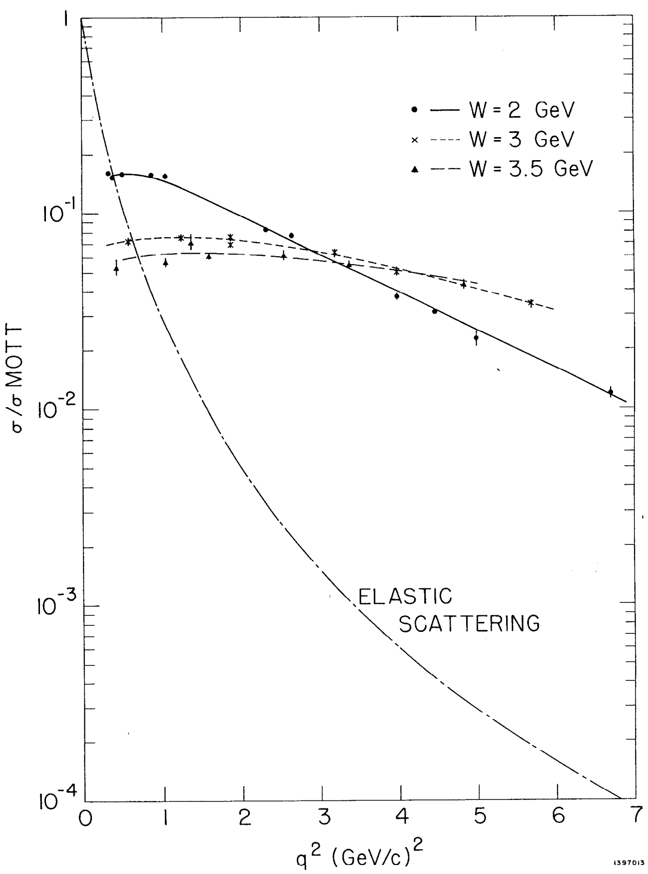

Figure 1.4: Figure from [4]. Measured inelastic cross sections divided by Mott cross sections for $W = 2$, $W = 3$, and $W = 3.5$ from SLAC, shown alongside elastic scattering cross sections. The inelastic cross sections show little q^2 dependence when compared with the elastic scattering cross section, serving as evidence of Bjorken Scaling.

relation. While the scaling is not perfect due to higher-twist effects and the running strong coupling constant $\alpha_s(Q^2)$, these were some of the first pieces of evidence to support the claim that nucleons are comprised of point-like spin 1/2 quarks.

In the parton model, a nucleon's structure can be described in terms of the longitudinal momentum distributions of its constituent partons. Therefore, the F_1 and F_2 structure functions can be decomposed and written in terms of a more fundamental quantity, parton distribution functions (PDFs). Today, we know that partons can be divided into two categories: electrically charged quarks, and electric charge-neutral gluons which act as the carriers of the strong force. As the cross section for electromagnetic scattering scales with the square of a particle's electric charge, we can treat the F_2 structure function as a simple charge-squared and x_{Bj} weighted sum of individual quark and antiquark PDFs, written as

$$F_2 = x_{Bj} \sum e_q^2 [q(x_{Bj}) + \bar{q}(x_{Bj}))], \tag{1.18}$$

where e_q is the charge carried by a given quark flavor and q and $\bar{q}$ are the quark and anti-quark PDFs, respectively. We can then apply the Callan-Gross relation to find

$$F_1 = \frac{1}{2} \sum e_q^2 [q(x_{Bj}) + \bar{q}(x_{Bj})]. \tag{1.19}$$

In preparation for discussing the EMC effect, we will examine how measured cross sections can be used to compare the structure functions of different nuclei. Using Eq. 1.13 and denoting the per-nucleon cross section for a given nucleus with A nucleons to be σ_{A_n}, we see the ratio of cross sections is given as

$$\frac{\sigma_{A_2}}{\sigma_{A_1}} = \frac{F_2^{A_2}}{F_2^{A_1}} \frac{\left[1 + 2\frac{\nu F_1^{A_2}}{M F_2^{A_2}} \tan^2 \frac{\theta}{2}\right]}{\left[1 + 2\frac{\nu F_1^{A_1}}{M F_2^{A_1}} \tan^2 \frac{\theta}{2}\right]}. \tag{1.20}$$

F_1/F_2 can be written in terms of the ratio $R = \frac{\sigma_L}{\sigma_T}$, where $\sigma_{L(T)}$ is the longitudinal (transverse) virtual photon cross section. We first write the total differential cross section in terms of the virtual photon cross sections as

$$\frac{d^2\sigma}{d\Omega dE'} = \Gamma[\sigma_T(x_{Bj}, Q^2) + \epsilon\sigma_L(x_{Bj}, Q^2)] = \Gamma\sigma_T(x_{Bj}, Q^2)[1 + \epsilon R(x_{Bj}, Q^2)], \tag{1.21}$$

where Γ is the total flux of virtual photons given by

$$\Gamma = \frac{\alpha E'(W^2 - M^2)}{4\pi^2 Q^2 M E(1-\epsilon)}, \tag{1.22}$$

and ϵ is the ratio of longitudinal to transversely polarized virtual photons given by

$$\epsilon = \frac{\Gamma_L}{\Gamma_T} = \left[1 + 2\left(1 + \frac{\nu^2}{Q^2}\right)\tan^2\frac{\theta}{2}\right]^{-1}. \tag{1.23}$$

Now, we find that the ratio R can be written in terms of F_1 and F_2 as

$$R = \frac{\sigma_L}{\sigma_T} = \frac{MF_2}{\nu F_1}\left(1 + \frac{\nu^2}{Q^2}\right) - 1, \text{ therefore} \tag{1.24}$$

$$\frac{\nu F_1}{MF_2} = \frac{1 + \frac{\nu^2}{Q^2}}{R+1}. \tag{1.25}$$

Plugging this into 1.20, we find that

$$\frac{\sigma_{A_2}}{\sigma_{A_1}} = \frac{F_2^{A_2}(1+\epsilon R_{A_2})(1+R_{A_1})}{F_2^{A_1}(1+\epsilon R_{A_1})(1+R_{A_2})}. \tag{1.26}$$

This means that the per-nucleon cross section ratio is only dependent upon the structure function ratio and $R_{A_{1(2)}}$. Although studies of the nuclear dependence of R are still ongoing, early measurements at SLAC [7][8] found R to be the same between different nuclei within uncertainty. While some recent results have hinted at a possible nuclear dependence of R [9], no significant deviation has been found in recent data. Therefore, it has historically been taken that the F_2 structure function ratio can be determined directly from a measurement of the cross section ratio by setting $R_{A_1} = R_{A_2}$ in Eq. 1.26, giving

$$\frac{\sigma_{A_2}}{\sigma_{A_1}} = \frac{F_2^{A_2}}{F_2^{A_1}}. \tag{1.27}$$

Using the Callan-Gross relation, the F_1 structure function could just as well be substituted into this equation in place of F_2. However, as can be seen in Eq. 1.13, in fixed-targets experiments with detectors at far-forward (small) angles, the F_2 structure function contributes significantly more to the measured cross section than F_1. Therefore, the measured cross section ratios in these experiments are generally equated to the F_2 structure function ratio rather than the F_1 structure function ratio.

1.4 Discovery of the EMC Effect

In the atomic nucleus, the binding energies of nucleons are typically on the order of a few MeV and their Fermi momenta are on the order of a few hundred MeV. Both of these energies are significantly smaller than the typical energies involved in DIS interactions, with some of the earliest experiments using beams with energies exceeding 100 GeV. Therefore, neglecting the effects of Fermi motion, one would expect that the measured structure function of a nucleus could be reasonably well approximated by the sum of the free structure functions of its constituents, allowing one to construct the equation

$$F_2^A = ZF_2^p + NF_2^n, \tag{1.28}$$

where Z and N are the numbers of protons and neutrons in the nucleus, respectively. To account for nuclear effects, one can perform a convolution of the Fermi motion of nucleons with the motion of quarks, described by structure functions. This convolution results in kinematic smearing of the observed structure functions. More concretely, when comparing the per-nucleon structure function of a nucleus with that of its free counterparts, this kinematic smearing results in a x_{Bj} dependent per-nucleon

J.J. Aubert *et al.*, Phys. Lett. B **123**, 275-278 (1983).

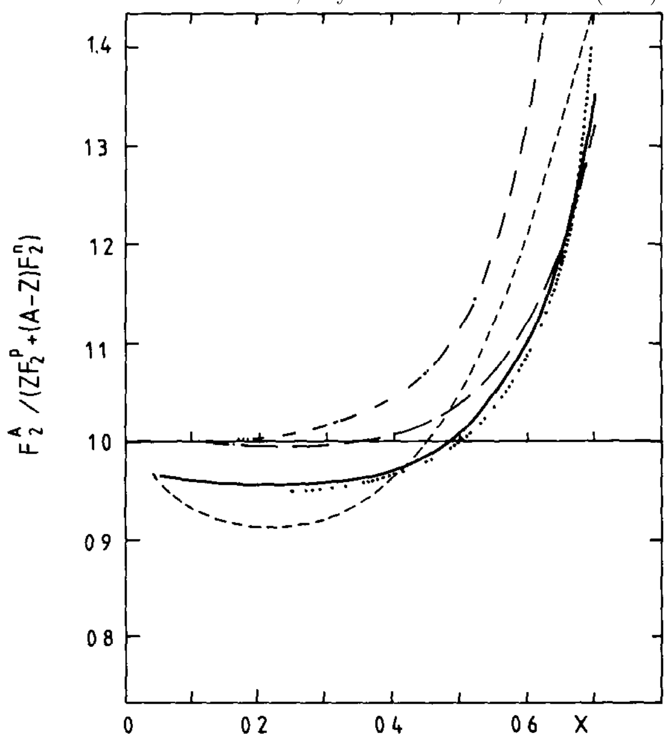

Figure 1.5: Figure from [1]. Theoretical predictions for the per-nucleon structure function ratio between iron and its free constituents due to Fermi motion. The prediction from the few-nucleon-correction model of Frankfurt and Strickman is given by the dotted line [10]. The prediction from the collective-tube model of Berlad et al. is given by the dashed line [11]. The solid line gives the prediction from Bodek and Ritchie [12]. The dot-dashed and triple-dot-dashed lines are also calculations from Bodek and Ritchie, however, they are not predictions and only serve as a measure of the sensitivity of their prediction to assumptions that are poorly understood.

cross section ratio shown in Fig. 1.5.

However, when the European Muon Collaboration (EMC) measured ^{56}Fe and ^{2}H cross sections using their muon beam and took the ratio between the two, they found that the shape of the per-nucleon cross section distribution was different than predicted [1]. Instead of finding the per-nucleon cross section ratio to be approximately unity at low x_{Bj} and to gradually rise due to Fermi motion at large x_{Bj}, they found the cross section ratio to be nearly 1.15 around $x_{Bj} = 0.1$ and to decrease linearly up

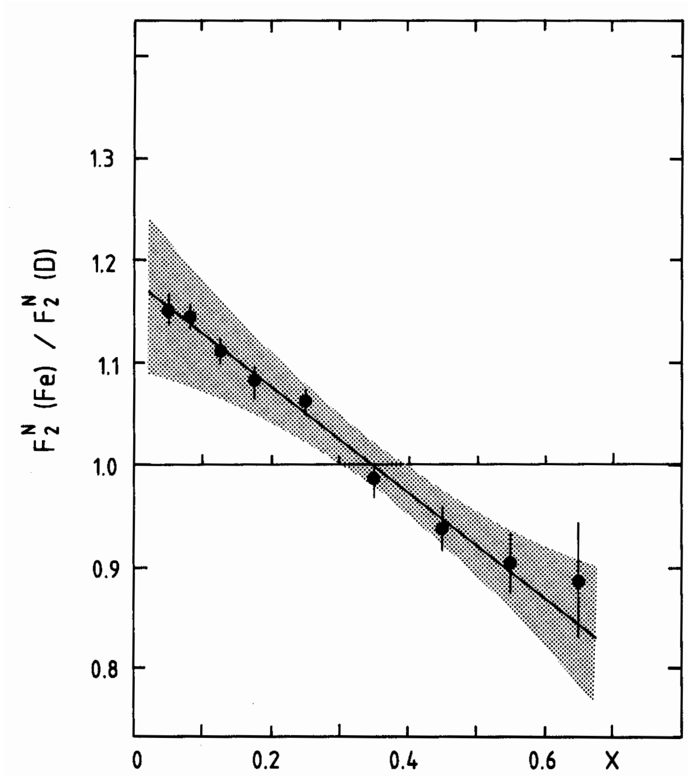

Figure 1.6: Figure from [1]. The measured ratio of the per-nucleon structure function for ^{56}Fe and ^{2}H. The statistical uncertainty is given by the error bars, while the shaded region indicates systematic uncertainty. Results are corrected for the non-isoscalarity of ^{56}Fe to account for the difference between F_2^n and F_2^p. This result was in stark contrast to the theoretical predictions of the day as shown in Fig. 1.5.

to x_{Bj} of approximately 0.7, shown in Fig. 1.6.

This phenomenon, today known as the EMC effect, is often characterized by the approximately linear region of the per-nucleon DIS cross section ratio in the range $0.3 < x_{Bj} < 0.7$, though the exact limits can vary slightly. In addition, the region of enhancement of the per-nucleon cross section ratio around $x_{Bj} \approx 0.2$ is known as the anti-shadowing region. Although the first results showing the EMC effect were published in 1983 and our understanding of nuclear structure has expanded dramatically over the past four decades, there is still no generally accepted explanation for what causes the EMC effect.

To come to a better understanding of the origin of the EMC effect, one can look at how the size of the EMC effect varies across different nuclei. The most commonly used metric to quantify the magnitude of the EMC effect is the "EMC slope". This is defined as the magnitude of the slope of the per-nucleon DIS cross section ratio roughly in the range $0.3 < x_{Bj} < 0.7$, written as $|dR_{EMC}/dx|$. This definition relies on the fact that the shape of the EMC effect is the same across all nuclei and that the slope in this range is relatively constant for a given nucleus.

1.5 Previous Measurements

Since the discovery of the EMC effect in 1983, a number of additional experiments have been performed to verify and expand upon the original measurement. This section will provide an overview of several of these experiments and discuss some of the impact they had on our understanding of nuclear structure and the EMC effect.

1.5.1 European Muon Collaboration

Following up on their 1983 publication, in 1988 the European Muon Collaboration published new results, shown in Fig. 1.7, for the per-nucleon cross section ratio of three additional nuclei: C, Cu, and Sn [13]. This experiment collected data covering a kinematic range of $5 < Q^2 < 35$ GeV^2 and $0.03 < x_{Bj} < 0.7$ and confirmed the result from the 1983 paper that nucleon structure functions in nuclei differ from those of free nucleons. However, in (slight) tension with the 1983 paper, but in agreement with results since then, they found a smaller enhancement of the per-nucleon cross section in the anti-shadowing region. In addition, by collecting data at kinematics extending all the way down to $x_{Bj} = 0.03$, they found that the cross section ratio falls below unity for $x_{Bj} \lesssim 0.05$, a phenomenon known as shadowing. The shadowing

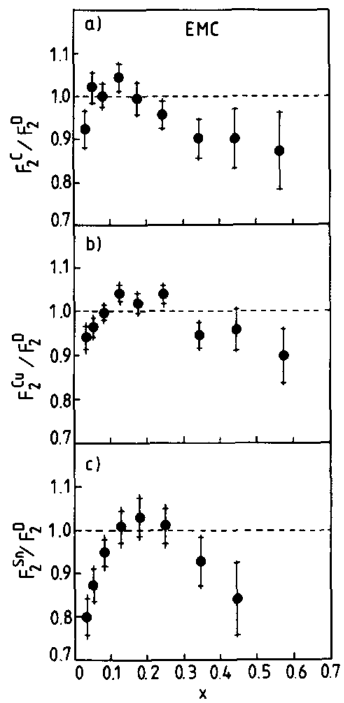

Figure 1.7: Figure from [13]. Measurements of the structure function ratio for Sn, Cu, and C are shown with statistical (inner bars) and total uncertainties. For all nuclei, there is a clear suppression of the structure function ratio at small x_{Bj}. This effect is most prominent for Sn, the largest nucleus studied. This supports the hypothesis that this effect is due to shadowing, as the ratio of inner nucleons to surface nucleons increases with the size of the nucleus.

effect at low x_{Bj} is most prominent in large nuclei, where the outer nucleons act as a shield for the inner nucleons. This causes a relative drop in the cross section due to the inner nucleons being in the "shadow" of the dense sea quark distributions at low x_{Bj} of the outer nucleons. Because this experiment was conducted at $Q^2 > 5$ GeV^2, this result suggested that the observed shadowing was due to partons as opposed to nucleons as a whole. The tension between these results and results from their 1983 paper at low x_{Bj} is commonly attributed to uncertainties in the radiative corrections procedure used in the analysis of the data published in 1983.

1.5.2 BCDMS

Only two years after the discovery of the EMC effect in 1983, the BCDMS collaboration published structure function ratios from their own deep inelastic muon scattering experiment [14]. They measured ^{2}H, N, and Fe cross sections with a kinematic coverage of $26 < Q^2 < 200$ GeV^2 and $0.2 < x_{Bj} < 0.7$ for N and $46 < Q^2 < 200$ GeV^2 and $0.08 < x_{Bj} < 0.7$ for Fe. They built upon the original result as they were able to put more precise systematic constraints on their data. Shadowing at low x_{Bj} was observed, and the structure function ratios showed no Q^2 dependence over the kinematic range studied.

1.5.3 New Muon Collaboration

In many experiments studying the EMC effect, the ^{2}H cross section is used in the denominator of the EMC ratio in place of the free proton and neutrons cross sections. This is primarily because free neutrons are unstable and therefore difficult to measure in isolation. To work around this experimental difficulty, ^{2}H is used because, as a weakly bound nuclear system, its constituent nucleons can be treated as quasi-free. However, as weakly bound as ^{2}H is, its cross section is still slightly different than the sum of its constituents due to nuclear effects. To quantify this difference, the New Muon Collaboration measured F_2^d/F_2^p, the ratio of the deuteron and proton structure function [15]. This was then used to perform a model-dependent extraction of the ratio of proton and neutron structure functions F_2^n/F_2^p, a quantity that must be known to high precision to study non-isoscalar nuclei which is discussed further in Sec. 3.17. Using muon beams with energies of 90, 120, 200, and 280 GeV, their data covered a wide kinematic range from $0.2 < Q^2 < 245$ GeV^2 and $0.001 < x_{Bj} < 0.8$. In their analysis, they did not observe any shadowing in the ratio of F_2^n/F_2^p. In addition, they found no Q^2 dependence of F_2^n/F_2^p at small x_{Bj} and a small Q^2 dependence of F_2^n/F_2^p at large x_{Bj}.

Along with their measurement of F_2^n/F_2^p, the New Muon Collaboration conducted several experiments to measure the structure function ratios of other nuclei. They first published the structure function ratios $F_2^{\mathrm{He}}/F_2^{\mathrm{D}}$, $F_2^{\mathrm{C}}/F_2^{\mathrm{D}}$, and $F_2^{\mathrm{Ca}}/F_2^{\mathrm{D}}$ covering the kinematic range $0.0035 < x < 0.65$ and $0.5 < Q^2 < 90$ GeV^2 using a 200 GeV muon beam [16]. Shortly thereafter, they published the structure function ratios $F_2^{\mathrm{C}}/F_2^{\mathrm{Li}}$, $F_2^{\mathrm{Ca}}/F_2^{\mathrm{Li}}$, and $F_2^{\mathrm{Ca}}/F_2^{\mathrm{C}}$ covering the kinematic range $0.0085 < x < 0.6$ and $0.8 < Q^2 < 17$ GeV^2 utilizing a 90 GeV muon beam [17]. These datasets were later reanalyzed to apply corrections for the ^{2}H target masses and to improve radiative corrections [18]. While both of these experiments collected data covering significant portions of the nominal EMC effect kinematic region ($0.3 < x_{Bj} < 0.7$), the precision of the data in this region was limited.

An additional study was conducted with seven different nuclear targets, covering a kinematic range of $2 < Q^2 < 70$ GeV^2 and $0.01 < x_{Bj} < 0.8$ using a 200 GeV muon beam [19] to investigate the kinematic and A dependence of nuclear structure functions. They found that the structure function ratio had a universal qualitative dependence on x_{Bj} for all nuclei studied. Their results also showed that nuclear shadowing scales with A, as previously observed.

1.5.4 SLAC

In response to the observation of the nuclear dependence of structure functions by the European Muon Collaboration in 1983, an analysis of existing DIS data collected at SLAC was performed to extract cross section ratios of Al and Fe (steel) to ^{2}H [20] [21]. The existing data was collected using an electron beam with energies between

4.5 and 20 GeV. These measurements, which had a Q^2 coverage of $2 < Q^2 < 20$ for aluminum and $3 < Q^2 < 20$ for iron, were found to be in good agreement with the EMC results. This served as a test of the Q^2 dependence of the EMC effect and as a high-precision validation of the original observation of the EMC collaboration.

A dedicated measurement of the A-dependence of the EMC effect was then performed at SLAC with experiment E139. Preliminary results were reported in 1984 [22], with final results later published that included an improved radiative corrections procedure [23]. To study the A-dependence of the EMC effect, E139 measured DIS cross sections of nine different nuclei including ^{2}H, ^{4}He, Ag, and Au. These cross sections were measured using an electron beam with energies between 8 and 24.5 GeV and covered a wide kinematic range of $0.089 < x_{Bj} < 0.8$ and $2 < Q^2 < 15$ GeV^2. Unlike other measurements at the time, this dataset included high-precision measurements of cross section ratios at large x_{Bj}, where the effects of Fermi motion have the largest impact. In agreement with previous measurements, the size of the EMC effect was found to scale approximately logarithmically with A, with the exception of ^{4}He.

1.5.5 HERMES

The HERMES collaboration at DESY used a 27.5 GeV positron beam to measure DIS cross section ratios of ^{3}He, ^{14}N, and ^{84}Kr with respect to ^{2}H covering the kinematic range of $0.010 < x_{Bj} < 0.65$ and $0.5 < Q^2 < 15$ GeV^2 [24] [25]. The first published cross section ratios appeared to suggest a nuclear dependence of R, the ratio of the cross sections of longitudinal and transverse photons. However, upon further analysis, it was found that the apparent nuclear dependence of R was in fact due to previously unrecognized instrumental and radiative effects. Accounting for these effects, the corrected results were consistent with R having no nuclear dependence.

1.5.6 Jefferson Lab

Several key experiments probing nuclear structure functions have been performed utilizing the high-luminosity electron beam at Jefferson Lab. Experiment E89-008 measured cross section ratios of C, Fe, and Au to ^{2}H in the resonance region ($1.2 < W^2 < 3$ and $Q^2 \approx 4$ GeV^2) [26], allowing for comparison with existing measurements of cross section ratios in the DIS region. The measured cross section ratios were parameterized in terms of the Nachtmann variable ξ, given by

$$\xi = \frac{2x_{Bj}}{1 + \sqrt{1 + 4M^2 x_{Bj}^2 / Q^2}} \, . \tag{1.29}$$

ξ was used as opposed to x_{Bj} to account for target mass corrections at finite Q^2. Note that, in the Bjorken limit ($Q^2 \to \infty$), the Nachtmann variable ξ reduces to x_{Bj}. It was found that the measured cross section ratios from the lower-energy resonance data were consistent with existing higher-energy DIS data as shown in Fig. 1.8, indicating that the nuclear effects are the same in both kinematic regions. This observation can be understood through the lens of quark-hadron duality, where structure functions in both the resonance and DIS regions exhibit the same behavior in perturbative QCD.

Experiment E03-103 at Jefferson Lab measured the EMC effect in ^{3}He, ^{4}He, Be, C, Cu, and Au in the range $0.3 < x_{Bj} < 0.9$ and $Q^2 \approx 3$–6 GeV^2 [29] [30]. This experiment placed particular emphasis on light nuclear targets (A<12), for which little experimental data were available at the time. Light nuclear targets are of particular interest as they are more amenable to comparison with theoretical calculations due to having fewer constituent nucleons and the availability of “exact” Green’s Function Monte Carlo (GFMC) calculations. In addition, due to the lack of available precision data, it was unknown whether the shape of the EMC effect would be the same in

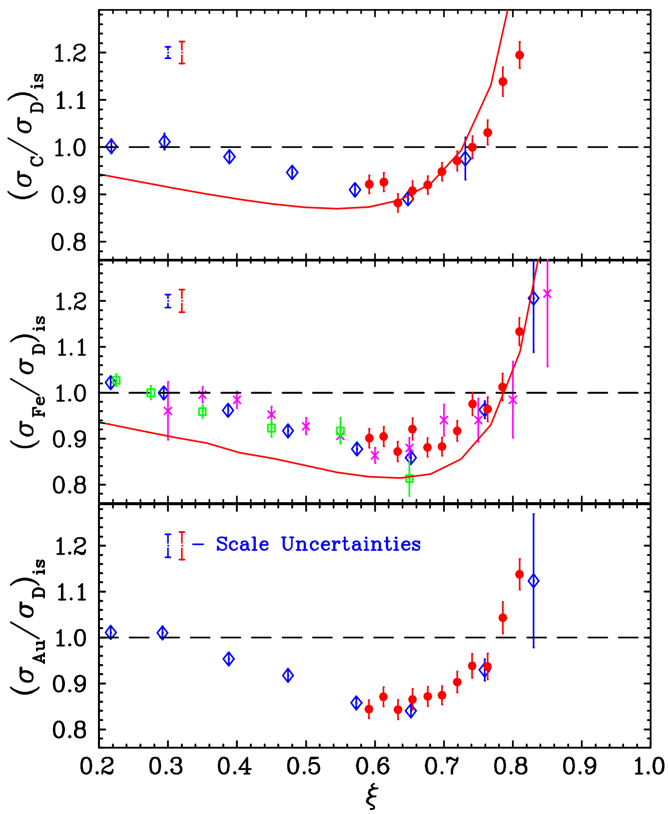

Figure 1.8: Figure from [26]. Isoscaler corrected per-nucleon cross section ratios as a function of the Nachtmann variable ξ. Cross section ratios measured in the resonance region at Jefferson Lab (red circles) [26] are shown alongside DIS results from SLAC E139 (blue diamonds) [23], SLAC E87 (magenta crosses) [20], BCDMS (green squares) [27], and an updated version of the calculations from Ref. [28] which include the contributions of nuclear binding effects on nuclear structure functions (red curves).

light nuclei as it was in heavier nuclei. Also, due to the complex relationship between nuclear mass and nuclear density (ρ) in light nuclei, mass and density-dependent fits to the EMC effect make markedly different predictions for the magnitude of nuclear modification in these nuclei. For example, despite having three times as many nucleons, ^{9}Be has an average nuclear density similar to that of ^{3}He. For these reasons, light nuclei provided a particularly enticing environment in which to make new measurements of the EMC effect.

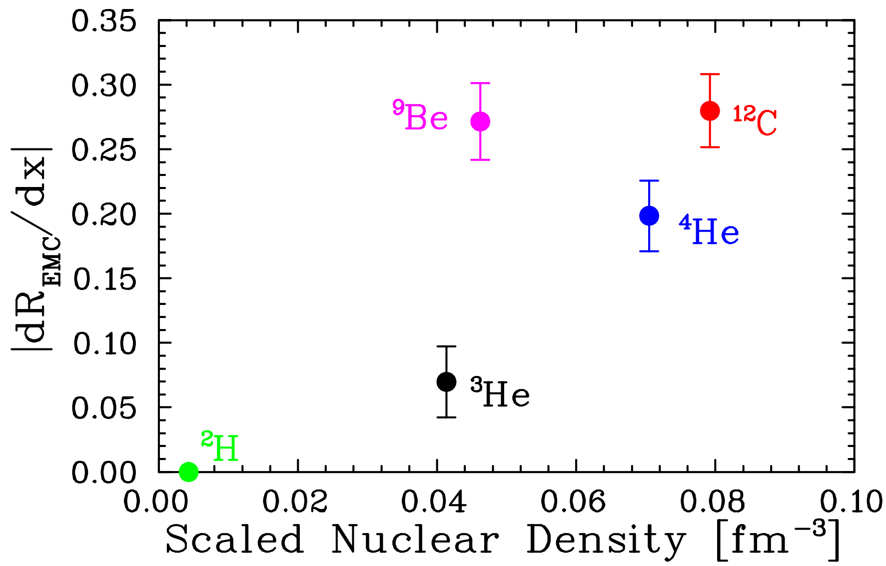

Figure 1.9: Figure from [29]. Results for the size of the EMC effect in the nuclei studied in experiment E03-103. The large EMC effect in ^{9}Be compared to ^{3}He and ^{4}He suggested that the EMC effect may be driven by local nuclear density as opposed to average nuclear density.

It was found that neither mass nor average density dependent fits could describe the data, particularly due to ^{9}Be which, despite having a lower average density, was found to have a larger EMC effect than ^{4}He as shown in Fig. 1.9. One possible explanation of the ^{9}Be data is that the EMC effect is driven by local density rather than average density. Because ^{9}Be can be viewed as a pair of dense α particles with one additional neutron, the density "seen" by the average nucleon is much greater than the average density of the entire nucleus due to the empty space between the alpha clusters. Therefore, these results for the EMC effect in light nuclei are consistent with the hypothesis that the EMC effect scales with local density rather than average density.

As data for this experiment was collected at lower energies than previous experiments, several measurements were made at different Q^2 values to verify that the results were Q^2 independent. As shown in Fig. 1.10, no systematic Q^2 dependence

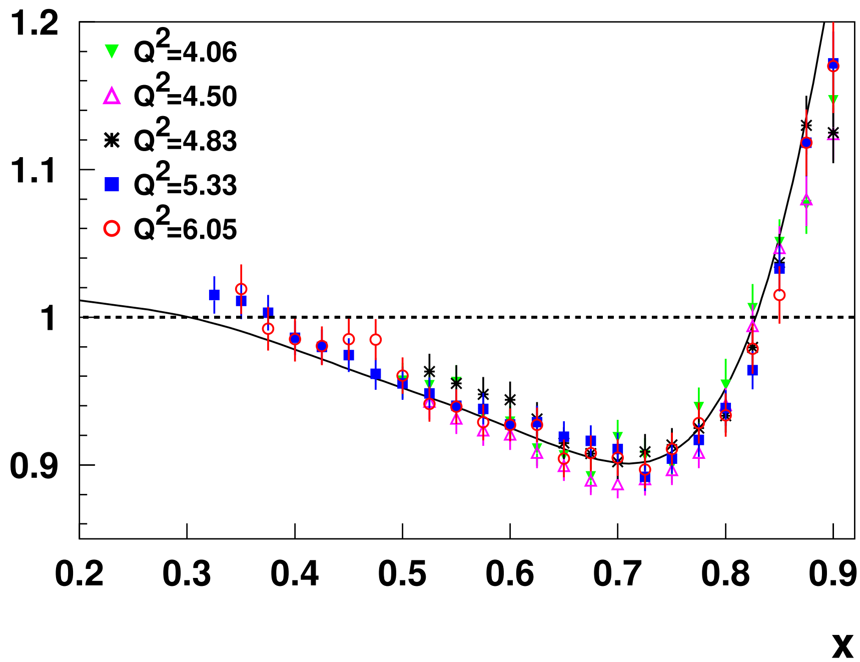

Figure 1.10: Figure from [29]. Carbon EMC Ratios for the 5 highest Q^2 bins from experiment E03-103. For $Q^2 > 4$ GeV^2, no Q^2 dependence was observed.

was found in the highest Q^2 data taken. However, Q^2 dependence *was* observed for settings where Q^2 was below approximately 3 GeV^2 and $x_{Bj} > 0.6$. These kinematics correspond to values of W^2 below $2-3$ GeV^2, where contributions due to resonances become significant.

The commissioning run of experiment E12-10-008 at Jefferson Lab measured the EMC effect in ^{9}Be, ^{10}B, ^{11}B, and ^{12}C using a 10.6 GeV electron beam. This corresponds to a kinematic coverage of $0.3 < x_{Bj} < 0.95$ and $4.3 < Q^2 < 8.3$ GeV^2 [31]. It was found that the sizes of the EMC effect in the boron isotopes ^{10}B and ^{11}B were similar to that of ^{4}He, ^{9}Be, and ^{12}C. Similarly to ^{9}Be, the boron isotopes can be seen as two dense α particles plus two or three additional nucleons. Therefore, by the same argument that was made for the ^{9}Be result from E03-103, these results further supported the idea that the EMC effect is driven by local, rather than average, nuclear density.

1.6 Models of an Isospin-Dependent EMC Effect

The flavor or isospin dependence of the EMC effect, that is, how the PDFs of different flavors of quarks are modified in the nuclear environment, can be measured to gain a deeper understanding of the origin of the EMC effect. There are numerous mechanisms by which the PDFs of up and down quarks could be modified differently in nuclei. Even simple models including only Fermi motion would predict some isospin-dependent nuclear modification due to the difference in the x_{Bj} distributions of up and down quarks. Despite this, isospin-dependent modification is typically not incorporated into models of nuclear PDFs. This is partially due to the lack of available data that is sensitive to isospin dependence. For light nuclei, it is difficult to discern any isospin-dependent nuclear modification from the existing data due to the fact that the size of the EMC effect in light nuclei is also highly sensitive to the details of the structure of the nucleus, which are poorly understood. On the other hand, for heavy nuclei, N/Z is highly correlated with A, making it difficult to distinguish between the impacts of A-dependent and isospin-dependent effects in many of these nuclei as well.

Despite these difficulties, a description of how isospin-dependent effects influence the modification of nuclear PDFs is necessary to come to a complete understanding of the EMC effect. In addition, an accurate description of the isospin-dependence of the EMC effect will allow for a more accurate determination of nuclear PDFs, which are essential to be able to reliably interpret results from measurements of processes involving the weak interaction such as neutrino DIS, as they are more directly impacted by quark flavor.

The following sections will cover a few models that predict isospin-dependent modification of nuclear PDFs.

1.6.1 CBT Model

One set of calculations predicting an isospin-dependent EMC effect is known as the Cloet-Bentz-Thomas (CBT) model [32]. In their calculations, for non-isoscalar nuclei, the isovector-vector mean field (ρ^0) couples to the quarks inside of the bound nucleons. In N>Z nuclei, this causes the up quarks to feel a small additional attraction and down quarks to feel a small additional repulsion in the mean field, producing an isospin-dependent modification of the nuclear PDFs as shown in Fig. 1.11. These calculations were performed within the framework of the Nambu-Jona-Lasino model, a low-energy QCD chiral effective field theory characterized by a 4-fermion contact interaction between the quarks [33] [34].

The CBT model calculations of nuclear PDFs were then applied to a reanalysis of the NuTeV extraction of the Weinberg or weak mixing angle, specifically $\sin^2(\theta_W)$, from neutrino DIS on ^{56}Fe [32]. This was motivated by the fact that the NuTeV extraction of the $\sin^2(\theta_W)$ disagreed by three sigma with the Standard Model prediction [35], a discrepancy that has become commonly known as the NuTeV anomaly, shown in Fig. 1.12. In the reanalysis using the CBT model calculation, it was found that the model's isospin-dependent treatment of nuclear PDFs provides a resolution to the NuTeV anomaly, reducing the discrepancy by two-thirds, bringing the result into significantly better agreement with the Standard Model prediction.

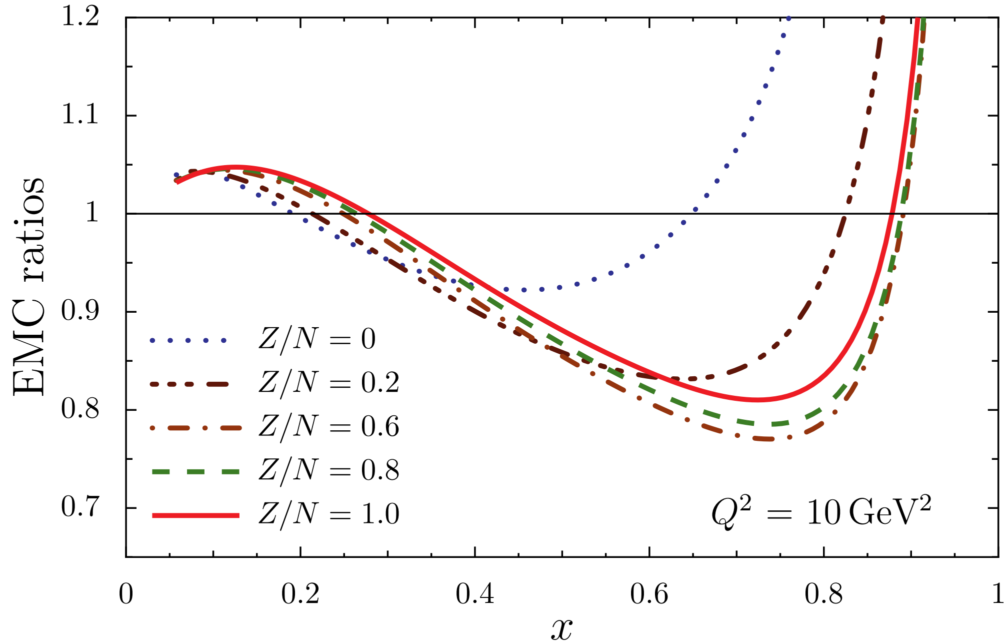

Figure 1.11: Figure from [32]. Theoretical calculations for the EMC effect in neutron-rich matter at $Q^2 = 10$ GeV^2. The EMC ratios are found to decrease from isoscalar nuclei until Z/N reaches approximately 0.6, at which point the EMC ratios begin to increase.

1.6.2 Short Range Correlations

Short Range Correlated pairs of nucleons (SRCs) are characterized by their high relative and low center of mass momenta. These high-momentum nucleons are thought to arise primarily due to the tensor component of the nucleon-nucleon interaction as well as the repulsive core of the strong interaction at short distances [36]. Several measurements have been performed to quantify the relative abundances of two-nucleon (2N) SRCs in a variety of nuclei [37] [38] [39]. From these studies, it has been found that the abundance of SRCs in a given nucleus strongly correlates with the size of the EMC effect in that same nucleus as shown in Fig. 1.13 [40] [41] [42]. It has also been experimentally found that most 2N SRCs are *np* pairs as opposed to *pp* or *nn* pairs [43], a phenomenon referred to as *np*-dominance.

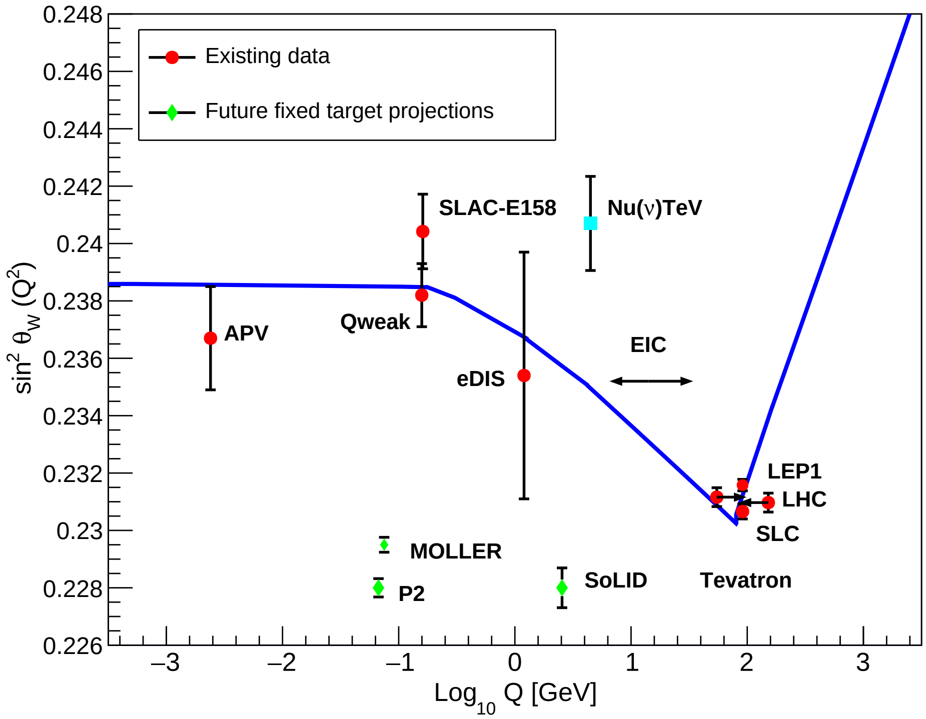

Figure 1.12: World data and projections for future measurements of $\sin^2(\theta_W)$ are shown alongside the Standard Model prediction (blue line). The NuTeV measurement is several standard deviations away from the prediction of the Standard Model. This result has become known as the NuTeV anomaly.

If there is a fundamental connection between the EMC effect and SRCs, then one would expect the isospin-sensitive nature of SRCs to introduce an isospin dependence into the EMC effect.

1.6.3 Nuclear PDF Fits

Studies have been performed comparing nuclear correction factors (F_2^A/F_2^D) obtained from Drell-Yan and charged-lepton DIS data with those obtained from neutrino DIS. While some analyses have found that the nuclear correction factors extracted from the two sources can be reconciled [44] [45] [46], other studies [47] [48] [49] published

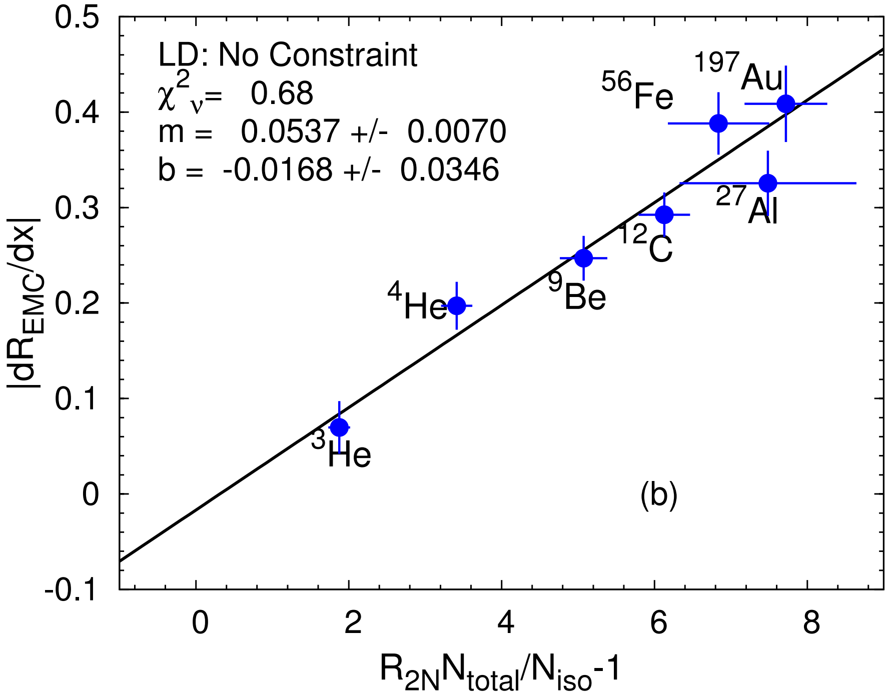

Figure 1.13: Figure from [42]. World data shows a strong correlation between the size of the EMC effect, here given by the slope of the EMC ratio $|dR_{EMC}/dx|$ in the range $0.3 < x_{Bj} < 0.7$, and the abundance of 2N SRCs in nuclei relative to ^{2}H, here given by $R_{2N}N_{total}/N_{iso} - 1$ (with the -1 term added so that the corresponding value for ^{2}H is 0, mirroring the EMC slope). R_{2N} represents the probability relative to ^{2}H that a nucleon will be part of a 2N SRC configuration. N_{total}/N_{iso} is the ratio of the total possible 2N pairs $A * (A-1)/2$ to the total number of possible np pairs NZ, accounting for the fact that 2N SRCs are predominantly np pairs [43]. It is important to note that, as addressed in [42], there are several different SRC-related quantities that can be used and that correlate well to the size of the EMC effect.

as recently as 2022 have found them to be in tension, as shown in Fig. 1.14. Due to the highly flavor-sensitive nature of the weak interaction, this tension hints at the possibility of isospin-dependent modification of PDFs. If true, this will have a significant impact on our ability to correctly interpret neutrino DIS data.

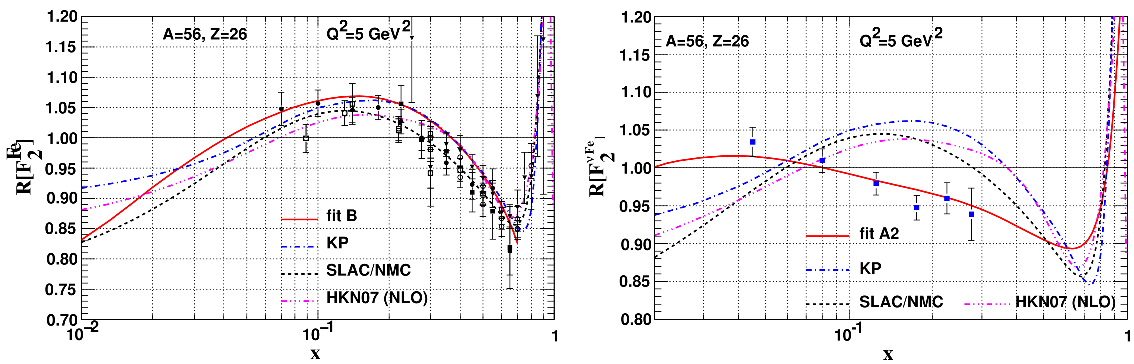

Figure 1.14: Figure from [47]. Nuclear correction factors for iron as a function of x_{Bj}. The left plot shows data obtained from charged-lepton-nucleus scattering and Drell-Yan data along with a fit of this data, labeled *fit B*. The right plot shows data obtained from neutrino-nucleus data along with its fit, labeled *fit A2*. These are shown alongside the SLAC/NMC parameterization (SLAC/NMC), fits from Kulagin and Petti (KP) [50] [51], and Hirai et al. [52].

1.7 Experiment E12-10-008

This work covers experiment E12-10-008 [2]. This experiment measured inclusive DIS cross sections for twenty-one nuclei, covering a broad kinematic range as shown in Fig. 1.15. Data were taken at EMC effect kinematics at three different scattering angles to allow for studies of the Q^2 dependence of EMC ratios. In particular, this allows for verification of the Q^2 independence of the EMC ratios above $Q^2 = 4$ GeV^2 that was found in experiment E03-103 [29]. In addition, the broad x_{Bj} coverage offers numerous advantages over measurements limited to the range $0.3 < x_{Bj} < 0.7$, where the EMC slope is typically determined. Extending our measurements to low x_{Bj} is useful because much of the existing data has the highest precision in this kinematic region. In addition, normalization uncertainties on these data are well constrained. Therefore, by taking measurements at $x_{Bj} < 0.3$, one can compare our results with existing high-precision data and verify that our data is properly normalized. Extending our measurements to $x_{Bj} > 0.7$ also provides an advantage.

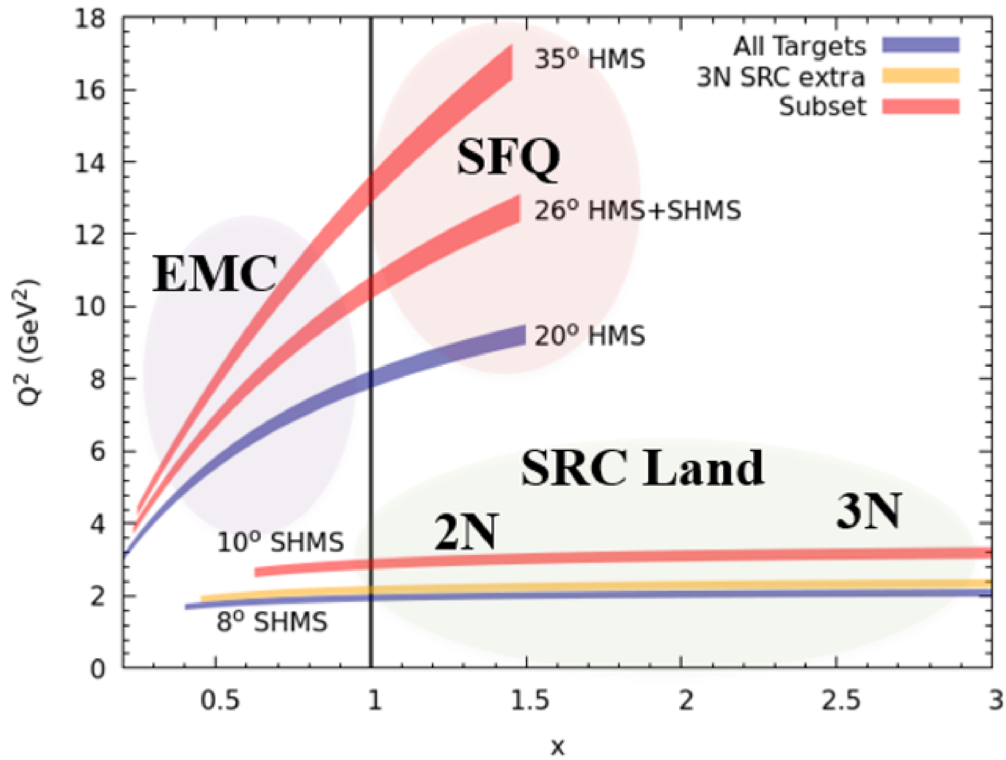

Figure 1.15: Kinematic coverage of the XEM2 run group of experiments. The kinematics for E12-10-008 are shown in the region labeled "EMC".

Above $x_{Bj} > 0.7$, the effects of Fermi motion begin to dominate the extracted EMC ratios, while quasielastic scattering also contributes significantly to the measured cross sections. Understanding quasielastic cross sections at $x_{Bj} > 0.7$ allows for better extraction of the radiative corrections that impact EMC ratios at $x_{Bj} < 0.7$. Utilizing the high-x_{Bj} data to better constrain our cross section model, EMC ratios can be more accurately extracted from the data.

Numerous insights can be gleaned from analysis of the twenty-one different nuclei that were studied in this experiment. Here, I will highlight a few of the primary goals of our experiment before delving into the experimental setup of E12-10-008.

Much like E03-103, a major focus of E12-10-008 is the study of the EMC effect in light nuclei. In addition to the light nuclei studied in E03-103, this experiment will provide the first measurements of the EMC effect at large x_{Bj} in ^{6}Li, ^{7}Li, ^{10}B, and ^{11}B. This is of particular interest, as it will provide the best dataset to date for discerning the impact of the local nuclear environment on nuclear structure functions.

Though it was measured in E03-103, ^{3}He was also measured in this experiment. Having an extreme N/Z ratio, ^{3}He provides the ideal environment to validate the isoscalar corrections that are made in order to compare isoscalar and non-isoscalar nuclei. This validation can be performed by comparing the ratio $^3\text{He}/(^2\text{H} +^1\text{H})$ to the ratio $^3\text{He}/^2\text{H}$, where the latter requires isoscalar corrections to be applied and the former does not. This was not possible at large x_{Bj} with the 6 GeV data due to resonances in the proton cross section impacting the data in that kinematic region. Now, with the upgraded 10.6 GeV electron beam, EMC ratios can be measured at higher Q^2 where the proton resonances are pushed above $x_{Bj} = 0.7$.

Another major goal of this experiment, which will also be the focus of the remainder of this dissertation, is the isospin or flavor dependence of the EMC effect. With this aim, targets such as ^{40}Ca, ^{48}Ca, ^{48}Ti, ^{58}Ni, and ^{64}Ni were studied to investigate the impact of varying the N/Z ratio at relatively fixed A. The motivations behind studying the isospin dependence of the EMC effect were addressed in Sec. 1.6.

Finally, E12-10-008 will provide data to support the investigation of the apparent relationship between the size of the EMC effect and the abundance of SRC pairs in a given nucleus. To this end, E12-10-008 ran in parallel with E12-06-105 [53], an experiment measuring the abundance of SRC pairs in nuclei through quasielastic inclusive scattering at large x_{Bj}. Running these two experiments in parallel has the effect of reducing the systematic uncertainty when comparing the EMC effect and SRC data due to them having several shared systematics uncertainties, such as those on the target thicknesses and cryogenic target density corrections. This in turn allows for a more direct comparison between the measurements of these two quantities and a more precise determination of whether these two phenomena are fundamentally connected.

Chapter 2

Experimental Setup

Experiment E12-10-008 collected inclusive DIS data in Hall C of Jefferson Lab from Fall 2022 through Spring 2023. This experiment primarily utilized the High Momentum Spectrometer (HMS) and a 10.6 GeV electron beam produced by the Continuous Electron Beam Accelerator Facility (CEBAF) [54]. Some data was also collected with the Super High Momentum Spectrometer (SHMS) for systematic checks. This chapter presents an overview of the instrumentation used for this experiment; more information can be found in the Hall C Standard Equipment Manual [55].

2.1 The Accelerator

The major components of CEBAF are the injector, two linacs, and two sets of recirculating arcs arranged in a race track configuration as shown in Fig. 2.1. This configuration allows the electron beam to circle the track up to 5 times ($5\frac{1}{2}$ times for Hall D), with a unique set of recirculating magnets required in each arc for each pass to handle the increasing beam energy.

The electron beam begins its life at the polarized electron source in the photo-cathode gun. The purpose of the photo-cathode gun is to provide bunches of highly polarized (roughly 80%) electrons. First, four lasers, one designated for each experimental hall, generate pulses at either 249.5 MHz or 499 MHz [56]. These frequencies are chosen as they are sub-harmonics of the 1.497 GHz accelerating and bunching

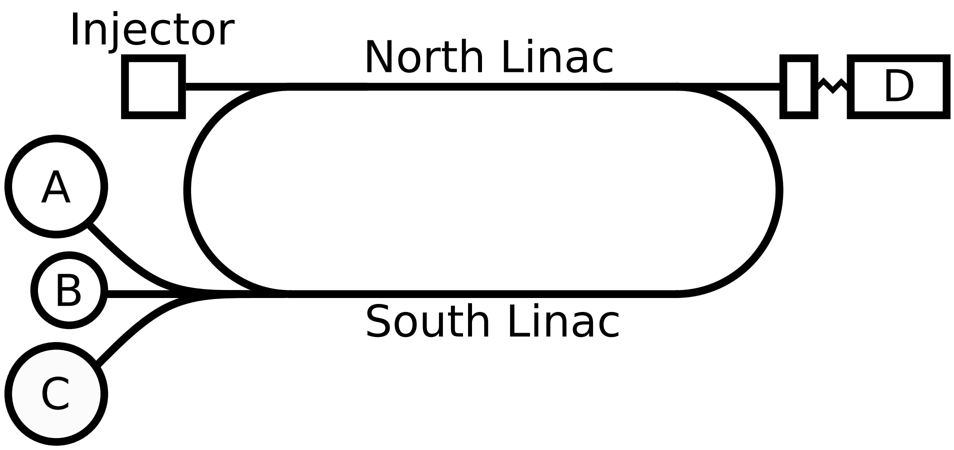

Figure 2.1: Sketch of the CEBAF accelerator site at Jefferson Lab in the 12 GeV era.

frequency of CEBAF. This approach allows for the simultaneous running of four experimental halls, each receiving variable beam currents. These laser pulses are then directed towards a strained GaAs cathode to produce polarized electrons. The sum of the currents sent to each of the four halls is typically on the order of several hundred μA. The electrons produced by each of the designated lasers are then bunched together and accelerated to 123 MeV in the injector before entering the main accelerator track.

The linacs utilize Superconducting Radio Frequency (SRF) technology to accelerate the electrons by about 1.1 GeV through a single linac, or by 2.2 GeV for a whole pass. For the 5-pass electron beam used in this experiment, the corresponding beam energy measured in the hall was 10.602 GeV. The goal of the recirculating arcs is to allow for multiple passes of the electron beam through a single linac. Each of the recirculating arcs consists of 5 sets of magnets, one to handle the specific energy of the beam at each pass. Once the desired number of passes around the accelerator track for a given electron bunch is achieved, the bunch is kicked into the beamline for the corresponding hall using an RF pulse. This kick is performed in an area of the accelerator known as the switchyard, located between halls A, B, and C and the south linac.

2.2 Hall C Beamline

Once the electron bunch is kicked into the Hall C beamline, it passes through several instruments on its way to the target chamber. These include wire scanners (harps), Beam Position Monitors (BPMs), Beam Current Monitors (BCMs), magnets to steer and focus the beam to the target, and rasters to increase the transverse size of the beam to avoid damaging the target. An overview of these systems is given here.

2.2.1 Harps

To ensure that the absolute beam position and cross-sectional area of the electron beam in the hall are within nominal limits, one can perform a harp scan. A harp scan is performed by passing a harp, a collection of wires with different orientations, transversely through the beamline with the beam powered on. As a wire passes through different sections of the beam, varying levels of current will be induced depending on the total flux of electrons along the wire as shown in Fig. 2.2. Using this information from wires with various orientations, one can determine the absolute position of the beam and reconstruct the beam profile. By placing several harps along the beamline, one can also determine the trajectory of the beam and how the beam profile evolves with position. The information provided by the harps is crucial for aligning the beam to hit the target, beam energy measurements, and beam polarimetry measurements which utilize the Compton or Møller polarimeters.

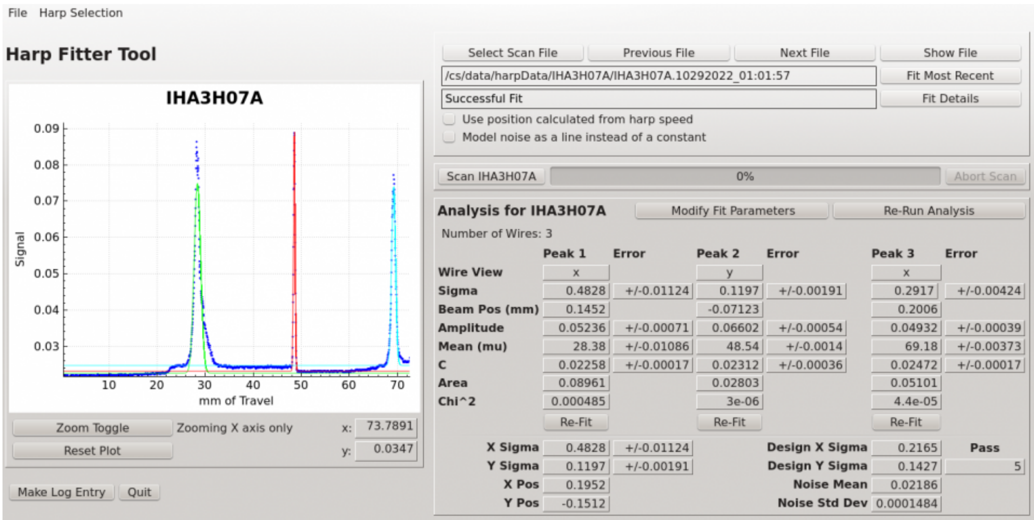

Figure 2.2: Result of a harp scan performed during the running of E12-10-008. The beam position is given by the X Pos and Y Pos values. The transverse size of the beam at the location of this harp was measured to be approximately 0.5 mm x 0.1 mm (X Sigma, Y Sigma).

2.2.2 Beam Position Monitors

While harps are great tools for determining beam position, a harp scan is an invasive measurement that requires dedicated beam time to perform. Therefore, to allow for continuous monitoring of the beam position during production running, BPMs are used instead. BPMs provide relative beam position measurements which, using harp scans for calibration, can be converted to absolute beam positions.

The BPMs used in Hall C are composed of four open-ended wire striplines (XM, XP, YM, YP), shown in Fig. 2.3, which are tuned to 1.497 GHz, the frequency of the beam. The wires are rotated 45° relative to horizontal to avoid damage from synchrotron radiation. As the electron beam passes through each of the BPMs, the beam generates an image charge on the wires. The magnitude of this charge is proportional to the distance of the beam from each of the plates. This allows one to determine the position of the beam as it passes through a BPM.

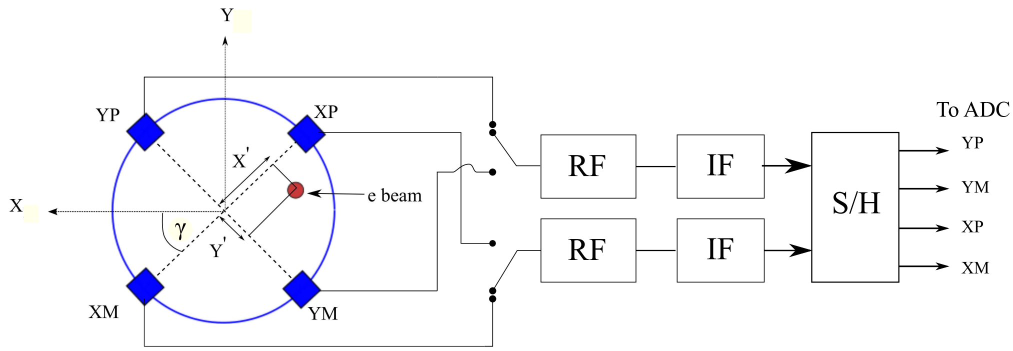

Figure 2.3: Figure from [55]. Schematic of the readout process for the Hall C BPMs. The 1.497 GHz RF signal from the BPMs is down-converted to an intermediate frequency (IF) and then digitized.

During the running of E12-10-008, the beam position remained relatively stable, having variations on the order of the expected precision of the measurement, 0.1 mm. Measured values for the beam position at each of the three upstream BPMs obtained during June 2022 are given in Table 2.1.

2.2.3 Beam Current Monitors

The Hall C BCM system provides continuous, non-invasive measurements of the current of the electron beam that enters the hall. This system is essential for determining the total charge accumulated in a given dataset, which is used for extracting abso-

BPM	X Position (mm)	Y Position (mm)
IPM3H07A	0.172	0.085
IPM3H07B	-0.211	0.242
IPM3H07C	-0.374	0.234

Table 2.1: Single EPICS readout of the electron beam positions measured by the upstream BPMs in Hall C in June 2022. These values are constrained by beam position locks and therefore should not drift significantly over time. In addition, these values are corrected in the analysis to give absolute beam positions. BPMs IPM3H07A, B, and C are located 3.71 m, 2.25 m, and 1.23 m upstream of the target, respectively.

lute cross sections. To this end, there are several devices upstream of the target whose function is to measure the beam current. The BCM system consists of an Unser monitor and five RF resonating cavities (BCM1, BCM2, BCM4A, BCM4B, and BCM4C) which are tuned to the beam frequency of 1.497 GHz. These monitors are highly sensitive to temperature fluctuations and are therefore wrapped in thermal blankets (Unser, BCM1, BCM2) or located in a thermally stabilized box (BCM4A, BCM4B, BCM4C). The RF output signals from these monitors are processed and sent to voltage-to-frequency (V2F) converters. Each signal is then sent to the data acquisition system and read out by the scalers, resulting in a scaler rate equal to the frequency of the signal output by the V2F converter.

The Unser monitor, a type of Parametric Current Transformer (PCT) [57], is unsuitable for use during standard data collection. This is because it has an overall offset that drifts significantly over time scales on the order of a few minutes. On the other hand, the gain of the Unser monitor is very stable. This contrasts with the BCMs, which have stable offsets but have slightly unstable gains that must occasionally be determined to enable one to accurately convert from a BCM response to the corresponding beam current. These gains are determined by performing a BCM calibration, which utilizes the Unser monitor due to its stable gain. This property of the Unser monitor allows for it to be used to determine the gains of the other RF cavities provided a set of data where the beam is frequently turned on and off. The beam-off periods allow one to account for the drifts in the Unser monitor's offset over short timescales, while the beam-on periods can then be used to determine the gains of the RF cavities. The procedure to calibrate the BCMs is discussed further in Sec. 3.4.

2.2.4 Rasters

The primary raster system in Hall C, known as the Fast Raster (FR), consists of two sets of orthogonal (horizontal and vertical) electromagnets that produce rapidly varying magnetic fields to increase the transverse size of the beam on the target to several square millimeters. These electromagnets are driven by four separate currents with triangular waveforms as shown in Fig. 2.4. This is necessary due to the large amounts of energy that would otherwise be deposited on small, highly concentrated areas of the target chamber, the target, and the beam dump, which could lead to permanent damage. The rasterization of the beam mitigates the risk of solid targets melting, helps prevent the cells of cryogenic targets from being damaged, and reduces density losses in cryogenic targets by spreading the heat load from the beam over a wider area. In addition, this process serves to reduce uncertainties due to variations in the thicknesses of targets by effectively averaging the target thickness over a larger area. During experiment E12-10-008 the raster was set to spread the beam over a square 2.00 mm $\times$ 2.00 mm area on the target.

2.3 High Momentum Spectrometer

The High Momentum Spectrometer (HMS) is the older of the two spectrometers currently installed in Hall C, with the newer Super High Momentum Spectrometer (SHMS) replacing the Short Orbit Spectrometer (SOS) with Jefferson Lab's 12 GeV upgrade. A sketch of the Hall C layout is given in Fig. 2.5. The HMS is located beam-right and the SHMS is located beam-left. The HMS and SHMS are moderate acceptance spectrometers, restricted to probing specific regions of kinematic (phase) space at a given time. The moderate acceptance of these spectrometers enables them to probe regions of phase space at higher luminosities than other larger acceptance

Figure 2.4: The Hall C raster controls GUI during E12-10-008. The top right plot shows the triangular waveform of the current driving the raster magnets. The bottom right plots show the 2.00 mm × 2.00 mm square pattern of the beam after passing through the raster. The size of the raster pattern is set using the “Width (mm)” and “Height (mm)” input fields in the “Turning Raster On” section of the GUI, which is located in the bottom left box.

spectrometers can handle. This allows one to quickly measure the regions of phase space they are interested in with world-leading statistical precision.

The HMS magneto-optical components consist of four large superconducting magnets: three quadrupoles and a dipole, which focus and bend particles of a given momentum into the detector hut as shown in Fig. 2.6. The quadrupoles focus particles within roughly ±8% of a specified central momentum onto the nominal focal plane of the spectrometer. This ensures that these particles will have a track that intersects all detector subsystems in the detector hut. The dipole then bends these particles (again

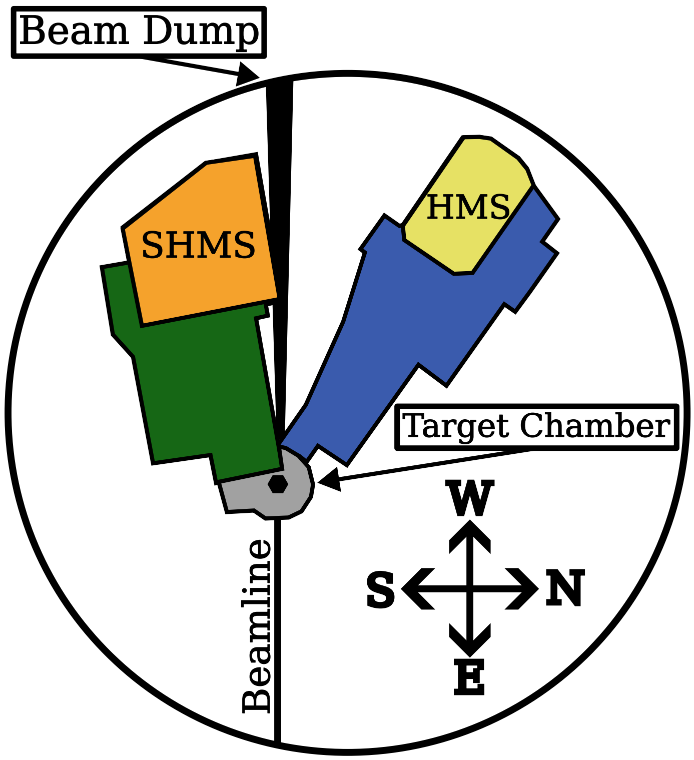

Figure 2.5: View from above of the layout of the spectrometers in Hall C. The electron beam enters the hall from the east side. It then intersects the target in the target chamber. Most electrons pass straight through the target, traveling to the beam dump on the west side of the hall. The SHMS is located beam-left, and the HMS is located beam-right, with the detector huts for each spectrometer shown in orange and yellow, respectively.

within roughly ±8% of the same specified central momentum) by 25° vertically up into the detector hut. Except when a polarity change is made, the settings of these magnets can be changed on order of 15 minutes, with special care made to minimize the effects of hysteresis, allowing for rapid reconfiguration of the spectrometer so that it can detect particles of various different momenta without significant downtime.

The HMS is mounted on top of a steel carriage that can move on a series of rails, allowing the entire spectrometer to rotate about the target. This process typically takes on the order of 10 minutes, depending on how far the spectrometer needs to move.

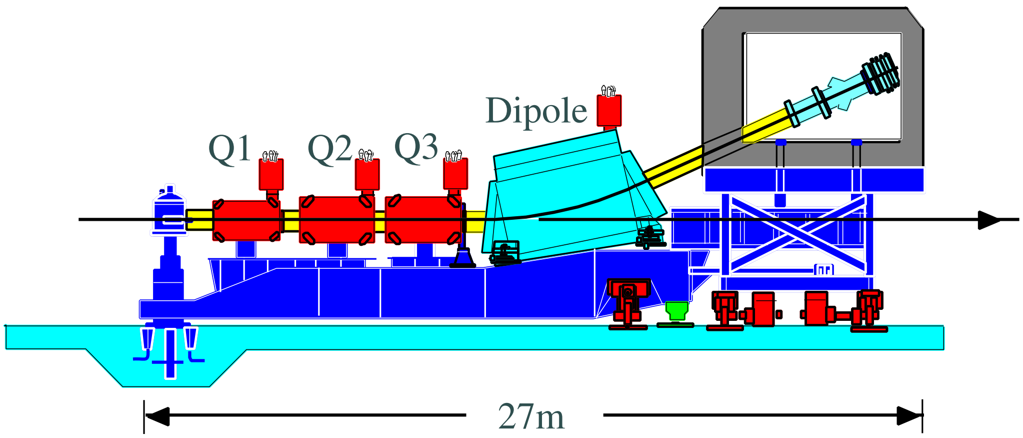

Figure 2.6: Figure from [58]. Sketch of the side profile of the HMS. Particles scattered from the target chamber within the angular acceptance of the spectrometer first pass through three quadrupole magnets (Q1, Q2, and Q3) that focus particles of a selected momentum onto the spectrometer focal plane. Particles of the selected momentum are then bent into the detector hut by the dipole magnet.

Both the angle and magnet settings of the spectrometer can be controlled remotely from the counting house using the GUIs shown in Fig. 2.7. Using these controls, one can select a particular region of phase space in Q^2 and x_{Bj} to be measured by carefully calculating the corresponding scattering angle and central momentum and configuring the detector accordingly. Table 2.2 outlines the nominal operational ranges, acceptances, and resolutions of the HMS.

Parameter	HMS Performance
Maximum Central Momentum	7.3 GeV
Momentum Acceptance ($\delta p/p$)	$\pm$8%
Momentum Resolution ($\delta p/p$)	<0.1%
Central Angle Range	10.5° - 90°
Horizontal Angular Acceptance	$\pm$32 mrad
Vertical Angular Acceptance	$\pm$85 mrad
Horizontal Angular Resolution	0.8 mrad
Vertical Angular Resolution	1.0 mrad

Table 2.2: Nominal operational ranges, acceptances, and resolutions of the HMS.

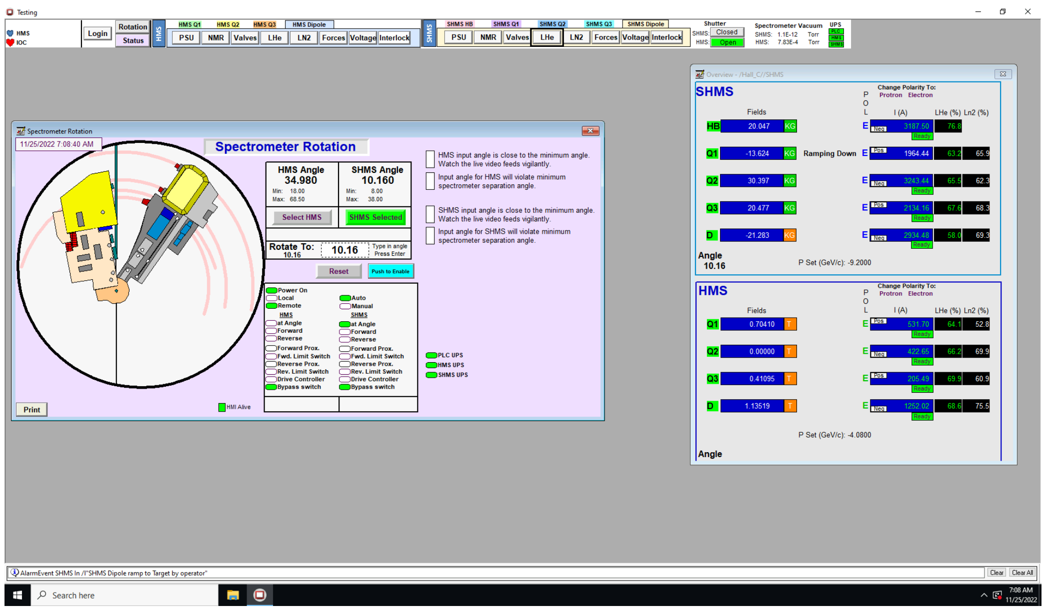

Figure 2.7: The spectrometer rotation and magnet control GUI in Hall C during E12-10-008 running.

2.4 HMS Detector Package

Once scattered particles have passed through the optical components of the HMS, they enter the detector hut. The HMS detector hut houses two horizontal drift chambers, two pairs of scintillator hodoscope planes, a Cherenkov detector, and a lead glass calorimeter. This section provides an overview of these detector subsystems.

2.4.1 Scintillator Hodoscopes

When high-energy charged particles, such as electrons, pass through a scintillating material they lose some of their energy (typically a few MeV in the case of the HMS scintillators). This deposited energy causes the scintillating material to be stimulated into an excited state. The material then rapidly decays back into the ground state, causing it to luminesce. Because the characteristic decay time of these excited states is typically on the order of nanoseconds, the signal produced has excellent timing

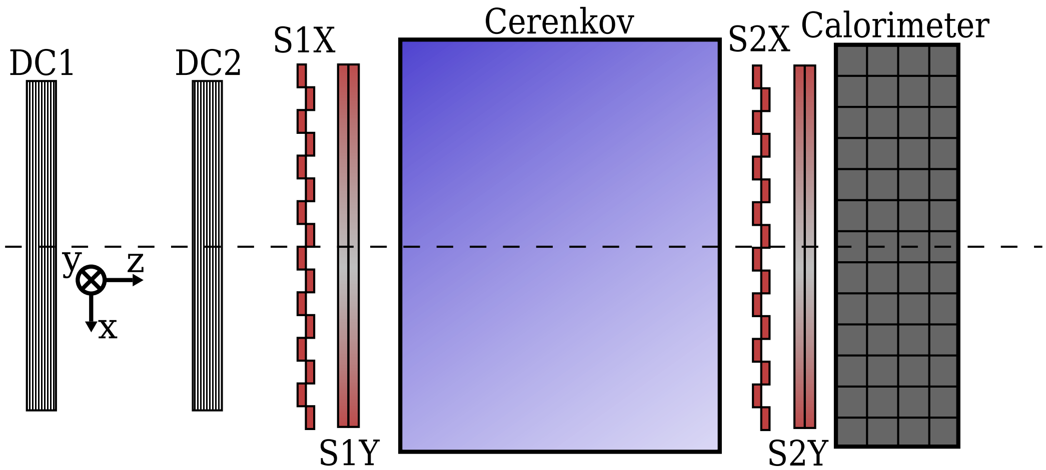

Figure 2.8: Diagram of the HMS detector package. Particles scattered or ejected from the target travel along the positive z-direction, with most electrons (and positrons for positive polarity magnet settings) ending their journey in the calorimeter. The positive x-direction points towards the floor of Hall C with an angle of 25° relative to vertical. The positive y-direction points towards the beamline.

resolution.

The HMS contains two pairs of scintillating hodoscope planes separated by approximately 2 meters. Each pair contains one plane with its hodoscope paddles oriented along the x-axis of the spectrometer and another plane with hodoscope paddles arranged along the spectrometer's y-axis.

Each hodoscope plane is composed of ten to sixteen BC-404 [59] scintillators optimized for use in high-rate environments; the time constant for these scintillators is 1.8 ns. Table 2.3 summarizes the dimensions of the scintillators and how they are divided between the four hodoscope planes. Each scintillator paddle is coupled via light guides to one Philips XP2282B photomultiplier tube (PMT) on each end to convert the light emitted by the scintillator material into an electrical signal and amplify it. The material used as a light guide from the scintillator material to the PMTs is UVT lucite. This material was selected for having good transparency to the 400 nm light emitted by the BC-404 scintillators. The hodoscope paddles are wrapped in aluminum foil to reflect otherwise outgoing light, and tedlar to minimize the amount of light that leaks between or otherwise escapes the paddles.

Due to their precise timing resolution, the primary purpose of the HMS hodoscopes is to provide timing information for the other HMS subsystems. This information can also be used for particle identification (PID) through time-of-flight (TOF) measurements to distinguish between particles of different masses provided that the expected TOF difference is larger than the timing resolution. In addition, due to the high detection efficiency of the combined four hodoscope planes and the fast signals they produce, the HMS hodoscope system is used to form the trigger that informs the data acquisition system to begin reading out the signals from all of the detectors.

2.4.2 Drift Chambers

The typical drift chamber consists of a gaseous medium and planes of wires connected to high-voltage. When a high-energy charged particle passes through the gas in a drift chamber, a track of ionized atoms is left in its wake. The freed electrons then accelerate toward the closest positive potential wires. These electrons reach energies large enough to produce electron-ion pairs when they knock into atoms on their way toward the wire, creating a Townsend avalanche. The electrons produced

Plane	Number of Paddles	Length	Width	Thickness
S1X	16	75.5 cm	8.0 cm	1.0 cm
S1Y	10	120.5 cm	8.0 cm	1.0 cm
S2X	16	75.5 cm	8.0 cm	1.0 cm
S2Y	10	120.5 cm	8.0 cm	1.0 cm

Table 2.3: Dimensions and layout of the scintillators in the HMS hodoscope planes. The thickness of these paddles is kept small (1.0 cm) to minimize the energy loss of the passing particles on their way to the calorimeter.

in the Townsend avalanche are then collected by the nearest positive potential wire, generating a signal. By creating a series of planes, each with its own set of parallel wires, and orienting the planes normally to the path of the ionizing particle, one can precisely determine the path the ionizing particle took through the wire planes based on the wires in each plane that received a signal. This can be taken a step further by utilizing the timing information from the hodoscopes. Because we know when the particle passed through each of the hodoscope planes, we can also determine when the particle passed through each of the wire chambers. Using the difference between this time and the time that the ionized electrons were picked up by the wire, one can determine precisely how far the ionizing particle was from that wire when it passed through the plane. This is the fundamental working principle behind drift chambers.

Just after the 12 GeV upgrade to Jefferson Lab, the HMS received a new pair of drift chambers. These drift chambers were modeled after those produced for the SHMS [60], differing primarily in their cross-sectional area [61]. The HMS drift chambers each consist of 6 wire planes, X, U, V, X', U', and V'. Each chamber is divided into two half-chambers of 3 wire planes and four cathode planes (made from copper-plated Mylar), with each wire plane located between two cathode planes as illustrated in Fig. 2.9. Each wire plane consists of alternating sense wires that collect the negative charges (held at 0 V) and field wires held at a large negative potential (several kV). The spacing between each of these wires is 0.5 cm. A fiberglass mid-plane separates the two halves of a single drift chamber.

The wires in the X plane run horizontally relative to the ground. The wires in the U plane are rotated 60° relative to the wires in the X plane. The V plane is formed by rotating the U wire plane by 180° about the vertical axis. The primed wire planes are formed by a 180° rotation about the axis normal to the wire plane of the corresponding un-primed planes, producing the same wire pattern shifted by

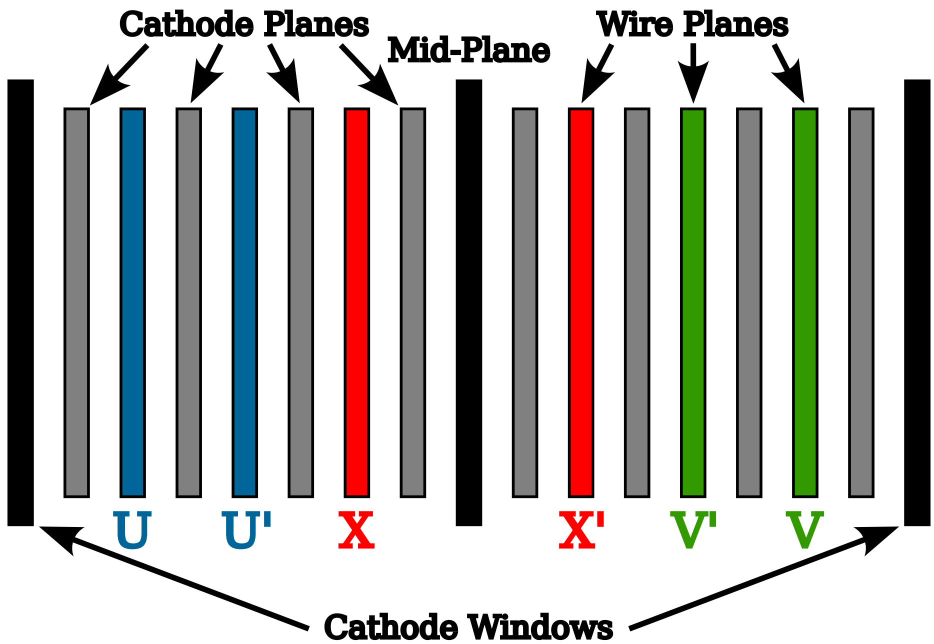

Figure 2.9: Side view of one of the HMS drift chambers.

1/2 of the wire separation. An illustration of the wire orientations is given in Fig. 2.10. In the first chamber, the planes are ordered U, U', X, X', V', and V; the second chamber is identical to the first chamber, but rotated 180° about the vertical axis. This effectively reverses the order of the planes and also makes the V and V' planes in the second chamber parallel to the U and U' planes in the first chamber, and vice versa. The gas that flows through the drift chamber is composed of a 50-50 mix of ethane and argon. Due to its chemical stability, large size, and relatively low cost, argon gas is used to promote Townsend avalanches. On the other hand, ethane is used for its quenching properties, absorbing UV photons to prevent electrons from being freed from the cathode due to the photoelectric effect.

As previously mentioned, the primary role of the HMS drift chambers is to provide precise tracking information. This information is then used in conjunction with the known properties of the magneto-optical system to reconstruct the scattering vertex

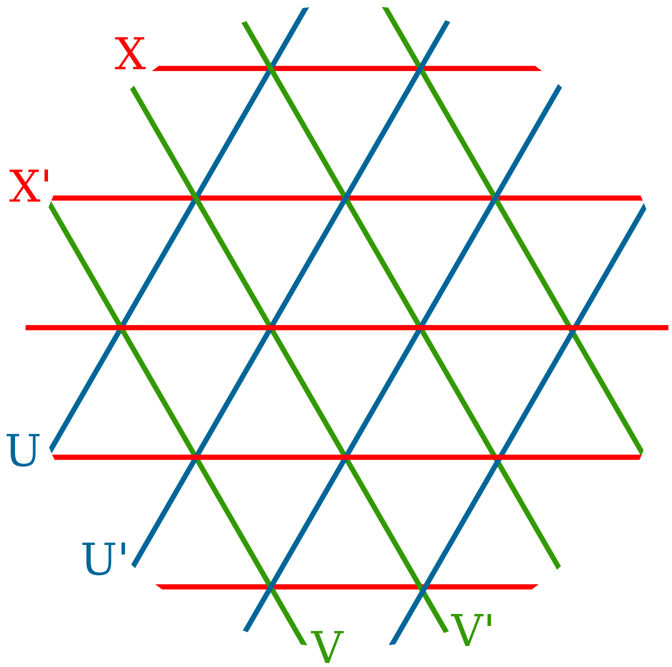

Figure 2.10: Wire layout in an HMS drift chamber viewed from along the direction of incoming particle motion ($+z$-direction).

(the position in the target where the scattering event occurred), scattering angle (θ), and momentum of a detected particle.

2.4.3 Gas Cherenkov

When a charged particle travels through a medium at a speed greater than the speed of light in that medium, Cherenkov radiation is produced. This condition can be expressed in terms of the medium's index of refraction n as

$$\beta > \frac{1}{n}, \tag{2.1}$$

where β is the ratio of the particle's speed to the speed of light in vacuum (c). This in turn produces a cone (or ring after the radiation stops being produced) of Cherenkov light as shown in Fig. 2.11. From this figure, the angle θ_c between the track of the charged particle and the emission angle of Cherenkov radiation can be immediately found to be

$$\cos(\theta_c) = \frac{1}{\beta n}. \tag{2.2}$$

Assuming negligible energy loss, the charged particle produces a constant number of Cherenkov photons between wavelengths λ_1 and λ_2 per unit length of the material it travels through, given by

$$\frac{dN}{dx} = 2\pi\alpha z^2 \int_{\lambda_1}^{\lambda_2} \left(1 - \frac{1}{(n(\lambda)^2)\beta^2}\right) \frac{d\lambda}{\lambda^2}, \tag{2.3}$$

where α is the Sommerfeld constant, and z is the charge of the particle producing Cherenkov radiation [62]. In order to maximize the signal produced, Cherenkov detectors tend to be very large compared to the previously discussed detectors.

The HMS Cherenkov detector is primarily used for particle identification (PID). Revisiting Eq. 2.1 and using the equation (in natural units) for relativistic momentum given by

$$p = \gamma m_0 \beta, \tag{2.4}$$

where m_0 is the particle rest mass and γ is the Lorentz factor $1/\sqrt{1-\beta^2}$, one finds that the momentum required for the production of Cherenkov radiation can be written in the form

$$\frac{1}{n} < \beta = \frac{p}{\sqrt{m_0^2 + p^2}}. \tag{2.5}$$

This particular form is of interest because the magnets in the HMS select particles of a given momentum to enter the detector stack. This means that particles of different

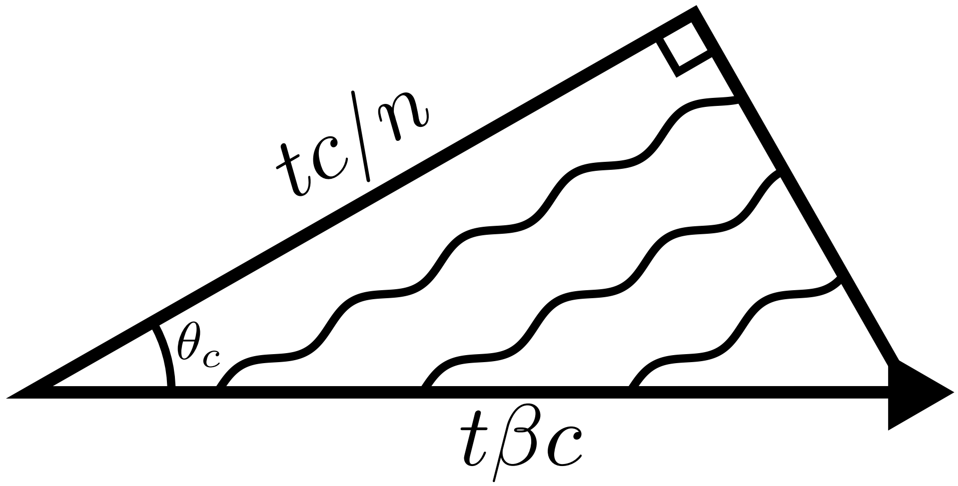

Figure 2.11: Depiction of the relationship between Cherenkov angle θ_c, the index of refraction n, and the particle velocity β. If $1/n$ is greater than β, there is no real solution to Eq. 2.2, reflecting the fact that there will be no angle at which a coherent wavefront can exist to produce Cherenkov photons.

rest masses will travel through the detector stack with different velocities. One can carefully select the index of refraction of the medium in the Cherenkov detector such that, at a given momentum, only certain types of particles (below a certain rest mass) will produce Cherenkov radiation, while heavier particles will not. This makes the Cherenkov detector a powerful tool for PID.

The HMS Cherenkov detector consists of a large cylindrical tank with an inner diameter of 59 inches and a length of 60 inches. This tank contains two mirrors that each focus their light onto one of two PMTs. The tank was filled with octafluorotetrahydrofuran (C_4F_8O) at 0.4 atm. This setup results in, on average, a combined 12 photoelectrons emitted from the photocathodes of the PMTs for a single event above the Cherenkov threshold. This gas mixture also corresponds to a pion Cherenkov threshold momentum of approximately 4 GeV and an electron threshold momentum of about 15 MeV. This allows for the Cherenkov detector to be used to distinguish between these two particles at energies that are above the electron threshold but below the pion threshold. As pions are the main source of background in our data, the ability to distinguish them from electrons is indispensable. One might note that some of the data our experiment collected on the HMS is at momenta above 4 GeV, making the Cherenkov detector mostly useless for this data because both electrons and pions will produce a signal in the detector. However, at our kinematics, pion yields decrease rapidly as momentum increases, to the point that pion contamination is relatively insignificant above 4 GeV. Therefore, this limitation is not an issue.

2.4.4 Electromagnetic Calorimeter

The final detector that a particle encounters in the HMS detector stack is the electromagnetic calorimeter. The HMS electromagnetic calorimeter is composed of four layers of thirteen stacked TF1 lead glass blocks [63]. Each block is coated in a layer of aluminized Mylar and Tedlar for optical isolation. Their dimensions are 10 cm x 10 cm x 70 cm, with the long edges parallel to the y-axis as shown in Fig. 2.8. The front two layers have PMTs on both of the square ends, while the back two layers have PMTs on only one end.

The purpose of an electromagnetic calorimeter is to measure the energies of incident electrons, positrons, and photons. These particles are in their own category because they experience high energy losses from bremsstrahlung (for electrons and positrons) and electron-positron pair production (for photons) when passing through matter at high energies (>100 MeV). This contrasts with heavier particles (muons, pions, protons, etc.), which are less impacted by energy loss from bremsstrahlung at high energies due to their larger masses, and are therefore harder to stop. Because

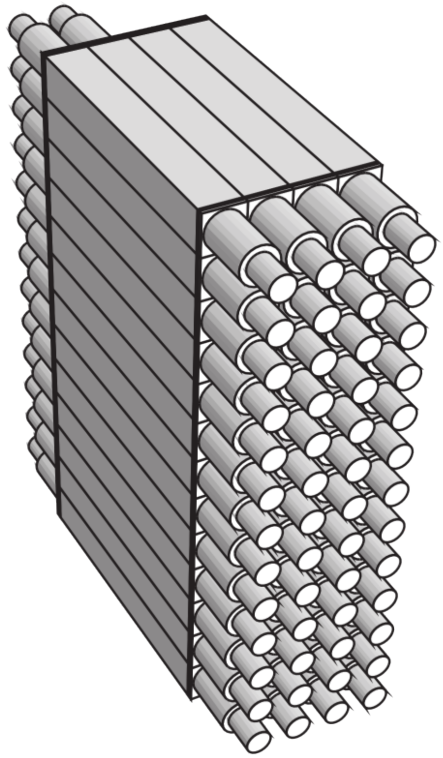

Figure 2.12: Figure from [63]. CAD drawing of the HMS electromagnetic calorimeter.

these heavier particles are harder to stop, most of them punch through the end of the calorimeter, depositing only a fraction of their energy. Since the HMS's tracking system already provides accurate information about a particle's momentum, the electromagnetic calorimeter is primarily used for PID by allowing one to distinguish between particles that deposit all their energy into the calorimeter and those that do not.

The precise working principle of a calorimeter can vary depending on the material(s) used. The bulk of the HMS electromagnetic calorimeter is made up of lead glass blocks. The lead glass functions as both the detector and the absorber, forming what is known as a homogeneous calorimeter. The short radiation length of TF1 lead glass (X_0 = 2.74 cm) allows it to promote electromagnetic showers and absorb the majority of a particle's energy over relatively short distances (40 cm = $14.6X_0$). In

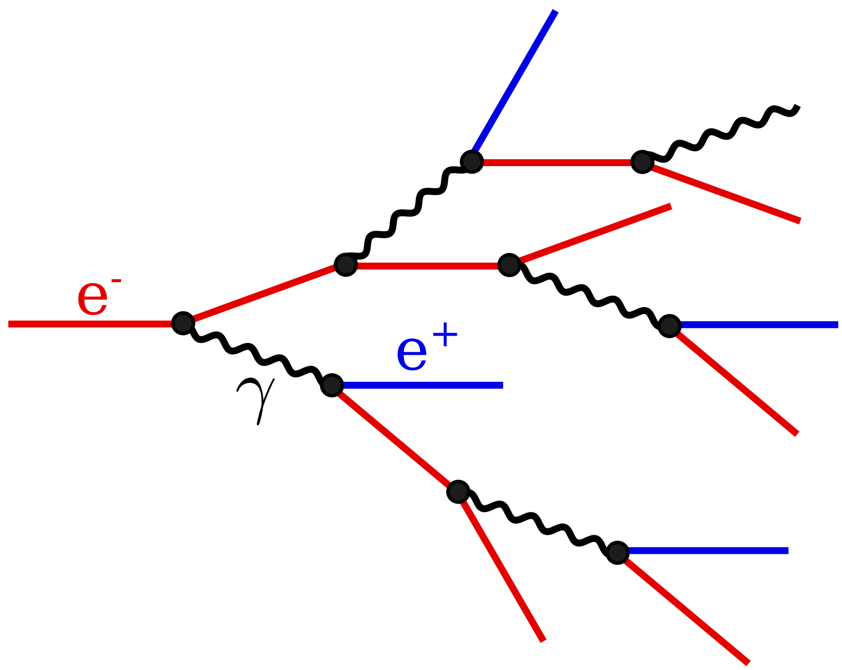

Figure 2.13: Diagram of a simple electromagnetic shower.

the case of an electron, an electromagnetic shower is produced when the high-energy electron emits a high-energy bremsstrahlung photon, which, in turn, may produce an electron-positron pair. This cycle continues until the energies of the particles fall below roughly 10 MeV, where processes such as ionization (for electrons and positrons) begin to dominate. A simple diagram of an electromagnetic shower is shown in Fig. 2.13. Somewhat counterintuitively, the energy lost in the aforementioned processes is not what is directly measured in a lead glass calorimeter. What is directly measured is the Cherenkov radiation produced by the electrons and positrons in the shower as they travel through the lead glass ($n = 1.65$). The amount of Cherenkov radiation produced is proportional to the sum of the path lengths of all electrons and positrons in the shower. This, in turn, is proportional to the energy these same particles deposit into the calorimeter via ionization. Therefore, the measured Cherenkov signal is proportional to the energy deposited into the calorimeter.

2.5 Hall C Data Acquisition and Trigger

The purpose of the Data Acquisition System (DAQ) is to digitize the signals produced by each of the detector subsystems described in the previous section and write them to disk when selected conditions are met. In Hall C, the data acquisition system is implemented using the CEBAF Online Data Acquisition (CODA) toolkit [64].

The signals are digitized using analog-to-digital converters (ADCs) and time-to-digital converters (TDCs). The ADCs used in Hall C are FADC250 modules (fADCs) [65]. These modules digitize the input signal at a sampling frequency of 250 MHz (4 ns) and can be configured to provide either a complete digitized waveform or an integrated pulse amplitude. They are used to digitize the signals from the HMS hodoscope planes, gas Cherenkov detector, and lead glass calorimeter. The modules are located in the Hall C Electronics Room of the Counting House and receive signals from the hall below via cables that connect to the detector. The CAEN V1190A TDCs [66] are used to provide precise timing information with a resolution of 100 ps. These TDCs are used to digitize the signals from the HMS drift chambers, hodoscope planes, gas Cherenkov detector, and lead glass calorimeter. The TDCs are located in the Hall C Electronics Room of the Counting House for all detectors except the drift chambers, for which they are located in the HMS Detector Hut.

Constantly writing the digitized signals from all of the detectors to disk would produce significant amounts of data, most of which would be noise. Therefore, a trigger system must be used to determine when the digitized signals should be written to disk. Signals from the hodoscopes, calorimeter, and Cherenkov detector are used to form their detector-specific pre-triggers. These pre-triggers are then combined using logic gates (AND/OR) to form higher-level pre-triggers. A pre-trigger (or multiple pre-triggers) can then be selected to form the Level 1 (L1) accept trigger that is sent

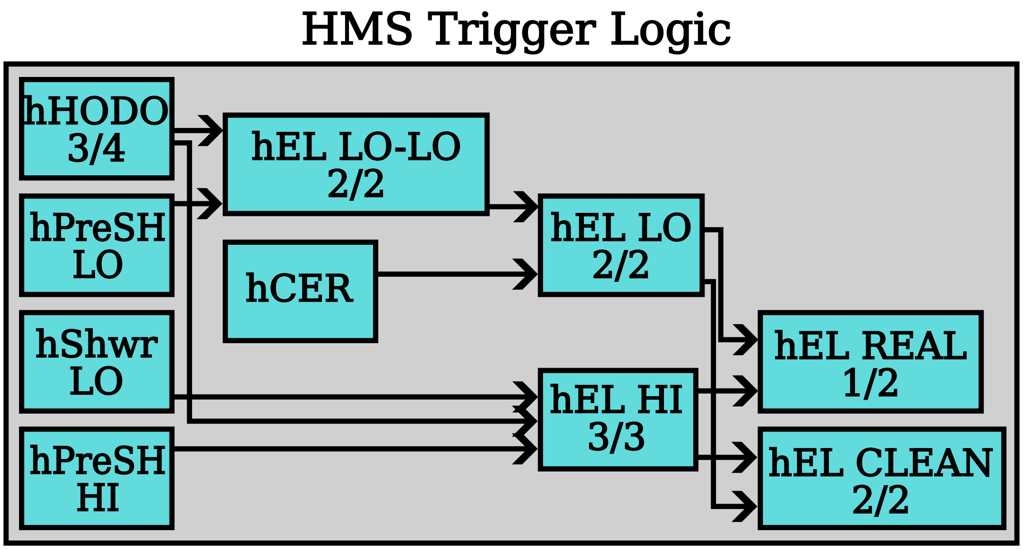

Figure 2.14: Diagram of the trigger logic for the HMS. For pre-triggers with a fraction under their name, that fraction indicates the number of pre-triggers connected to it on the left that must have fired (been activated) for that pre-trigger to activate as well. For example, the hEL_CLEAN pre-trigger will activate if both the hEL_LO and hEL_HI pre-triggers fire, while the hEL_REAL pre-trigger will activate if either one of them fires. The prefix "h" indicates that the pre-trigger is associated with the HMS detector. The SHMS has a nearly identical trigger logic configuration, and the associated pre-triggers begin with the letter "p".

to the readout controllers (ROCs) to initiate the writing of the digitized signals to disk for a given time window (several μs). A diagram of the trigger logic used in the HMS during E12-10-008 is shown in Fig. 2.14.

All data collected during the E12-10-008 experiment used one of three trigger types to initiate the writing of data to disk: hHODO 3/4, hEL_REAL, or hEL_CLEAN. The maximum trigger rate allowed during the experiment was 4 kHz due to limitations with the rate at which data can be written to disk. For kinematics where rates exceeded this limit, a "prescale factor" was applied which drops all but every nth trigger, allowing the computer to keep up with the rate at which data was trying to be written to disk. Descriptions of the detector-specific pre-triggers are provided below along with descriptions of the three trigger types used during E12-10-008.

- **hPreSH_LO, hPreSH_HI, and hShower_LO:**

  As previously discussed, the HMS calorimeter consists of four layers of lead glass blocks. These layers are labeled A, B, C, and D from front to back. For each layer, the sum of the signals produced by each of the blocks in that layer is used to construct the quantities Asum, Bsum, Csum, and Dsum. The hPreSH_LO and hPreSH_HI pre-triggers are formed if the sum of Asum and Bsum are above the corresponding predetermined thresholds. Similarly, the hShower_LO pre-trigger is formed when the sum of the signals from all four layers is above another predetermined threshold.

- **hCER:**

  The signal from the HMS Cherenkov detector is read out using two PMTs. The signals from each of these PMTs are summed together. If this sum is above a predetermined threshold, the hCER pre-trigger is formed.

- **hHODO 3/4:**

  The hHODO 3/4 trigger (often simply called the "three-of-four trigger") only requires "hits" on three of the four hodoscope planes to fire. In a hodoscope plane, a "hit" is defined as when at least one scintillator paddle produces signals above a predetermined threshold in both of its PMTs. This trigger is often called an unbiased trigger because, by not requiring any information from the two PID detectors (the calorimeter and Cherenkov), it has an approximately equal probability of firing for any type of charged particle. This trigger is primarily used for background studies because it fires for a large portion of the background events (which in our case are mostly pions). This trigger is also used for PID detector efficiency studies.

- **hEL_REAL:**

  The hEL_REAL trigger was the primary trigger used to collect production data for E12-10-008. Electrons are identified by their large energy deposition in both the calorimeter and Cherenkov detectors. Therefore, by requiring either the hPreSH_LO and hCER or the hShwr_LO and hPreSH_HI pretriggers to have fired, this trigger is biased towards firing for electrons, however, a decent number of background events do still cause this trigger to fire. For most kinematic settings studied, the background suppression of the hEL_REAL trigger resulted in reasonable (<4 kHz) trigger rates, therefore a more biased (and potentially less efficient) trigger was not necessary for production data taking.

- **hEL_CLEAN:**

  The hEL_CLEAN trigger was the most strict trigger used during E12-10-008. This trigger was selected to collect data for settings where background rates far exceeded the 4 kHz limit at which data can be written to disk, and the rates of the events of interest were small in comparison. Without a very strict trigger, a larger prescale factor would be required to keep the prescaled trigger rate below 4 kHz. This additional prescaling would proportionally increase the beam time required to collect the desired number of non-background events. Therefore, a more strict trigger must be used so that beam time can be more efficiently utilized. To this end, the hEL_CLEAN trigger was employed during positive-polarity data collection, where the particles of interest were pair-produced positrons whose rates were significantly lower than the pion and proton backgrounds. The hEL_CLEAN trigger was not used during any of the negative-polarity data collection.

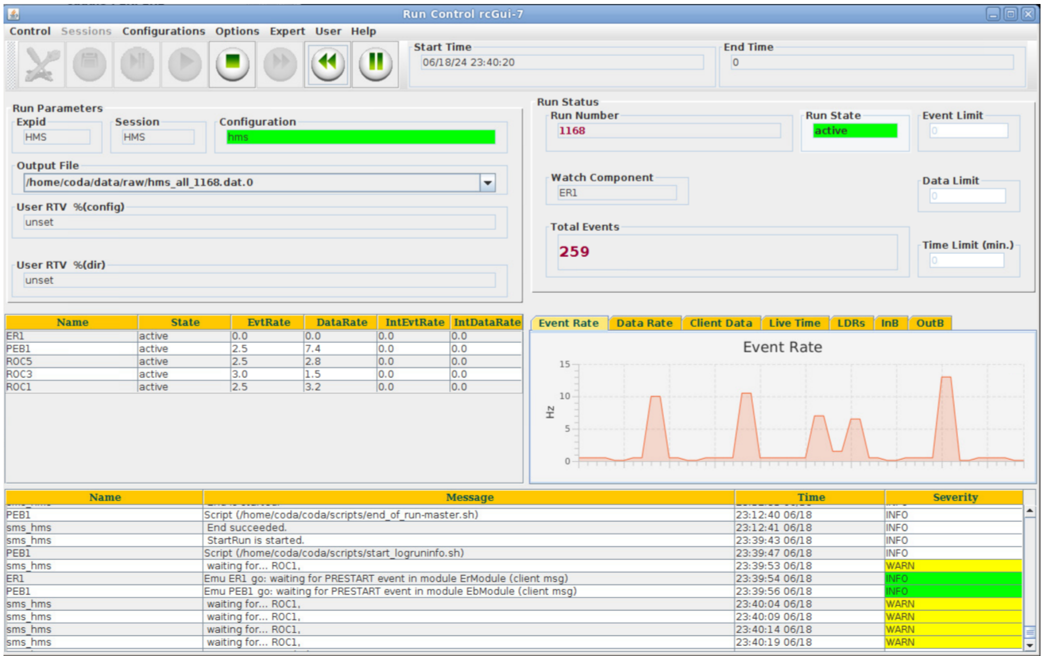

Figure 2.15: The run control GUI used by shift workers to start and stop data collection for the HMS.

The data collected during E12-10-008 is organized into numbered .dat files, each constituting an individual period of data collection known as a “run”. Data collection for a run is started and stopped by the shift leader by using the run control GUI, shown in Fig. 2.15. Each run is usually associated with a specific configuration defined by the target, spectrometer configuration (angle, momentum setting), beam energy, and trigger type. These parameters are not changed over the course of a single run, allowing all of the data collected during a single run (and runs with the same parameters) to be analyzed as a unit without needing further subdivisions. In addition, quantities such as the average beam current are determined on a run-by-run basis, though accelerator issues or special studies may cause the beam current to be varied throughout a run.

The data contained in the .dat files for each run can be broken into three distinct categories, as described below.

- **EPICS:**

  The slow control software used at JLab is called the Experimental Physics and Industrial Control System (EPICS) [67]. Data that is fed into the EPICS data stream are read out either every 2 or every 30 seconds. This can include information like the beam energy, target temperatures, target pressures, magnet set and readback currents, and the spectrometer angle.

- **Scalers:**

  Scaler data are read out every 2 seconds or 1000 triggers, whichever comes first. This data consists of many counters, most of which keep track of the number of times each of the pre-triggers fires. However, these data also include information on the beam current from the BCMs. The scalers are not impacted by the DAQ dead time and are therefore used to determine and correct for it, as will be discussed in the next chapter.

- **Physics:**

  Physics data are read out on a trigger-by-trigger basis. These data contain information about the signals from the detectors that were fed into the fADCs and TDCs, as well as higher-level quantities derived from this information.

2.6 Targets

To investigate the nuclear dependence of the EMC effect, experiment E12-10-008 collected electron scattering data on twenty-five different targets. Of these, twenty-two were dedicated nuclear targets, and three were specially designed targets used to align the beam and perform systematic studies. Furthermore, of the dedicated nuclear targets, four were composed of a cryogenic fluid encased in an aluminum

Target	Thickness (g/cm^2)	Chem. Purity (wt%)	Enrichment (at%)
^{6}Li	0.225 ± 0.0008	99.9	95
^{7}Li	0.254 ± 0.003	99.99	99.88
^{9}Be	0.986 ± 0.003	99.5	NAT
$^{10}B_4C$	0.576 ± 0.002	99.99	96.6
$^{11}B_4C$	0.633 ± 0.002	99.99	99.8
^{12}C	0.574 ± 0.002	99.99	NAT
^{27}Al	0.460 ± 0.001	99.9	NAT
^{40}Ca	0.785 ± 0.003	99.99	99.97
^{48}Ca	1.051 ± 0.003	99.99	90.04
^{48}Ti	0.294 ± 0.001	99.99	NAT
^{54}Fe	0.367 ± 0.001	99.99	97.68
^{58}Ni	0.2408 ± 0.0004	99.9	99.5
^{64}Cu	0.942 ± 0.003	99.999	NAT
^{64}Ni	0.2607 ± 0.0005	99.9	95
^{108}Ag	0.528 ± 0.002	99.9	NAT
^{119}Sn	0.4562 ± 0.0006	99.75	NAT
^{197}Au	0.4047 ± 0.0006	99.9	NAT
^{232}Th	0.409 ± 0.001	99.5	NAT

Table 2.4: Specifications for the solid targets used during E12-10-008. For targets that were not isotopically enriched, the mass number of the target is taken to be the natural abundance-weighted average mass number of the element, rounded to the nearest integer.

alloy shell (AA7075), and the other eighteen were solid. Specifications for these solid and cryogenic targets can be found in Tab. 2.4 and Tab. 2.5, respectively. In addition, Tab. 2.6 has the specifications for the aluminum alloy shell of the cryogenic targets. The three specially designed targets are discussed at the end of this section.

The targets were installed onto one of two target ladders. In each of the target ladders, the targets are aligned vertically along the pivot axis of the spectrometers. The cryogen in the cryogenic targets is constantly kept flowing in a loop between the target chamber and a heat exchanger to keep it cool. However, the density of the cryogen around the beam line can vary due to the heat deposited by the electron beam. Therefore, dedicated measurements are made at various beam currents to allow one to account for these density fluctuations (see Sec. 3.9.2). The solid targets are cooled via conduction with the target ladder to avoid melting.

Because only one ladder can be installed in the target chamber at a time, one of the ladders was used for the first half of the experiment and the other was swapped in for the second half. The active ladder is connected to a vertical motion system that is controlled remotely from the Hall C counting room using the target control GUI. The target control GUIs for each of the target ladders are shown in Figs. 2.16 and 2.17. The target control GUI can be used to set the vertical position of the ladder such that a particular target is placed into the beam line. This system allows the target to be changed in just a few minutes. To avoid damaging the target ladder, target changes must only be done when the beam is not being sent into the hall. In addition to controlling the motion of the target ladder, the target control GUI is also used to control and monitor the status of the cryogenic targets.

In addition to being connected to the vertical motion system, the active target ladder is installed in the Hall C target chamber, shown in Fig. 2.18. The Hall C target chamber is an aluminum cylindrical tank with an inner diameter of 41 inches and 2-inch thick walls (resulting in an outer diameter of 45 inches). The inside of the tank is kept at near-vacuum (around 10^{-6} or 10^{-7} mbar) during experimental

Target	Length (mm)	Nom. Pressure (PSIA)	Nom. Temperature (K)
^{1}H	99.98 ± 0.01	26	19
^{2}H	99.98 ± 0.01	26	22
^{3}He	99.98 ± 0.01	55	5.6
^{4}He	99.98 ± 0.01	113	5.6

Table 2.5: Specifications for the cryogenic targets used during E12-10-008. The length of the target cell is measured at room temperature and includes the thickness of the aluminum alloy 7075 shell. Therefore, when determining the areal thickness (g/cm^2) of the cryogen, one must subtract the thickness of the shell and account for the contraction of the target due to the temperature difference.

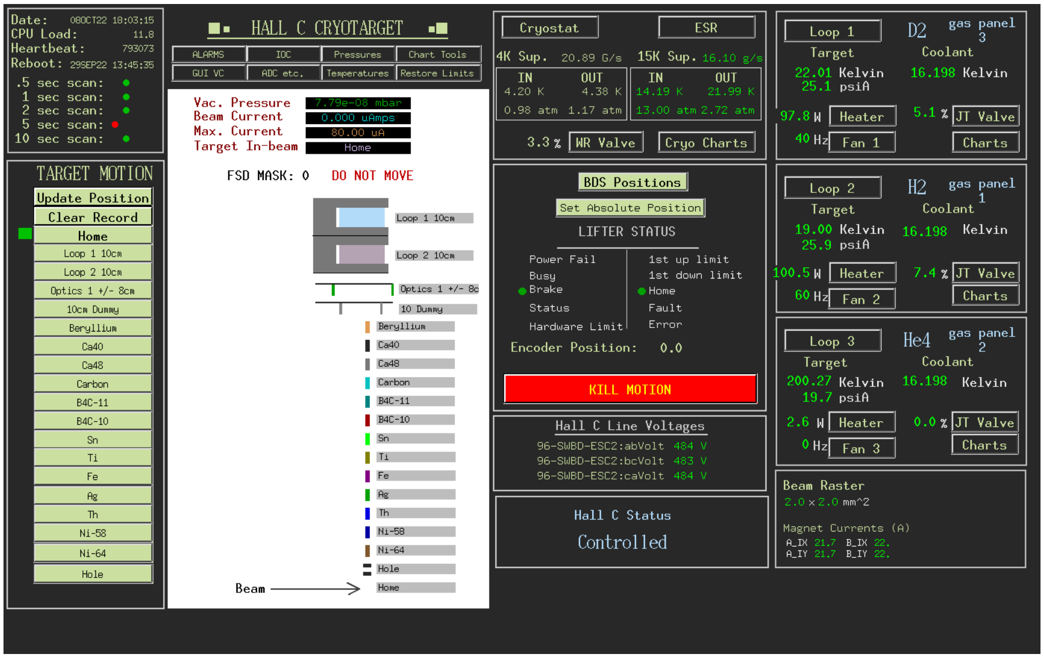

Figure 2.16: The target control GUI for the first target ladder. The target position can be set by selecting the desired target from the list on the left-hand side. The panels on the right-hand side contain the controls and statuses of the cryogenic targets. On this ladder, cryogenic loop 1 contained liquid deuterium (^{2}H nuclei), and loop 2 contained liquid hydrogen (^{1}H nuclei).

running. The electron beam enters the target chamber from the beam line via the entrance beam pipe. The vast majority of these electrons pass straight through the target material with minimal deflection, exiting the target chamber via the beam exit pipe and heading to the beam dump.

For the electrons that are significantly deflected, a thin window composed of 0.020-

Target	Entrance (mm)	Exit (mm)	Right (mm)	Left (mm)
^{1}H	0.264 ± 0.082	0.208 ± 0.035	0.444 ± 0.015	0.329 ± 0.007
^{2}H	0.168 ± 0.009	0.2024 ± 0.056	0.462 ± 0.011	0.330 ± 0.008
^{3}He	0.168 ± 0.009	0.2024 ± 0.056	0.462 ± 0.011	0.330 ± 0.008
^{4}He	0.264 ± 0.082	0.208 ± 0.035	0.444 ± 0.015	0.329 ± 0.007

Table 2.6: Specifications for the aluminum alloy 7075 shells that encased the cryogenic targets.

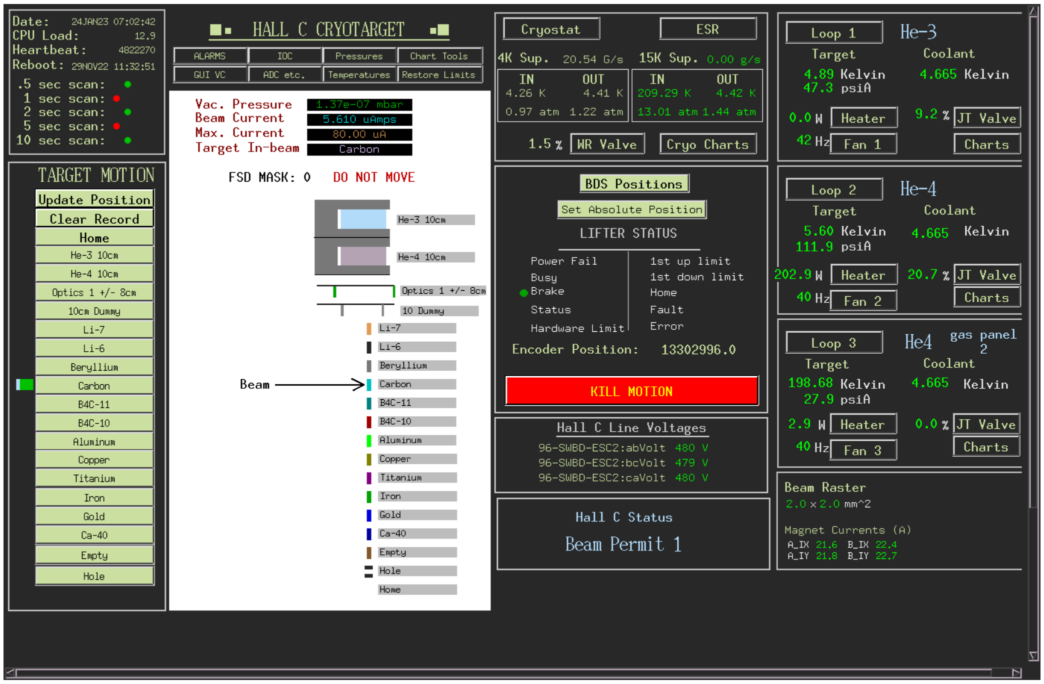

Figure 2.17: The target control GUI for the second target ladder. The display is identical to that of the first target ladder apart from the targets listed. On this ladder, cryogenic loop 1 contained ^{3}He gas, and loop 2 contained ^{4}He gas.

inch thick 2024-T3 aluminum forms the section of the target chamber wall between the target ladder and possible spectrometer entrances. This window allows the scattered electrons to exit the target chamber with minimal interference. The electrons within the set angular acceptance of the spectrometer then pass through a small section of air before entering one of the spectrometers. This physical separation between the spectrometer and the target chamber is done to allow the spectrometers to rotate about the target without coupling to the target chamber and beam line vacuum.

The 3 other targets that were used were the aluminum alloy 7075 dummy, carbon optics, and hole targets. These targets are described below:

- **Aluminum Alloy 7075 Dummy:**

  The aluminum alloy 7075 dummy target is composed of two AA7075 foils separated by 10 cm, with the front and back foils approximately aligned with the

Figure 2.18: Picture of the target ladder installed in the Hall C target chamber during the alignment process from [68]. During this process, the solid target portion of the ladder only contained the hole target to prevent exposure of the other targets to air.

entrance and exit windows of the AA7075 shell that holds the cryogenic targets. This target is used to estimate the background caused by the AA 7075 shell of the cryogenic targets. The entrance and exit dummy target foils are 0.240 ± 0.003 g/cm^2 and 0.236 ± 0.003 g/cm^2, respectively. This is approximately 4 times thicker than the corresponding windows of the cryogenic target shells. This is done to match the radiation length of the dummy target to that of the cryogenic targets, causing both to experience similar external radiative effects.

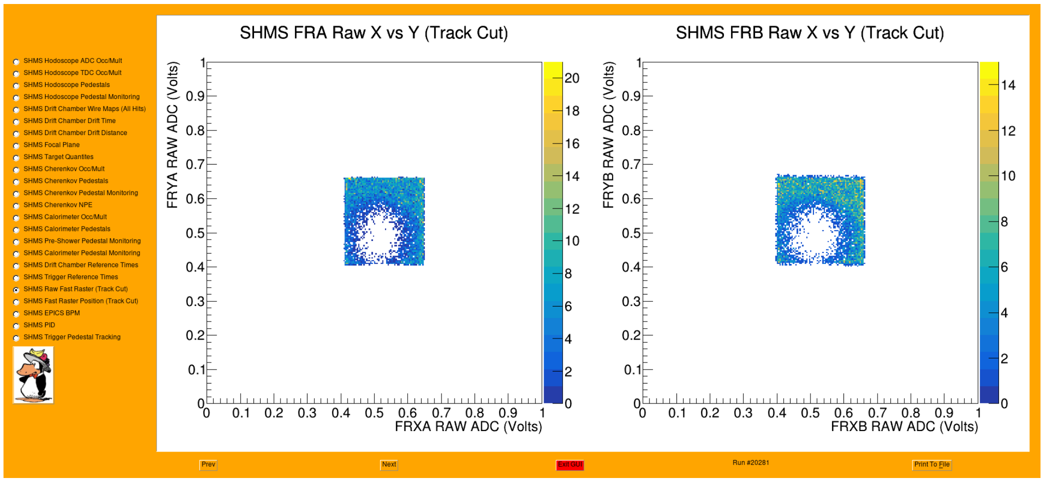

Figure 2.19: Raster pattern with the carbon hole target roughly centered on the beam. The electrons that pass straight through the hole in the target are not scattered and therefore not detected by the spectrometer, while the electrons that hit the rest of the target are detected.

- **Carbon Optics:**

  The carbon optics target consists of two carbon foils: one located 8 cm upstream of the spectrometer pivot axis and the other located 8 cm downstream of it. This target is used to provide data to perform the optics calibrations for each of the spectrometers. This calibration allows one to reconstruct the scattering angle and momentum of a detected particle as it exited the target material given its track through the spectrometer as measured by the drift chambers.

- **Carbon Hole:**

  The hole target consists of a thin carbon foil with a 2 mm circular hole in the middle. With the beam rastered to at least 2.00 mm $\times$ 2.00 mm, this target is used to locate and center the beam position on the target ladder. A hole appears in the raster pattern where electrons simply pass through the hole in the foil and are not scattered into the spectrometer. The centering of the beam position on the target ladder is performed by adjusting the beam position until the hole in the raster pattern is centered. An example of a raster pattern with the beam centered on the hole is shown in Fig. 2.19.

Chapter 3

Data Analysis

This chapter covers the data analysis procedure that was used to obtain the results shown in Ch. 4. This includes setting the proper reference times and timing windows, performing detector calibrations and efficiency studies, estimating backgrounds, and comparing data to Monte Carlo simulations to extract cross sections.

3.1 Reference Times

As discussed in a previous chapter, when the Level 1 (L1) accept trigger is caused to fire by one of the pre-triggers, it is sent to the readout controllers (ROCs) to initiate the writing of data from all of the fADCs and TDCs. This L1 accept trigger operates at a clock rate of 40 MHz, which corresponds to a 25 ns timing resolution. In addition, the L1 accept trigger has an intrinsic 4 ns jitter, causing the timing resolution to be 29 ns. To measure the arrival time of the raw detector signals using the full 10 GHz (0.1 ns) resolution of the TDCs, a time with a higher resolution than the L1 trigger time must be used as a reference. For this experiment, the HMS reference time is a copy of the hHODO 3/4 pre-trigger that is sent to all fADC and TDC modules. The reference time is then measured against the 10 GHz clock of the TDCs, which allows it to be used to correct for the jitter introduced by the coarse timing resolution of the L1 accept trigger. One can then recover the 0.1 ns resolution of the arrival time of the detected signal by taking the difference between it and the corresponding reference

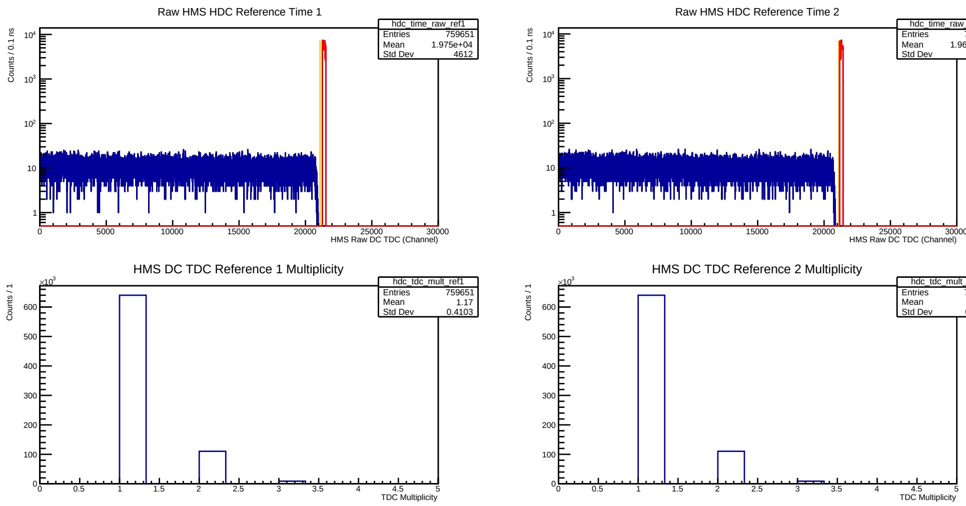

Figure 3.1: Two raw HMS drift chamber reference time spectra for a run using the hHODO 3/4 trigger. The histograms in the top plots show the raw reference time counts as a function of TDC channel (0.1 ns), while the bottom plots show the multiplicity - the number of hits within the trigger readout window. The red and blue histograms correspond to the TDC times with and without a multiplicity cut requiring only one hit in the time window. The vertical yellow lines in the top plots are the reference time cuts that were selected for use in further analysis. The small gap between the random coincidences (blue) and the good reference time peak (red) is likely due to electronic dead time. This dead time introduces a minimum time interval between the occurrence of a valid trigger (corresponding to a good reference time) and a random coincidence.

time.

Due to random coincidences (especially at high rates), more than one reference time “hit” may occur during the read-out window of a single accepted trigger. To ensure that the proper reference times, those corresponding to the trigger, are selected to correct the raw times, one must set reference time cuts. Without any cuts applied, the analyzer defaults to setting the first hit within the window to the reference time; on the other hand, with the cut applied, the analyzer selects the first hit occurring after the cut as the reference time. Histograms of the raw uncorrected TDC times and fADC pulse times are shown in Fig. 3.1. The cuts are set just before the sharp peaks, significantly increasing the probability that the proper reference time is selected. If

```
; Cut to select the Reference time when multiple hits in reference time
; This file is for ELREAL and ELCLEAN triggers
; The units in channels for the module (CAEN tdc or FADC)
; negative value refcut means that the first reference time greater than the abs(refcut)
;     is used as reftime. If no ref time is found  greater than the abs(refcut) then first
;     reference time is used.
; positive value refcut means that the first reference time greater than the abs(refcut)
;     is used as reftime. If no ref time is found  greater than the abs(refcut) then no
;     reference time is used and warning message is produced.
; Cut is on reference time per detector.
;
; NOTE: These are integers, not floats

; cut variable = hDCREF2
hdc_tdcrefcut=-20200
; cut variable = hT2
hhodo_tdcrefcut=-1100
; cut variable = hFADC_TREF_ROC1
hhodo_adcrefcut=-2200
hcer_adcrefcut=-2200
hcal_adcrefcut=-2200
```

Figure 3.2: Reference time parameter file used for the HMS hEL_REAL and hEL_CLEAN runs. The cuts are set to negative values which, as noted in the parameter file, means that if no hit is found after the reference time cut, the first hit is used instead.

there is no hit present after the cut, one can choose to either use the first hit or not use a reference time at all for that event.

The reference time spectra were found to peak at different times when comparing runs that used hHODO 3/4 as the trigger and runs that used either hEL_REAL or hEL_CLEAN as the trigger. This occurred due to small differences in the time that each of the triggers fires. To account for this, two sets of cuts were used: one for runs taken using the hHODO 3/4 trigger, and another for runs taken using either the hEL_REAL or hEL_CLEAN trigger. The file containing the cuts used for the hEL_REAL or hEL_CLEAN runs is shown in Fig. 3.2. The peak times were otherwise found to be consistent over the course of the experiment. This was expected since no changes were made to the trigger logic or relevant hardware during this time.

3.2 Timing Windows

The next step in the analysis process is determining the timing window cuts. These timing window cuts help to remove background hits in the fADCs and TDCs that occurred within the readout window, which is relatively wide compared to the typical time distribution of good hits. For the hodoscope, the timing window cuts were made on a PMT-by-PMT basis on the difference between the fADC pulse time and TDC time for each of the hits. This difference should be constant for good physics events (apart from differences due to finite timing resolution) because both the fADC and TDC times originate from a good event (not background, cross-talk, etc.) and are therefore derived from the same input signal. For the calorimeter and Cherenkov detectors, the timing window cuts were also made on a PMT-by-PMT basis, however, they used the difference between the hodoscope time projected to the spectrometer's focal plane (HodoStartTime) and the fADC time. This difference should also be roughly constant for true events following the same argument that was made for the hodoscope, provided that the time-of-flight (TOF) of the particle between the hodoscope and the other detector (calorimeter or Cherenkov) is also approximately constant. These definitions are summarized as

$$\text{AdcTdcDiffTime} = \text{TdcTime[pmt][hit] - AdcPulseTime[pmt][hit]} \tag{3.1}$$

for the hodoscope PMTs, and

$$\text{AdcTdcDiffTime} = \text{HodoStartTime - AdcPulseTime[pmt][hit]} \tag{3.2}$$

for the calorimeter and Cherenkov PMTs. A sample AdcTdcDiffTime spectrum for one of the two HMS Cherenkov PMTs with cuts overlayed is shown in Fig. 3.3.

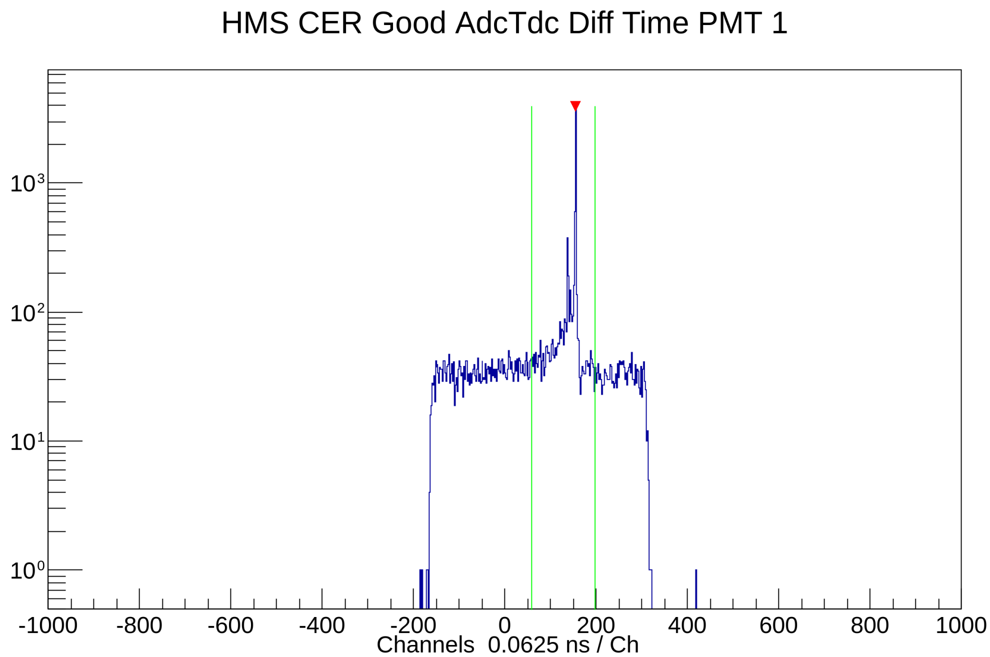

Figure 3.3: Difference between the fADC pulse time and hodoscope time for the HMS Cherenkov PMT 1. The vertical green lines show the cuts that were made on the fADC-TDC time difference for all subsequent analyses. These cuts are intentionally kept loose to minimize the risk of removing potentially good events, as any remaining bad events will be removed by subsequent cuts.

The timing window cuts for the drift chambers were made on a plane-by-plane basis using the raw TDC times. A sample drift time spectrum for one of the HMS drift chambers is shown in Fig. 3.4 along with the timing window cuts used. The drift time spectra for all twelve planes were found to be very similar, therefore one set of cuts was used for all twelve planes.

3.3 HMS Detector Calibrations

Now that the reference time and timing window cuts have been set, the next step in the analysis process is to perform the HMS detector calibrations. This section will cover the calibrations for the HMS hodoscopes, drift chambers, Cherenkov, and

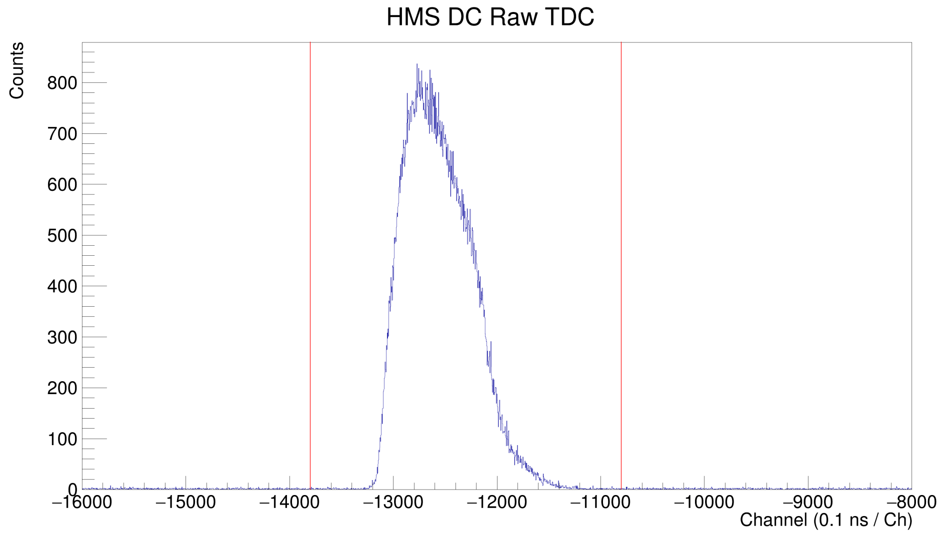

Figure 3.4: Raw TDC time spectrum for the U plane in the front HMS drift chamber. The timing window cuts are shown as vertical red lines. The spectra for all twelve planes were found to overlap almost entirely, so these cuts were used for all planes. The broad shape of the drift chamber TDC time spectrum is caused by the distribution of drift times. A drift time is the interval between when an ionizing particle passes through the drift chamber and when its signal is picked up by a sense wire. This time is a function of the distance between where a particle passes through the drift chamber and the nearest sense wire.

calorimeter.

3.3.1 Hodoscope Calibrations

The purpose of the hodoscope calibration is to determine the corrected TDC time t_{Corr}, representing the time that the particle passed through and produced a signal in the scintillator paddle. In general, this can be written as

$$t_{Corr} = t_{raw} - t_{TW} - t_{cable} - t_{prop.} - t_{\lambda} \ , \tag{3.3}$$

where t_{raw} is the raw TDC time, t_{TW} is the time-walk correction, t_{cable} is the correction accounting for the time it takes for the signal to propagate from the PMT to the TDC,

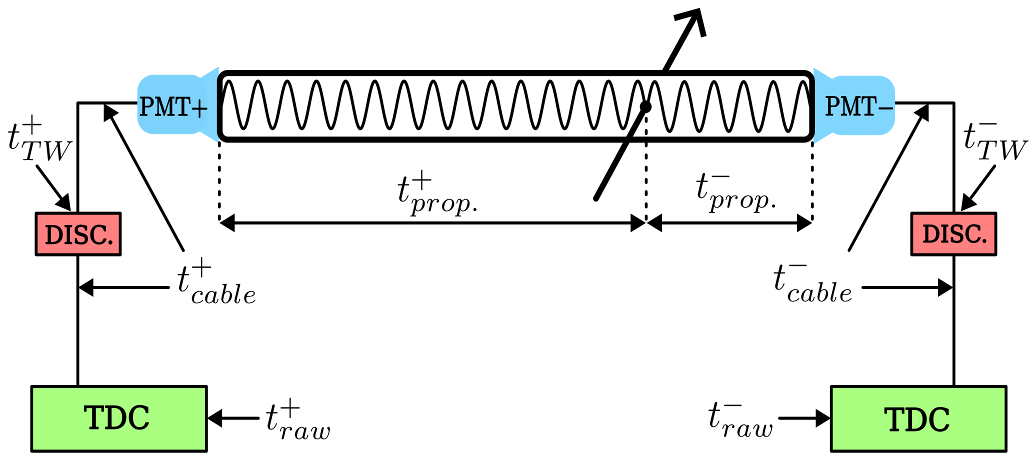

Figure 3.5: Illustration of the individual components of the hodoscope timing correction. Using the raw TDC times, these corrections allow one to determine the times that particles passed through the scintillator paddle.

t_{prop} is the correction accounting for the time it takes for the signal to propagate from its point of origin inside the scintillator paddle to the PMT at the edge, and t_{λ} accounts for any remaining time difference between individual scintillator paddles. These general timing corrections are illustrated in Fig. 3.5.

- **Time-Walk Correction:**

  When an analog pulse passes through a leading-edge discriminator, a logic signal is output when the amplitude of that pulse exceeds some threshold voltage. This causes the time of the output logic signal to be dependent not only on the pulse arrival time but also on the pulse amplitude since a higher amplitude pulse will cross the threshold voltage sooner than a lower amplitude pulse. This effect that the pulse amplitude has on the timing of the output signal, illustrated in Fig. 3.6, is known as time-walk. This time-walk effect has a non-negligible impact on the time read-out by our TDCs and must be corrected for in our analysis.

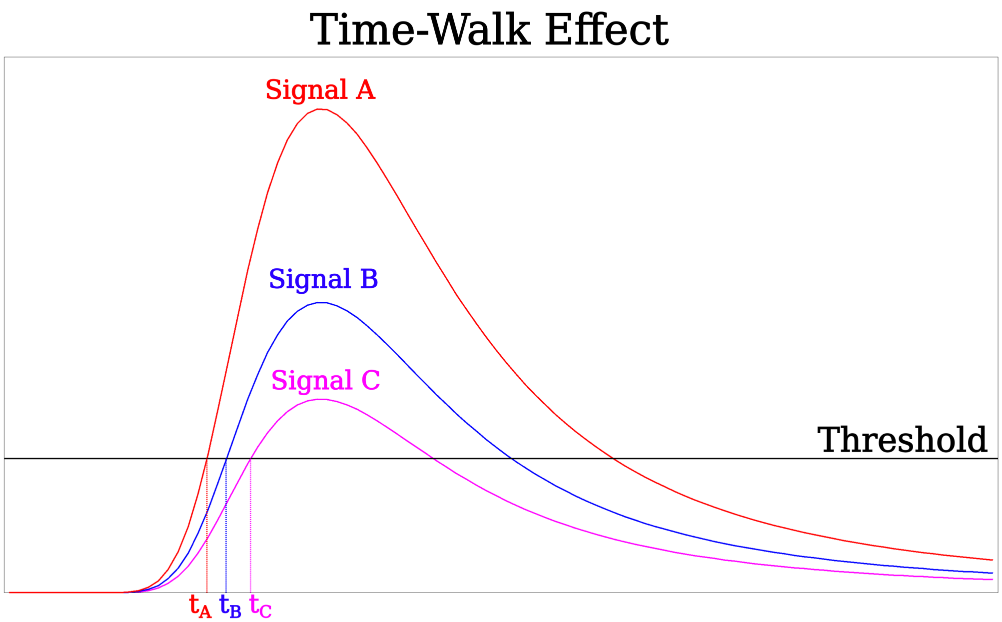

Figure 3.6: Visualization of the time-walk effect. As the amplitude of the signal increases, the time at which it crosses the discriminator threshold decreases relative to its peak.

Fortunately, the method used to determine the pulse time on the fADCs is not sensitive to the signal amplitude. This pulse time is defined as the time at which the pulse's voltage crosses some constant fraction of its maximum amplitude. Therefore, given that the pulse shape is consistent, the fADC provides an amplitude-independent measure of the pulse time. One can then plot the difference between the hodoscope ADC and TDC times as a function of the pulse amplitude, fit away the time-walk effect, and recover the corrected TDC time. The fit function used is

$$f_{TW}(A) = c_1 + \frac{1}{(\frac{A}{TDC_{Thrs}})^{c_2}} \tag{3.4}$$

where A is the pulse amplitude, c_1 and c_2 are the fitting parameters, and TDC_{Thrs} is the TDC threshold voltage. Figure 3.7 shows the fADC-TDC

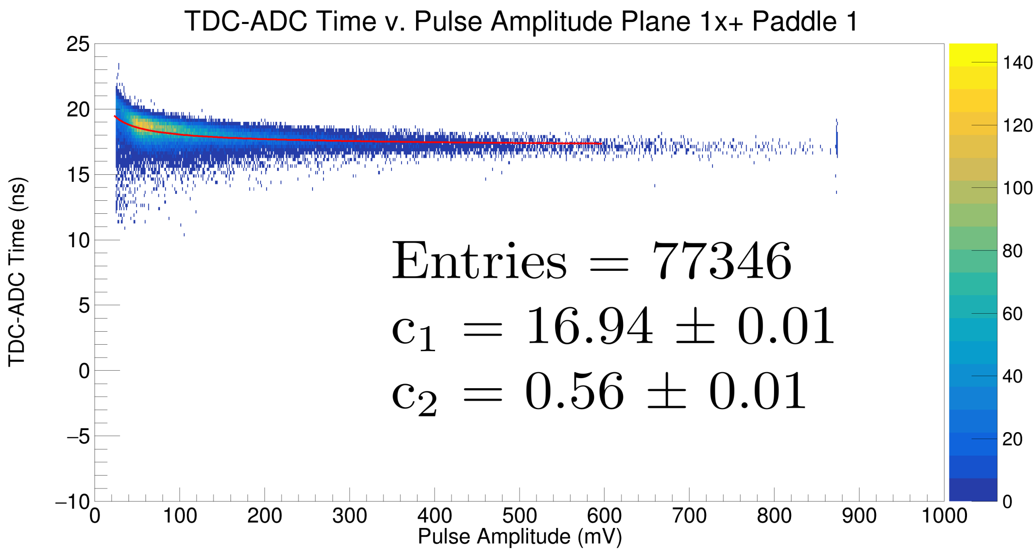

Figure 3.7: Difference between fADC and TDC times plotted against pulse amplitude for the positive side PMT of paddle 1 in the 1x plane of the hodoscope. This distribution is fit to remove the effect of time-walk, with the fitted results c_1 and c_2 of Eq. 3.4 shown within the figure.

time difference plotted as a function of the fADC pulse amplitude for a single hodoscope PMT before the time-walk correction is applied. Applying this correction to the TDC time removes the amplitude dependence of the fADC-TDC time difference. This also allows one to use the TDC time, which is more precise than the pulse time output by the fADC, in further analysis.

- **Cable Time Offset and Propagation Velocity in the Scintillator:**

  The next step in the hodoscope calibration procedure is to determine the cable time offset and the signal propagation velocity in the scintillator for each of the paddles: t_{cable_offset} and v_p.

  To determine these values, half of the difference between the time-walk corrected TDC times for the positive and negative PMTs of a single scintillator paddle is plotted against the position the particle passed through the paddle. Half of the TDC time difference is taken because, for every unit the track position moves towards one PMT, it also moves a unit away from the other PMT. This causes the time difference between the two PMTs to grow twice as quickly as the time it takes for the signal to propagate from the track position to the center of the scintillator. Therefore, to more directly extract the propagation velocity from this plot, half of the TDC time difference is used. The track position is determined using the tracking information from the drift chambers. Once this data has been plotted, it is then fit to extract the propagation velocity and difference between the positive and negative PMT cable times using the function

$$f(y_{track}) = \frac{1}{v_p} y_{track} + b_0 \ , \tag{3.5}$$

where y_{track} is the y-position of the particle along the scintillator centered at $y = 0$, v_p is the propagation velocity of the signal in the scintillator, and b_0 is half of the cable time difference between the positive and negative sides. A sample plot showing this data with the above fit overlayed is shown in Fig. 3.8.

- **Hodoscope Paddle Time Difference Corrections:**

  The final step in the hodoscope calibration procedure is to determine t_λ for each of the hodoscope paddles. Consider an event where a single charged particle passes through all four hodoscope planes. One would expect the difference in the TDC times read out from any two struck paddles in different planes to be equivalent to the time it took for the particle to traverse between them. However, the corrections described above aren't totally sufficient, and additional time offsets exist between hodoscope paddles. These offsets are accounted for by applying the t_λ correction for each hodoscope paddle.

  First, a cut is made to ensure that one and only one hodoscope paddle receives a hit in each of the hodoscope planes for an event. Then, the TDC time difference

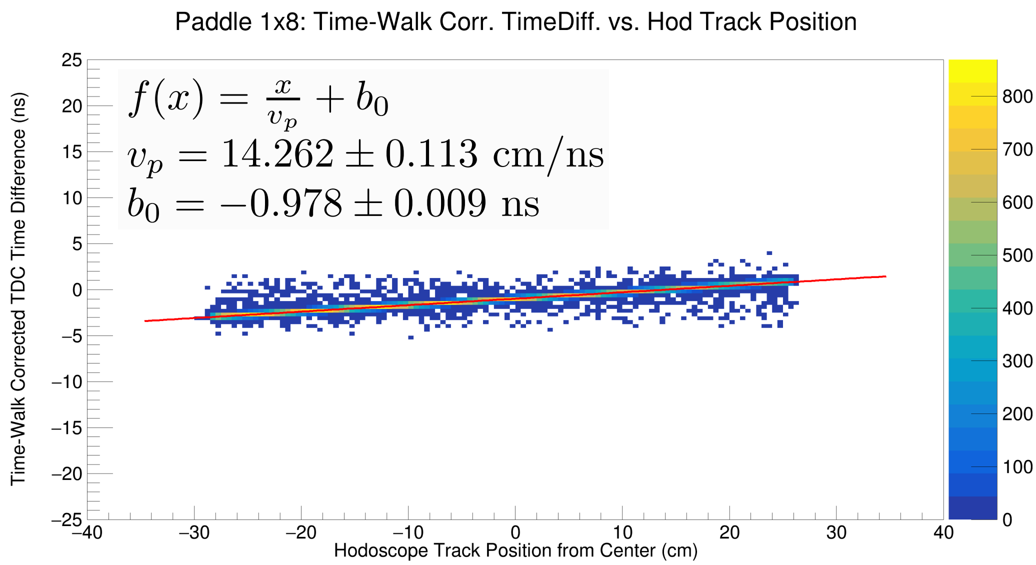

Figure 3.8: Half of the TDC time difference between the positive and negative sides of a hodoscope paddle plotted against the position the particle passed through that paddle. This distribution is fit to determine the propagation velocity of the signal produced by the particle in the scintillator and the difference between the positive and negative side cable propagation times.

is formed for six combinations of paddles in different planes, as shown in Fig. 3.9.

For this calibration, the measured TDC time for each paddle is defined as the average time walk and cable time corrected TDC times of the positive and negative sides, written as

$$t_i = \frac{T^{+}_{TW} + T^{-}_{TW} - 2 \times t_{cable\_offset}}{2} \ , \tag{3.6}$$

where $T^{+(-)}_{TW}$ is the positive (negative) side time walk corrected TDC time. The "true" time difference between two paddles in different planes can then be written as

$$(t_i + t_{\lambda i}) - (t_j + t_{\lambda j}) = \frac{D_{ij}}{v} \ , \tag{3.7}$$

where $t_{\lambda i(j)}$ is the t_λ correction for the i (j) PMT, D_{ij} is the distance between

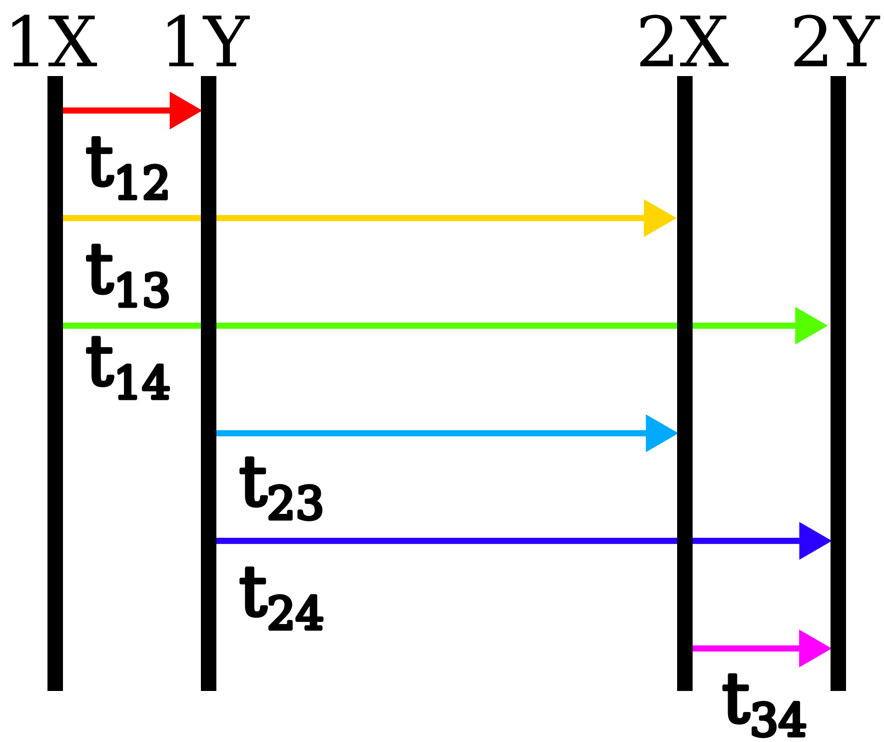

Figure 3.9: Sketch of the HMS hodoscope planes showing the time differences used to determine the t_λ corrections.

the points at which the particle crossed the planes of the i and j paddles as determined by the tracking, and v is the velocity of the particle. The time differences between the hodoscope paddles as defined in Fig. 3.9. We can then use Eq. 3.7 to define the time difference between two paddles that is not due to the time it took for the particle to traverse between them as

$$t_{\lambda_i} - t_{\lambda_j} = \frac{D_{ij}}{v} - (t_i - t_j) \equiv b_{ij} \ . \qquad (3.8)$$

This gives six b_{ij} for one event, one for each pair combination of the four paddles. Forming these differences for many events, one can set up a system of 52 linear equations, one for each hodoscope paddle, to solve for each of the 52 $t_{\lambda i}$ as

$$\begin{bmatrix} c_{1,1} & c_{1,2} & \dots & c_{1,51} & c_{1,52} \\ c_{2,1} & c_{2,2} & \dots & c_{2,51} & c_{2,52} \\ \vdots & \vdots & \ddots & \vdots & \vdots \\ c_{51,1} & c_{51,2} & \dots & c_{51,51} & c_{51,52} \\ c_{52,1} & c_{52,2} & \dots & c_{52,51} & c_{52,52} \end{bmatrix} \begin{bmatrix} t_{\lambda 1} \\ t_{\lambda 2} \\ \vdots \\ t_{\lambda 51} \\ t_{\lambda 52} \end{bmatrix} = \begin{bmatrix} b_1 \\ b_2 \\ \vdots \\ b_{51} \\ b_{52} \end{bmatrix} , \tag{3.9}$$

where b_m is defined as

$$b_m = \sum_{n=m}^{52} b_{mn} - \sum_{n=1}^{m} b_{nm} , \tag{3.10}$$

and c_{mn} is the corresponding coefficient in front of the $t_{\lambda n}$ term obtained after performing the same operations that were used to form b_m on the left-hand side of Eq. 3.8.

For example, consider forming a matrix from two calculated time differences, $b_{1,20}$ and $b_{20,40}$. We would then obtain

$$\begin{bmatrix} 1 & \dots & -1 & \dots & \dots & \dots \\ \dots & \dots & \dots & \dots & \dots & \dots \\ -1 & \dots & 2 & \dots & -1 & \dots \\ \dots & \dots & \dots & \dots & \dots & \dots \\ \dots & \dots & -1 & \dots & 1 & \dots \\ \dots & \dots & \dots & \dots & \dots & \dots \end{bmatrix} \begin{bmatrix} t_{\lambda 1} \\ \vdots \\ t_{\lambda 20} \\ \vdots \\ t_{\lambda 40} \\ \vdots \end{bmatrix} = \begin{bmatrix} b_{1,20} \\ \vdots \\ b_{20,40} - b_{1,20} \\ \vdots \\ -b_{20,40} \\ \vdots \end{bmatrix} , \tag{3.11}$$

with all other elements being 0. This system of equations is then solved numerically using Singular Value Decomposition (SVD). Paddle 7 (1x7) is used as the baseline, meaning that row 7 and column 7 of the coefficient matrix are set to 0 (along with b_7) before performing the SVD (otherwise, without setting a reference paddle, a uniform offset of all $t_{\lambda n}$ would also be a solution due to the linear dependence of the functions).

Once the full hodoscope calibration procedure is complete, it is important to verify that the calibration worked as intended. One plot that is examined is a 2D histogram that shows particle velocity, as determined by the hodoscopes, plotted against the focal plane position of the particle, shown in Fig. 3.10. For a dataset consisting primarily of GeV energy electrons, a good calibration would result in a histogram whose distribution is a Gaussian that peaks near $\beta = \frac{v}{c} = 1$ at all focal plane positions. A poor calibration may have a β peak significantly offset from 1, or a β distribution that varies as a function of hodoscope position. This variation would appear as sharp discontinuities at positions corresponding to the boundaries between individual hodoscope paddles.

The hodoscope calibration coefficients determined throughout the experiment were found to be stable enough for our purposes to allow us to use a single set of coefficients to analyze all of the data.

3.3.2 Drift Chamber Calibrations

As discussed in Sec. 2.4.2, when a charged particle passes through the drift chambers, a track of ionized atoms is left in its wake. The freed electrons then accelerate in the electric field toward the nearest positive potential wire. As the electron travels toward the wire, a Townsend Avalanche is formed, resulting in a signal being produced once the avalanche reaches the wire. The delay between the time that a charged particle passes through a drift chamber and when a signal is produced in one of the wires is known as the drift time. This drift time can be used to determine the distance at which a charged particle passes by the wire, known as the drift distance. This allows

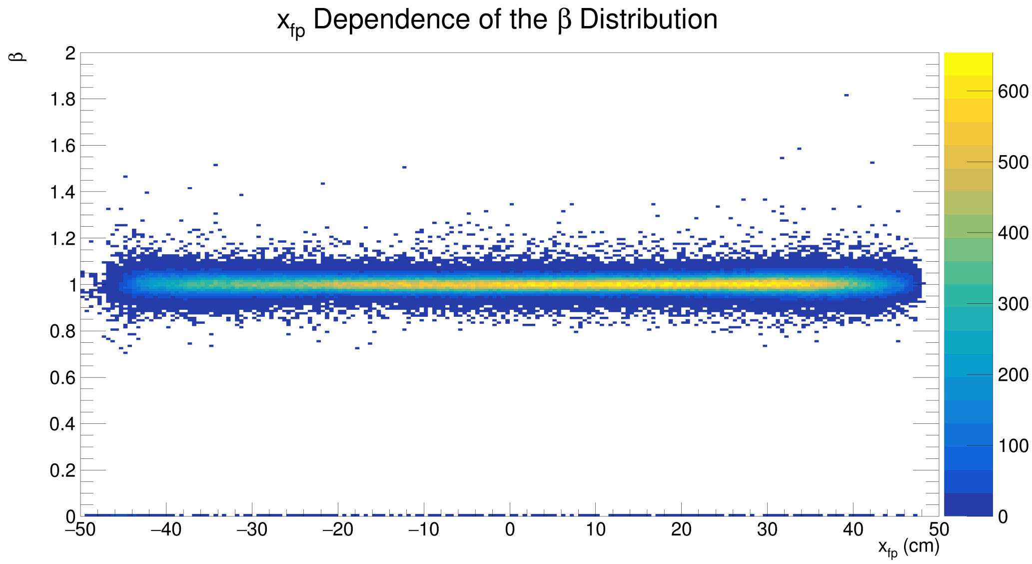

Figure 3.10: Diagnostic plot for the hodoscope calibration. Using a dataset consisting primarily of electrons at 4 GeV, β is plotted against the x-position of particle tracks at the focal plane (x_{fp}). The β distribution is peaked at 1 at all x_{fp}, and no discontinuities due to individual poorly calibrated paddles are observed. The spread in the β distribution is primarily due to the timing resolution of the hodoscopes rather than actual variations in the velocities of the detected particles.

for more precise tracking than possible from a simple wire chamber with the same wire spacing. The goal of the drift chamber calibration is to produce the mapping from drift times to the drift distances.

The first step in the drift chamber calibration procedure is to determine a quantity known as the t_0 offset. This offset corresponds to the TDC time of a particle that passed directly through one of the wires, having no drift time. Once this offset is applied to the TDC time spectrum, the corrected TDC time of a particle passing directly through the wire will be zero ($t_0 = 0$). It was noticed that the overall offset of the drift time spectrum tended to shift over time, therefore, this offset was monitored and updated with every kinematic change. This offset was determined per discriminator card, with each card containing up to 16 wires. The overall timing offset per card was determined using a linear fit to the rising edge of the drift time

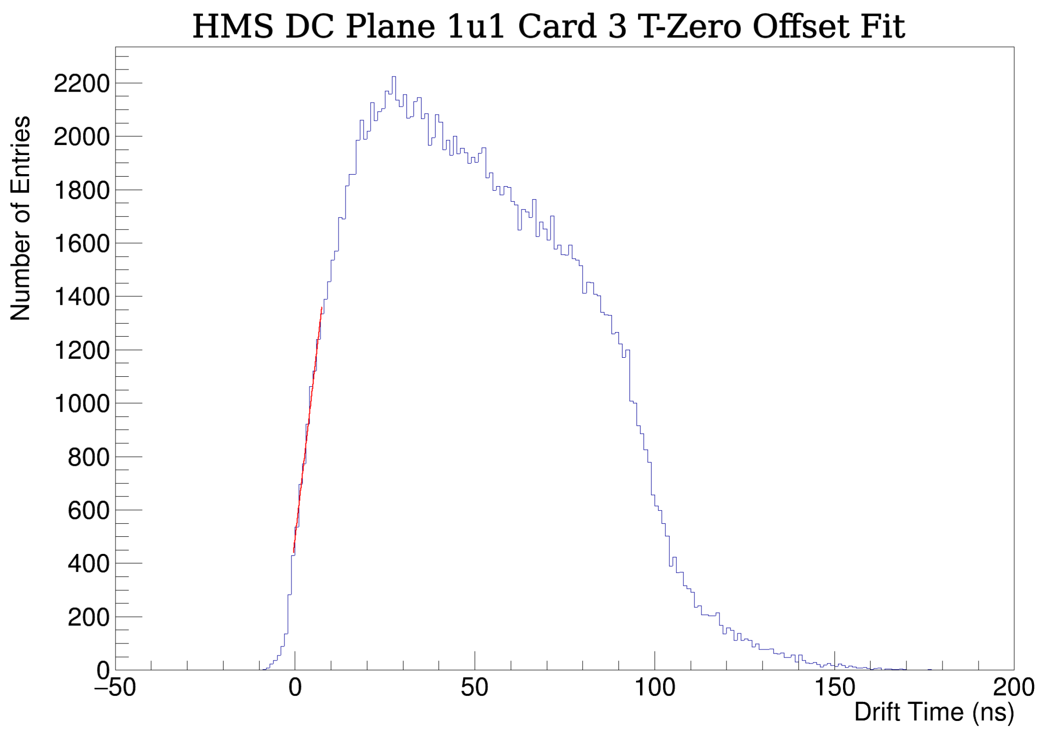

Figure 3.11: Sample drift time distribution with the linear fit used to extract the t_0 offset overlayed in red. To extract the t_0 offset, the fit line is extrapolated to the x-axis to determine the x-intercept. This intercept is used as the offset.

distribution, as shown in Fig. 3.11. This fit was then extrapolated to the horizontal axis, with the t_0 offset corresponding to the x-intercept.

Once the overall drift time offset has been set such that $t_0 = 0$, we can create the map to convert from these corrected drift times to drift distances, using the fact that the drift distances should be approximately uniformly distributed from 0 cm to 0.5 cm (the spacing between wires). The events should be uniformly distributed because particles have no preferred distance at which to pass between two wires, and, for sufficiently small wire spacing, the variation in the rate of events is approximately linear as a function of position, leading to a uniform drift distance spectrum. With this, we can form a mapping between drift times and drift distances using the equation

$$d_{drift}(t_{drift}) = \Delta \frac{\int_{t_0}^{t_{drift} \leq t_{max}} F(\tau) d\tau}{\int_{t_0}^{t_{max}} F(\tau) d\tau} , \tag{3.12}$$

where d_{drift} is the drift distance, t_{drift} is the drift time, Δ is the nominal width of the drift distance distribution which is equal to the wire spacing (0.5 cm), $F(\tau)$ is the drift time distribution, and t_{max} is the maximum drift time.

Due to the finite precision of the TDC time, Eq. 3.12 is implemented in practice using a finite sum, not an integral. In addition, the integral in the denominator of Eq. 3.12 is the total number of counts in the drift time distribution, which we can write as N_{tot}. With this, the practical implementation of the drift time to drift distance map can be written as

$$d_{drift}(t_{drift}) = \Delta \frac{1}{N_{tot}} \sum_{bin(t_0)}^{bin(t_0+t_{drift})} F(n) , \tag{3.13}$$

where $F(n)$ is the number of counts in the n^{th} bin. One of these time-to-distance maps is made for each of the wire planes, resulting in a total of 12 maps.

To verify that the calibration worked as intended, one can analyze the data that was used for the calibration with the new t_0 offsets and time-to-distance maps applied, and plot the drift distance spectra for each of the wire planes. If the calibration worked as intended, it will by definition result in a uniform drift distance spectrum, as shown in Fig. 3.12.

Unlike the hodoscope calibration, the drift chamber calibration coefficients were found to not be stable enough to allow us to use a single set of calibration constants to analyze data over the entire run period. Therefore, a unique set of calibration constants was used for each kinematic setting, resulting in over 100 sets in total.

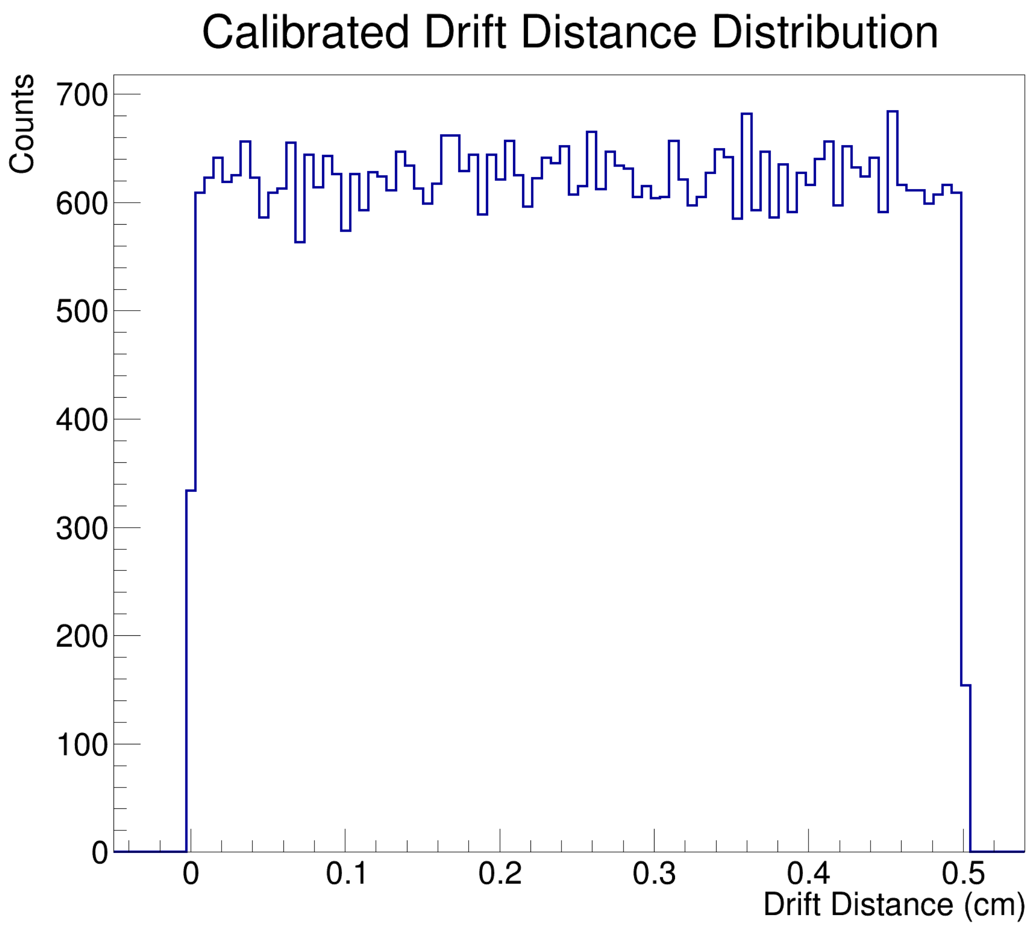

Figure 3.12: Sample drift distance distribution using the t_0 offsets and time-to-distance maps from the calibration. The uniform nature of the distribution is used to verify that the calibration worked as intended.

For several settings, a good drift chamber calibration could not be performed. This occurred primarily due to having insufficient statistics for the particles of interest in those settings. In those instances, the calibration constants from settings with similar kinematics that were run nearby in time were applied instead.

3.3.3 Cherenkov Calibrations

When a charged particle travels faster than the speed of light in a medium, Cherenkov radiation is produced. In the HMS Cherenkov detector described in Sec. 2.4.3, this radiation is focused by one of two mirrors onto a corresponding PMT. Upon reaching the photocathode of a PMT, this radiation then stimulates the emission of a certain number of photoelectrons. Assuming the photocathode is not near being saturated, the number of photoelectrons emitted follows a Poisson distribution, with a mean proportional to the amount of radiation incident on the photocathode. For a single Cherenkov-producing charged particle passing through the HMS Cherenkov detector filled with the gas mixture described in Sec. 2.4.3, the mean sum of the number of photoelectrons emitted across both PMT's photocathodes was found to be approximately 12. These electrons are then multiplied by the PMT, resulting in a large output signal that is sent to an fADC. The fADC then determines the integrated charge present in the signal, measured in units of pC.

The goal of the Cherenkov detector calibration is to produce a mapping for each PMT that allows one to convert from the integrated charge of a signal measured by an fADC, which is not physically meaningful in itself as it is dependent on the gain of the particular PMT, to the number of photoelectrons that were emitted from the corresponding PMT's photocathode, which is physically meaningful as it is directly related to the amount of radiation that was incident on it. These mappings are very important because the sum of the number of photoelectrons emitted from the photocathodes of both PMTs can be used to distinguish between particles that produced Cherenkov radiation in our detector and those that only produced radiation via other processes, as the signal produced in the PMTs due to radiation from these other processes is typically much smaller than the signal produced due to Cherenkov radiation.

Due to the approximately linear relationship between the number of photoelectrons emitted from the photocathode of a PMT and the charge integral of the output signal, the mapping between these two quantities can be accomplished using a con-

PMT #	pC/Photoelectron
PMT 1	10.01
PMT 2	9.46

Table 3.1: Calibration coefficients for the HMS Cherenkov PMTs. The coefficient for each PMT is the factor used to convert from the signal output by the PMT (in pC) to the number of photoelectrons emitted from the photocathode of that PMT.

stant scale factor that is equal to the charge integral corresponding to when a single photoelectron is emitted from that PMT's photocathode. For each PMT, this scale factor is the calibration coefficient we want to obtain. To determine the calibration coefficient for a single PMT, the single photoelectron (SPE) peak in that PMT's charge integral spectrum is fit with the function

$$f(x) = a + bx + cx^2 + de^{-\frac{1}{2}\frac{(x-\mu)^2}{\sigma^2}} , \tag{3.14}$$

where the second-order polynomial is used to model the background, and the mean of the Gaussian μ is the calibration coefficient for that PMT. The conversion can then be made using the equation

$$\frac{\rho_c}{\mu} = n_{pe} , \tag{3.15}$$

where ρ_c is the charge integral and n_{pe} is the number of photoelectrons that were emitted from the photocathode of the PMT. A sample charge integral spectrum with this fit overlayed is shown in Fig. 3.13.

Over the run period, the calibration constants for both of the HMS Cherenkov PMTs were found to be stable enough for our purposes to allow for the use of a single set of coefficients to analyze all of the data, provided in Tab. 3.1.

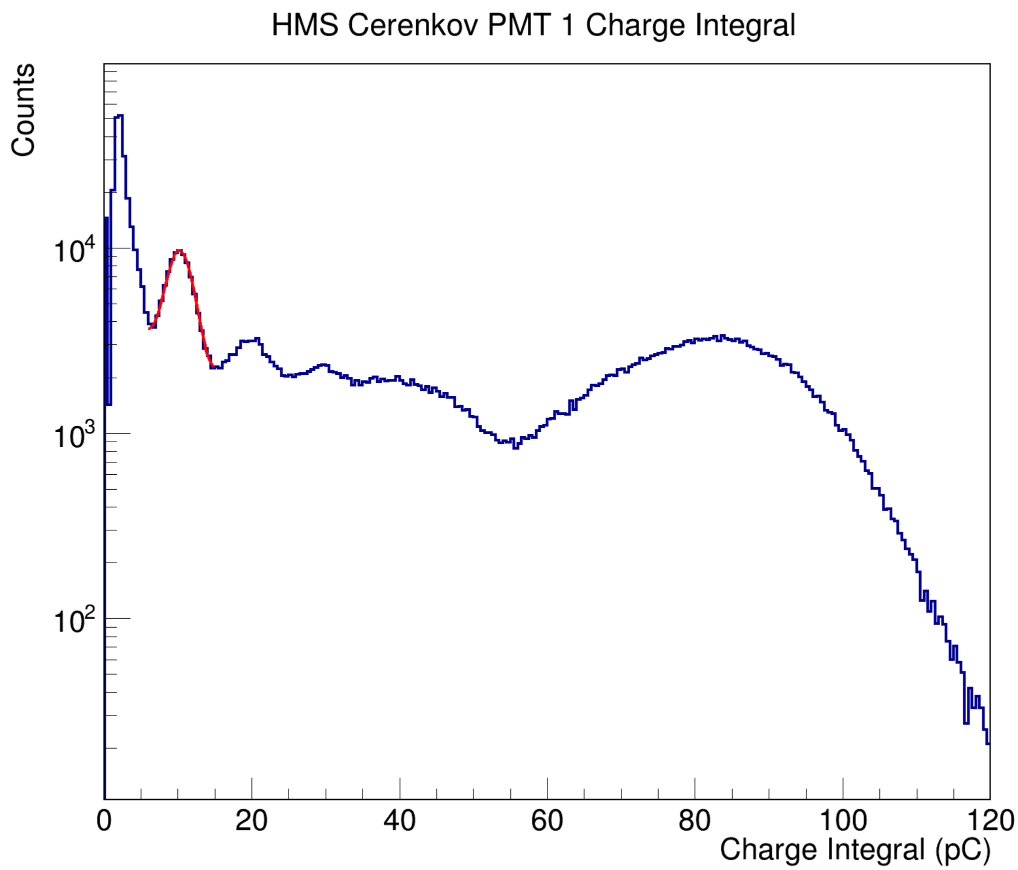

Figure 3.13: Charge integral spectrum for one of the HMS Cherenkov PMTs with a fit of the single photoelectron peak overlayed. The large number of counts to the left of the SPE peak is due to electronic noise. This is also known as the pedestal.

3.3.4 Calorimeter Calibrations

The HMS lead glass calorimeter is primarily used for particle identification, as different types of particles have unique total energy deposition distributions. The goal of the calorimeter calibration is to be able to determine the energy deposited in each of the calorimeter blocks based on the signal amplitudes reported from each of the corresponding fADCs.

In order to determine how much energy was deposited in the calorimeter blocks from the measured signal amplitudes in the corresponding fADCs, one must determine

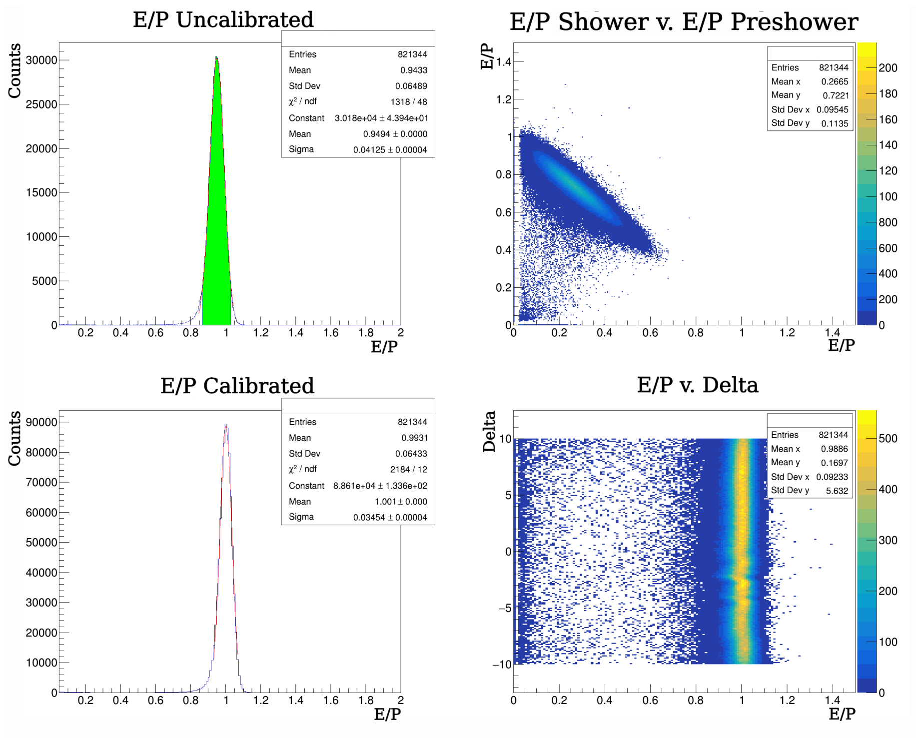

Figure 3.14: Diagnostic plots for the HMS calorimeter calibration. The top left plot shows the calorimeter spectrum before the calibration was performed. The bottom left plot shows the same spectrum using the gains obtained from the calibration script. The bottom right plot shows how the calorimeter spectrum varies as a function of momentum relative to the central momentum. Ideally, there should be no noticeable variation of the E/P peak as a function of δ, however, some slight variation is observed. Fortunately, this variation is small enough that it doesn't have any noticeable impact on the analysis. The top right plot shows the relationship between the energy deposited in the preshower (layers 1 and 2) and shower (layers 3 and 4) blocks.

the gains of each of the PMTs, as well as how much the produced Cherenkov light was attenuated in each of the lead glass blocks before it was picked up by the PMT [63].

The light attenuation is accounted for by multiplying the measured signal amplitude after pedestal subtraction by a correction factor. This correction factor is a function of the track position's distance from the PMTs.

The next step is to determine the relative gains of each of the PMTs. Before the experiment, the gains of the calorimeter's PMTs were set such that the amplitude of the fADC signals would on average be the same between blocks in the same layer. To this end, the gains of the PMTs connected to the bottom blocks were kept relatively low and the gains of the PMTs connected to the top blocks were kept relatively high, counteracting the fact that higher energy particles are bent less by the dipole magnet and are therefore detected lower on the calorimeter. The variation in PMT gains from the top to the bottom of the calorimeter was approximately 20%, corresponding to the total momentum acceptance of the HMS. This amplitude matching was done to ensure that the calorimeter trigger efficiency would be constant over the entire calorimeter.

To correct for the variation in the gains of each of the PMTs, the calibration code minimizes the differences between the estimated total energies deposited by electrons (or positrons) in the calorimeter, and the momenta of these electrons (or positrons) as determined by the tracking. The estimated energy deposited in a PMT is given by

$$\epsilon = c(A - A_{ped})f(y) \ , \tag{3.16}$$

where ϵ is the estimate of the deposited energy, c is the calibration constant for that PMT, A is the amplitude of the signal reported by the fADC, A_{ped} is the pedestal offset of the fADC, and $f(y)$ is the horizontal (y) position-dependent correction to account for the attenuation of light across the lead glass blocks. Calorimeter blocks with PMTs on both sides have a different functional form for the position-dependent correction than blocks with only a single PMT. They are given by:

$$f(y) = \begin{cases} \frac{e^{y/c_1}}{1+\frac{y^2}{c_2}} & \text{if 1 PMT} \\ \\ \frac{c_3 \pm y}{c_3 \pm \frac{y}{c_4}} & \text{if 2 PMTs} \end{cases} \tag{3.17}$$

The calorimeter calibration coefficients were found to not be stable enough to allow us to use a single set of calibration constants to analyze data over the entire run period. This is because the calorimeter PMTs are not optimized for use at high rates, causing their gains to change slightly as the kinematic settings, and consequently the rates, were changed. Therefore, like for the drift chambers, a unique set of calibration constants was used for each kinematic setting. For settings where a good calibration could not be performed due to low statistics, calibration constants from settings with similar kinematics were used.

3.4 BCM Calibrations

To extract cross sections from our experimental data, we must have an accurate measurement of how many electrons impinged on our target in each of our data sets. This measurement relies on an accurate determination of the beam current entering the hall, which is measured using an Unser monitor and several Beam Current Monitors (BCMs) as described in Sec. 2.2.3.

The Unser monitor has a very stable response to changes in beam current (nominally 4 mV/μA), which is calibrated by sending a known current through a wire inside of the beam pipe. However, the Unser monitor has an offset that can drift significantly over time scales of several minutes. This makes the Unser monitor unsuitable for making accurate measurements of the beam current over longer periods of time. On the other hand, the BCMs have very stable offsets, but their gains can drift slightly over the course of several months and also have no a priori absolute calibration. To provide an absolute calibration, special data sets were collected at different times during the experiment to determine the gains of the BCMs relative to the very stable gain of the Unser monitor. Using the gain determined from the cali-

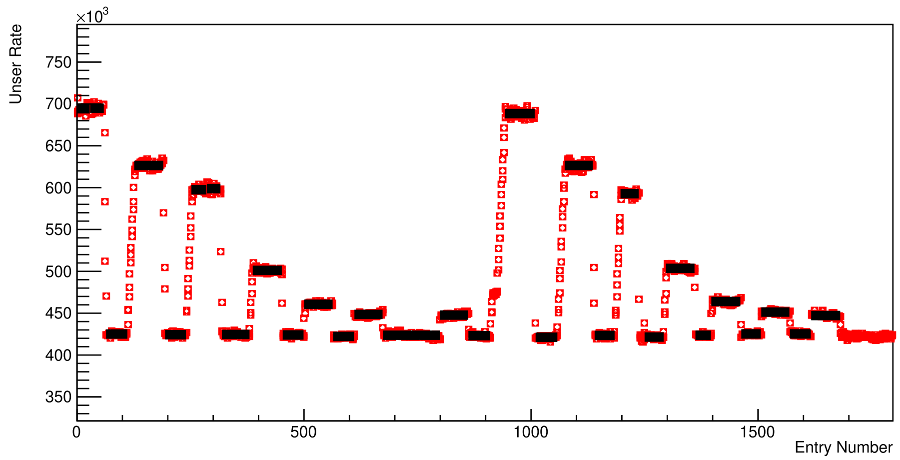

Figure 3.15: Figure from [69]. Unser rates over the course of a single BCM calibration run (one data point every 2 seconds).

bration, the output of a BCM could then be accurately mapped to the corresponding beam current I using the equation

$$I = (\nu_{on} - \nu_{off})A \ , \tag{3.18}$$

where $\nu_{on(off)}$ is the signal from the BCM when the beam is on (off), and A is the BCM's gain. The BCM offset ν_{off} is extrapolated from the calibration, not determined directly from the BCMs when the beam is turned off.

The BCM calibration is performed using a data set where the beam current is frequently turned on and off, as shown in Fig. 3.15. The beam-off periods are used to determine the offset of the Unser monitor, which, as previously mentioned, can drift over timescales of several minutes. With both the offset and gain of the Unser now known, the current entering the hall during the beam-on periods can be accurately measured. The gains and offsets for each of the BCMs can then be extracted by plotting the currents measured by the Unser during the beam-on periods against the

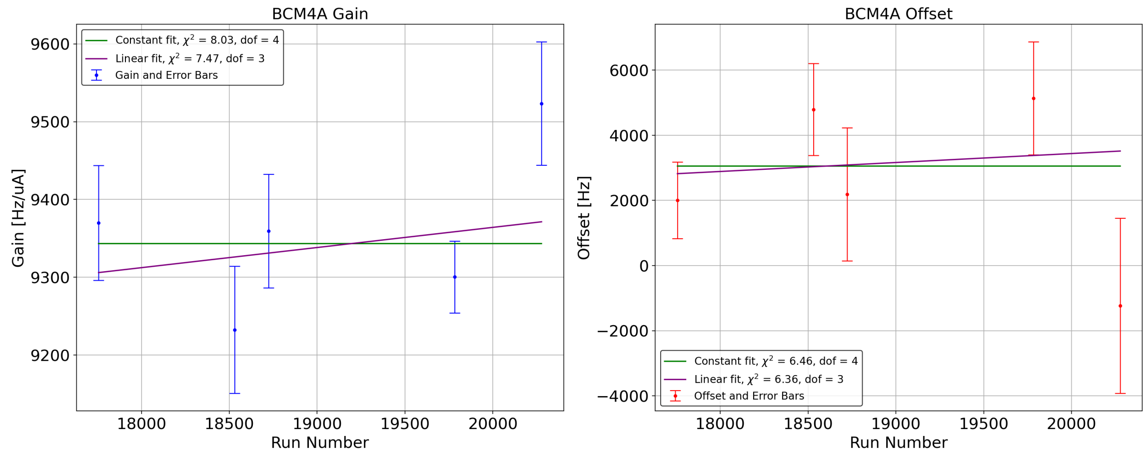

Figure 3.16: Figure from [70]. Measured gains and offsets for BCM4A. Because these quantities were found to be relatively stable and the χ^2/dof was found to be smaller for a constant fit than for a linear fit, the weighted average of each of these quantities was used to determine the beam current for all of the collected data.

corresponding scaler rates and performing a linear fit.

The gains and offsets for BCM1, BCM2, and BCM4A were found to be stable (within measurement uncertainties) throughout the experiment. For each of these BCMs, the weighted averages of the gains and offsets found in the calibrations were used when determining the beam currents measured by that BCM throughout the experiment, as opposed to using multiple different sets of offsets and gains.

In addition to having a stable gain and offset, BCM4A also utilizes a more advanced temperature control system and different electronics, giving it a more linear response over a wider range of beam currents. Therefore, BCM4A was selected to provide the current measurements that were used for the rest of the analysis. The gains and offsets found for BCM4A are shown in Fig. 3.16.

After this calibration, it was found that a small offset persisted in the current measured by BCM4A (as well as the other BCMs). This additional offset, which was determined by looking at the current dependence of yields, is discussed in Sec. 3.9.2.

Quantity	Data Cut	Monte Carlo Cut
Calorimeter Signal	$H.cal.etottracknorm > 0.7$	NA
Cherenkov Signal	$H.cer.npeSum > 2.0$	NA
Non-Dispersive Angle	$\|H.gtr.ph\| < 0.040$ rad	$\|hsyptar\| < 0.040$ rad
Dispersive Angle	$\|H.gtr.th\| < 0.090$ rad	$\|hsxptar\| < 0.090$ rad
Momentum	$\|H.gtr.dp\| < 8.0\%$	$\|delta\| < 8.0\%$
Beam Current	$H.bcm.bcm4a.AvgCurrent > 5.0$ uA	NA
Event Success	NA	$stop\_id == 0$

Table 3.2: Summary of the cuts applied to get a clean electron data set for cross section extraction. The calorimeter signal cut is applied on the momentum-normalized total energy deposition. The Cherenkov signal cut is applied on the sum of the integrals of the signals from the Cherenkov PMTs normalized by the integrals corresponding to the emission of a single photoelectron from the photocathodes of each of the PMTs. The purpose of both the calorimeter and Cherenkov cuts is to remove non-electron events. Acceptance cuts are applied to the reconstructed particle momentum relative to the spectrometer's central momentum (δ), as well as to the particle's reconstructed scattering angle in the dispersive (x) and non-dispersive (y) directions. A cut is applied on the beam current to remove any background events that may have been collected while the beam was turned off. For the Monte Carlo data, a cut is applied on the variable *stop_id* to remove events that failed to enter the spectrometer.

3.5 Cuts and Efficiencies

To measure the inclusive cross section for electron-nucleus scattering, we need to be able to distinguish electron events from events due to other types of particles entering the HMS, primarily pions. This is accomplished by placing cuts on spectra from the HMS calorimeter and Cherenkov detectors. We must also use the tracking information to remove events that did not enter the HMS from within its nominal acceptance, as the Monte Carlo simulation does not reproduce these events well. Finally, a cut is applied to remove any events that occurred while the beam was off, as these are primarily due to cosmic radiation. This section will cover the cuts applied to the experimental data to extract cross sections and their efficiencies. The cuts are summarized in Tab. 3.2.

3.5.1 Calorimeter Cut and Efficiency

As discussed in Sec. 2.4.4, different types of particles have unique total energy deposition distributions in the HMS lead glass calorimeter. A cut is applied on the variable $H.cal.etottracknorm$, the momentum-normalized total energy deposition (E/P) spectrum, to remove most of the pion events while keeping the majority of the electron events. Approximations of the electron and pion momentum-normalized total energy deposition spectra in the calorimeter are shown in Fig. 3.17, where the approximately pure electron and pion data sets are created by applying cuts on the signal from the Cherenkov detector. A calorimeter cut of $E/P > 0.7$ was chosen to strike a balance between minimizing the number of pions that pass the cut and minimizing the number of electrons that fail to pass the cut.

Now that the calorimeter cut has been selected, we must determine the percentage of the good electron events that pass this cut, known as the calorimeter cut efficiency ϵ_{cal}. The ideal data set to determine the calorimeter cut efficiency would use a trigger that did not explicitly depend on the calorimeter signal and would be comprised purely of electrons. The only trigger that was used during E12-10-008 that did not explicitly depend on the calorimeter was the hHODO 3/4 trigger. Unfortunately, all of the data we collected with this trigger had a significant number of pion events relative to the number of electron events, where even very strict Cherenkov cuts would not create a pure enough electron dataset to perform this study.

The hEL_REAL trigger (see Fig. 2.14) explicitly depends on the calorimeter through several pretriggers such as hPreSH_LO, so runs using this trigger cannot be used directly to determine the calorimeter cut efficiency. However, this explicit dependence on calorimeter pretriggers can be accounted for by first determining the hPreSH_LO electron trigger efficiency $\epsilon_{\mathrm{hPR\_LO}}$, which can be accomplished using

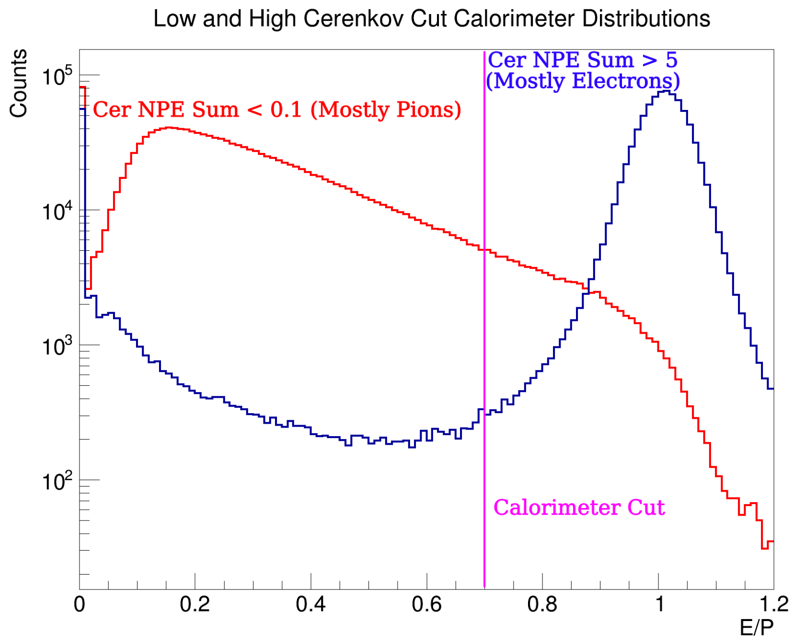

Figure 3.17: Calorimeter momentum-normalized total energy deposition spectra with different cuts on the total Cherenkov signal integral normalized by the integral corresponding to the emission of a single photoelectron from the PMT's photocathode (Cer NPE Sum). Many of the events that pass the Cer NPE Sum > 5 cut but are below the calorimeter cut are pion events that produced signal in the Cherenkov PMTs through other processes. For example, as a pion passes through the material in the spectrometer, it can knock electrons free that produce Cherenkov radiation in the Cherenkov detector.

hHODO 3/4 trigger data. The hPreSH_LO electron trigger efficiency was determined as

$$\epsilon_{\text{PR\_LO}} = \frac{N([\text{PR\_LO}] \wedge H.cer.npeSum > 10.0)}{N(H.cer.npeSum > 10.0)} , \tag{3.19}$$

where the tight PID cut on the signal from the Cherenkov detector was selected to ensure the cleanest electron data set possible while still retaining enough events to prevent the study from losing any sensitivity due to statistical limitations. To account for the small number of pions and other backgrounds that remained in the data sets used to determine the hPreSH_LO electron trigger efficiency after the tight Cherenkov PID cuts were applied, the hPreSH_LO electron trigger efficiency was determined for several targets and fit as a function of the ratio of electron to pion counts for each target, normalized to carbon. The fit was then extrapolated back to the y-axis to determine the electron trigger efficiency. Using this method, the hPreSH_LO electron trigger efficiency was found to be $100.02\% \pm 0.02\%$, therefore, we treated the efficiency of this trigger as consistent with 100% in the analysis.

Now, because the hEL_REAL trigger will fire if the hEL_LO pretrigger fires and the hEL_LO pretrigger can only fire if the hPreSH_LO pretrigger fires, we can determine the calorimeter cut efficiency using hEL_REAL trigger data, which was taken at more favorable kinematic settings for this study than the hHODO 3/4 trigger data, by applying an additional cut requiring the hEL_LO pretrigger to have fired and multiplying the result by the hPreSH_LO efficiency. Therefore, the calorimeter cut efficiency can be determined as

$$\epsilon_{cal} = \epsilon_{\mathrm{PR\_LO}} \frac{N([\mathrm{EL\_LO}] \wedge H.cer.npeSum > 10 \wedge H.cal.etottracknorm > 0.7)}{N([\mathrm{EL\_LO}] \wedge H.cer.npeSum > 10)} \ , \tag{3.20}$$

where the tight PID cut on the Cherenkov signal was used for the same reasons that it was used for in the hPreSH_LO electron trigger efficiency determination. Once again, to account for the small number of pions and other backgrounds that remained in the data used for this study, the calorimeter cut efficiency was determined for several targets and fit as a function of the ratio of electron to pion counts for each target, normalized to carbon, and extrapolated back to the y-axis to determine the electron cut efficiency. The pion sample used to determine the pion fraction (π/e) for each target is obtained by applying the cuts $0.2 < H.cal.etottracknorm < 0.4$ and $H.cer.npeSum < 0.5$. This sample does not include all of the pions, however it is sufficient because we only need to determine the relative pion fractions between different targets. As shown in Fig. 3.18, this fit results in a calorimeter cut efficiency

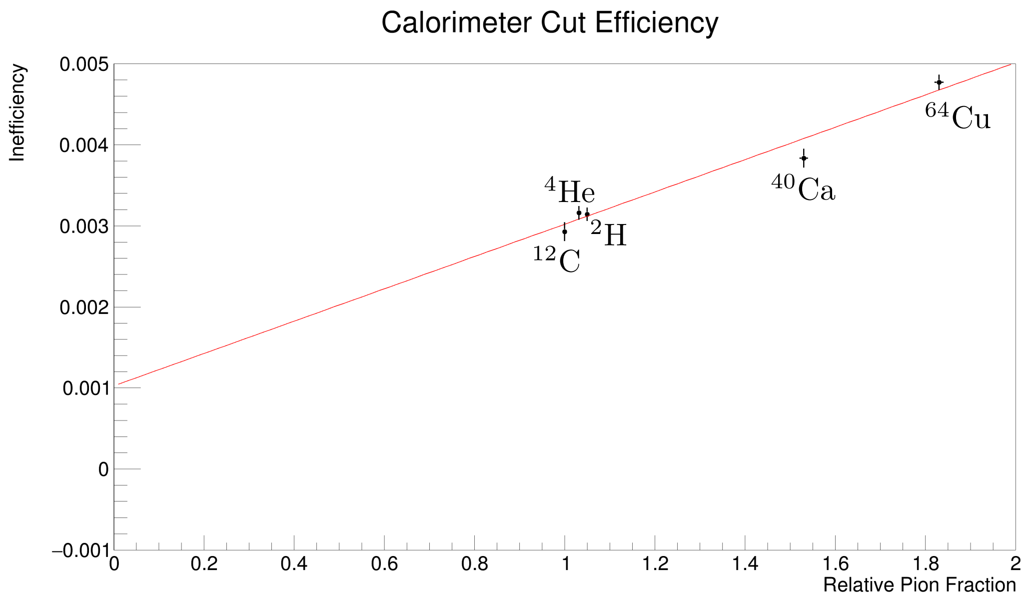

Figure 3.18: Calorimeter cut efficiency for several targets as a function of the ratio of electron to pion counts for each target, normalized to carbon. The fit is extrapolated to the y-axis to determine the cut efficiency for a data set consisting only of electrons.

of 99.9% with a statistical uncertainty of less than 0.1%. Within error, the calorimeter cut efficiency was found to be uniform over the entire surface of the calorimeter.

3.5.2 Cherenkov Cut and Efficiency

To distinguish between particles that did and those that did not produce Cherenkov radiation in the Cherenkov detector, a cut is placed on the total integral of the signals from the Cherenkov PMTs normalized by the integrals corresponding to the emission of a single photoelectron from the photocathodes of the respective PMTs. This quantity is often called the Cherenkov NPE sum and is contained in the variable *H.cer.npeSum*. Non-Cherenkov emitting particles may still produce a signal in the Cherenkov detector PMTs due to radiation emitted in other processes, primarily from “knock-on” electrons. However, the signals produced in the PMTs due to the radiation from these other processes are on average smaller than those produced due

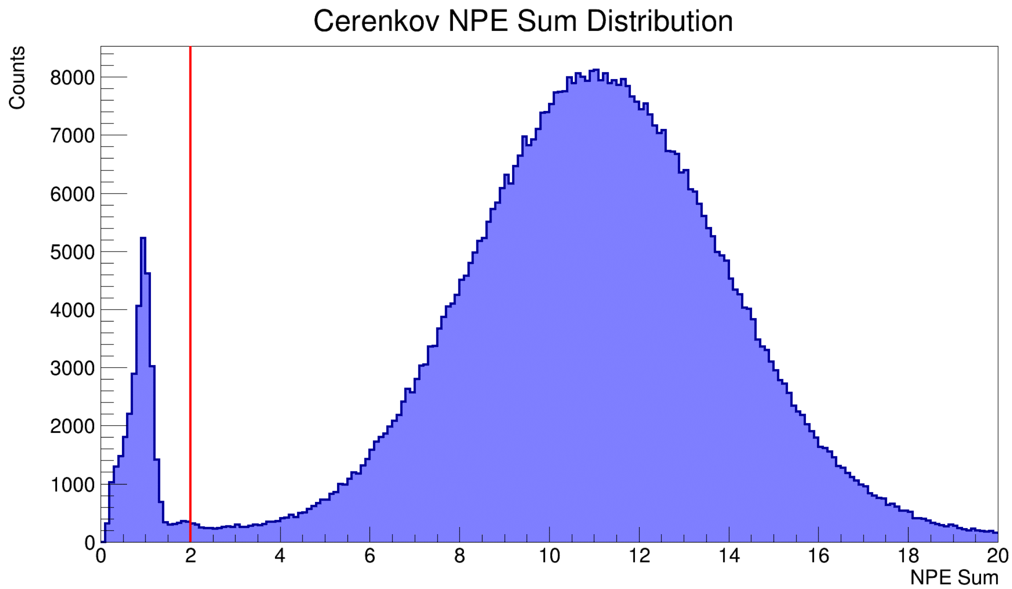

Figure 3.19: Total signal integral from the Cherenkov PMTs normalized by the integral corresponding to the emission of a single photoelectron from the PMT's photocathode. Events that did not produce a signal in the Cherenkov PMTs corresponding to over 0.1 photoelectrons have been filtered from this histogram, removing a large peak at 0. A cut requiring that the NPE sum is greater than 2 is applied in our analysis to remove events that did not produce a significant signal in the PMTs, which mostly occurs for non-Cherenkov-producing particles.

to Cherenkov radiation. As shown in Fig. 3.19, a cut requiring the Cherenkov NPE sum to be greater than 2 removes most of these non-Cherenkov radiation-producing particles.

With the Cherenkov NPE sum cut set, the cut efficiency now needs to be determined. As for the calorimeter cut efficiency, the ideal data set for determining the Cherenkov cut efficiency uses a trigger that does not depend directly on the Cherenkov and consists solely of electrons. While none of the hHODO 3/4 data could be used to produce a clean enough electron sample, some of the hEL_REAL data could. To remove the Cherenkov dependency from the hEL_REAL trigger data, a cut was made requiring the hEL_HI trigger to have fired, which has no Cherenkov dependency. With this data, a tight cut on the calorimeter spectrum was applied to obtain the cleanest electron dataset we could achieve with our data, and the Cherenkov cut was applied to determine its efficiency. Under the assumption that the data set will consist of only electrons after PID cuts, the Cherenkov cut efficiency was determined as

$$\epsilon_{cer} = \frac{N([\mathrm{EL\_HI}] \wedge H.cal.etottracknorm > 1.0 \wedge H.cer.npeSum > 2.0)}{N([\mathrm{EL\_HI}] \wedge E.cal.etottracknorm > 1.0)} \ , \tag{3.21}$$

where the tight PID on the calorimeter signal was used for the same purposes that the tight PID cut on the Cherenkov signal was used in the determination of the calorimeter cut efficiency. Unlike the calorimeter, the Cherenkov cut efficiency was found to vary over the momentum acceptance of the detector as shown in Fig. 3.20. The detector efficiency can be represented by a binomial distribution, where the efficiency is equal to the observed probability of success p of the binomial distribution. The uncertainty of the detector efficiency σ_p in each δ bin is determined by approximating the error of the binomial distribution as a normal distribution, which gives

$$\sigma_p = \sqrt{\frac{p(1-p)}{n}} \ , \tag{3.22}$$

where n is the number of events (trials) in the corresponding δ bin.

This efficiency was fit to a piecewise distribution and corrected for in the analysis. This piecewise function can be written as

$$\epsilon_{cer} = \begin{cases} 0.9994 & \text{if } \delta < -1.0\% \\ 0.99727 - 0.00213 \times \delta & \text{if } -1.0\% < \delta < 0.5\% \\ 0.9962 & \text{if } \delta > 0.5\% \end{cases} \tag{3.23}$$

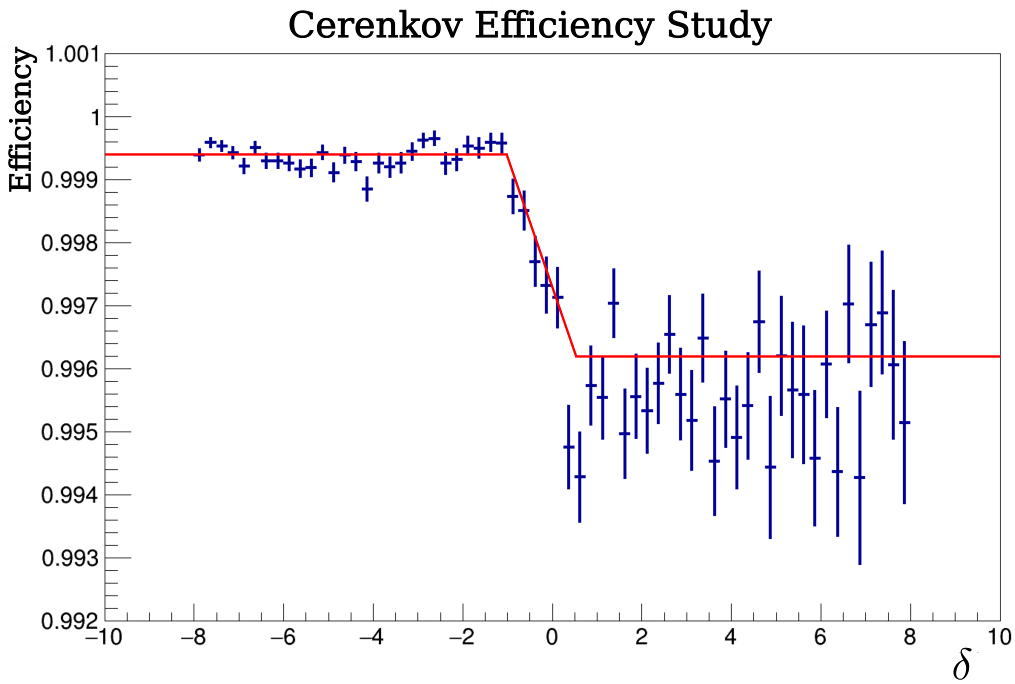

Figure 3.20: Efficiency of the HMS Cherenkov cut as a function of δ, a particle's reconstructed momentum relative to the central momentum of the spectrometer, in percent, for the cryogenic targets. The red line is the fit, given in Eq. 3.21, which is used to correct for the Cherenkov efficiency in the analysis. The dip in efficiency around $\delta = 0$ is hypothesized to be due to differences between the top and bottom mirrors or PMTs of the Cherenkov detector. At high δ, the efficiencies were found to vary by about $\pm 0.1\%$ between different targets. The discrepancy between the fit and the data points at high δ is because the fit was determined using the carbon target efficiency, which had relatively low backgrounds compared to other targets.

where δ is the reconstructed momentum of the particle relative to the central momentum of the spectrometer, given in percent. A 0.1% point-to-point systematic uncertainty was applied for the trigger and detector cut efficiency corrections to account for uncertainty in the methods used to extract the efficiencies and to account for small variations in the Cherenkov cut efficiency observed across different targets. This systematic uncertainty is small compared to our target statistical uncertainty of 0.5%, which is based on bins of size 0.025 in x_{Bj}.

3.5.3 Acceptance Cuts

Comparisons are made between the experimental data and Monte Carlo simulations to extract cross sections. The Monte Carlo simulation can reproduce the experimental results very well within a certain momentum and angular acceptance of the spectrometer. However, outside of this acceptance, the Monte Carlo does not reproduce the real-world data well. To limit the data to Monte Carlo comparison to the kinematic region where the Monte Carlo *can* reproduce the experimental results well, cuts are applied to the reconstructed dispersive angle, non-dispersive angle, and momentum (relative to the spectrometer's central momentum) in both the experimental and Monte Carlo data. The exact acceptance cuts used are provided in Tab. 3.2.

3.5.4 Beam Current Cut

A cut is applied to ensure that the beam current measured by BCM4A was above 5 μA at the time the event occurred. This cut is used to remove unwanted events that happened while the beam was off, as these events are primarily caused by cosmic radiation. This cut also eliminates events that occurred at the beginning of ramping up the beam current into the hall, when the beam may not yet be stable. Additionally, this cut removes any false beam current that the BCM might register due to a small offset or noise in its output while the beam is off, ensuring a more accurate accounting of the beam charge accumulated during a run.

3.6 Electron Tracking Efficiency

Occasionally, the tracking algorithm may fail to reconstruct a track for an electron event passing through our detector. This can occur due to inefficiencies in the drift chamber planes, which can cause not enough planes to have wires that fired to enable left-right ambiguities to be resolved and for a good track to be reconstructed. The tracking algorithm may also fail if too many wires in each of the individual planes fire in an event, making it difficult to unambiguously determine a single good track to associate with that event.

The equation for the electron tracking efficiency of our detector can be written as

$$\epsilon_{track}^{e^-} = \frac{N_{el\_did}}{N_{el\_should}} , \tag{3.24}$$

where N_{el_should} is the number of events that passed electron PID cuts and passed through a fiducial region defined by the hodoscope planes, and N_{el_did} is the number of those events for which a good track was also found. As shown in Fig. 3.21, the electron tracking efficiency was calculated to be over 98% for all of the data collected during E12-10-008 and was generally above 99.6%.

To extract cross sections, these tracking efficiencies were applied as corrections to the data on a run-by-run basis to account for the otherwise good electron events that were not counted due to them not having tracks. The uncertainty of the electron tracking efficiency was determined by filling an inverse-variance weighted histogram with the residuals of the H1X rate-dependent linear fit shown in Fig. 3.21 and calculating the standard deviation of the distribution, which was found to be approximately 0.04%.

3.7 Dead Time Corrections

There are two types of dead times that must be corrected for when extracting experimental cross sections: computer dead time and electronic dead time. Both of

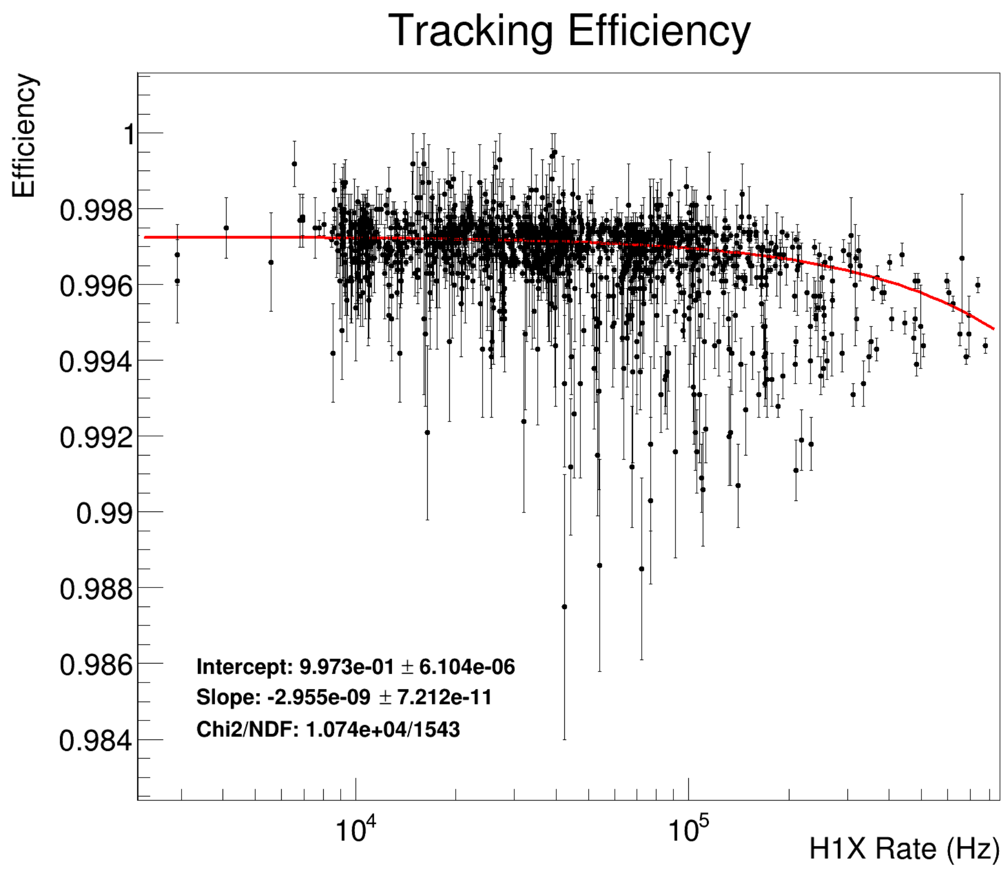

Figure 3.21: Electron tracking efficiency of each of the data sets collected during E12-10-008. The efficiency is plotted against the rate of hits in the first hodoscope plane (H1X) to determine the rate dependence of the tracking efficiency. A first-order polynomial, shown in red, is fit to the tracking efficiency, and the standard deviation of the residuals of this fit is used to determine the uncertainty of the tracking efficiency.

these dead times can be corrected for together using a value known as the "total live time", t_{tlt}, which is defined as the effective fraction of time during which events were able to be counted by our detector *and* data acquisition system. As the computer and electronic dead times are independent, the total live time can be written as their product

$$t_{tlt} = t_{elt} \times t_{clt} \ , \tag{3.25}$$

where t_{elt} is the electronic live time and t_{clt} is the computer live time. These correction factors correspond to the fractions of events that are not lost due to each of these dead times. In this section, we define electronic and computer dead times and outline how their correction factors are determined.

3.7.1 Computer Dead Time

Events may be dropped if the DAQ is unable to write data to disk quickly enough to keep up with the incoming event rate. These dropped events are said to be lost due to computer dead time. Fortunately, the scaler data makes determining how many events were lost this way a simple process.

When a selected pre-trigger fires, it causes the DAQ to write an event to disk, though, as previously mentioned, the event may be dropped if the data cannot be written quickly enough. In addition, a copy of that pre-trigger's output pulse is sent to the scaler DAQ, which counts how many times that pre-trigger fires. By taking the ratio between the number of events written to disk N_{disk} and the corresponding scaler DAQ count for that pre-trigger N_{scaler}, one can determine the computer dead time correction factor (or effective computer live time) t_{clt} as

$$t_{clt} = \frac{N_{Disk}}{N_{Scaler}} \ . \tag{3.26}$$

The computer dead time correction factors calculated for runs taken during the E12-10-008 experiment are shown in Fig 3.22. The computer dead time was corrected for on a run-by-run basis. If more than one event type (hHODO 3/4, hEL_REAL, hEL_CLEAN) is collected at a single time, applying the computer dead time correction can get complicated, however, because we only took one event type at a time, this correction can be applied in a straightforward manner.

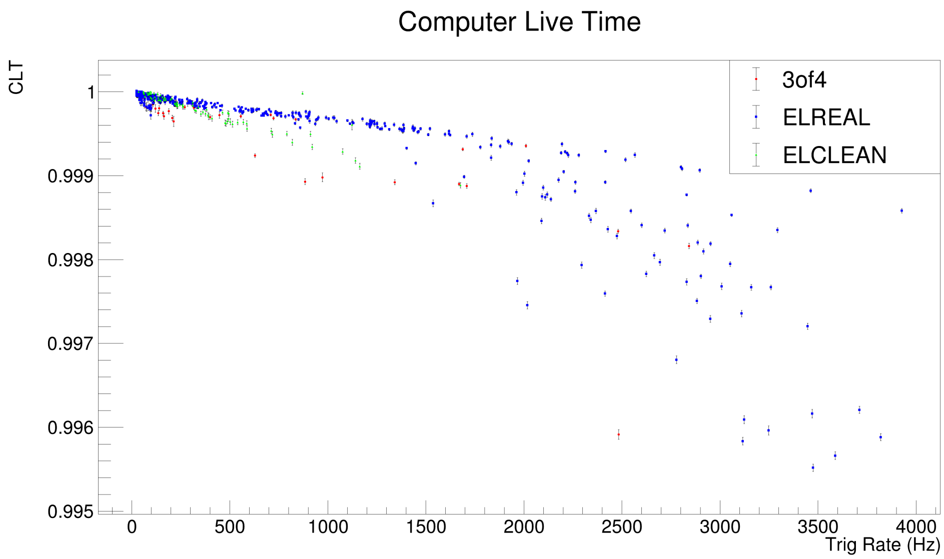

Figure 3.22: HMS computer dead time correction factors (effective computer live times) as a function of prescaled trigger rate for runs taken during E12-10-008. The fraction of events lost due to the computer dead time was found to be generally on the order of 0.1% for most runs, representing a relatively small correction – especially at low (<1 kHz) trigger rates.

3.7.2 Electronic Dead Time

When an event in the HMS meets the conditions of a pre-trigger, that pre-trigger will generally fire, outputting a logic pulse. However, for a duration τ after a pre-trigger fires, any additional events that reach that pre-trigger will be ignored and not be counted, illustrated in Fig. 3.23. The events lost this way are said to be lost due to electronic dead time. To extract experimental cross sections, we must account for the events which were not counted due to this dead time.

A particle entering the spectrometer can be considered an independent, discrete event. Therefore, the probability distribution of n, the number of good events that are sent to the trigger over a fixed period of time τ, will follow a Poisson distribution, written as

$$P(n) = \frac{(R_{true}\tau)^n e^{-R\tau}}{n!} \ , \tag{3.27}$$

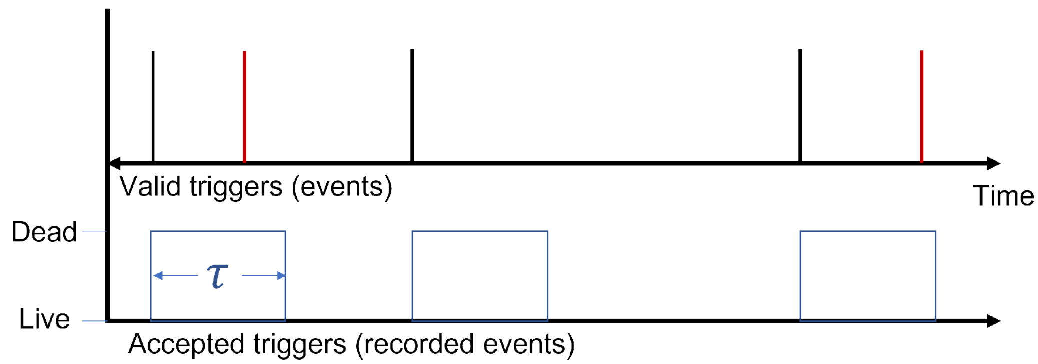

Figure 3.23: Figure from [71]. Illustration showing how electronic dead time can cause events to be dropped. The events shown in red are dropped because they arrived within the dead time of a previous event.

where R_{true} is the average event rate. To correct for the electronic dead time, we must determine the fraction of events that caused the pre-trigger to fire and were not lost due to the electronic dead time, t_{elt}.

t_{elt} can be expressed as the ratio of R_{meas} over R_{true}, where R_{meas} is the measured rate of accepted triggers as determined from the scalers, however, we have no direct way to determine R_{true}. Rather, we infer the electronic dead time from measuring the total dead time and removing the contribution from computer dead time. To measure the total dead time, a system known as the Electronic Dead Time Monitor (EDTM) is used. This system injects a pulse of a known frequency into the trigger electronics, with a copy of the EDTM pulse being passed directly to the scaler DAQ to get a count of how many EDTM pulses were sent to the trigger electronics. Like the events coming from the detector, these pulses can be dropped due to both electronic and computer dead times. Therefore, the fraction of output EDTM pulses (as measured by the scalers) that caused the trigger to fire and were written to disk as events, is equivalent to the total dead time correction factor, t_{tlt}, which can be written as

$$t_{tlt}^{raw} = \frac{N_{EDTMDisk}}{N_{EDTMScaler}} \ . \tag{3.28}$$

However, we need to account for the EDTM pulses that arrived during beam downtimes, as we are only interested in the electronic dead time correction factor as it applies to physics events, which only occur when the beam is being sent into the hall. Assuming fast beam ramp-up and ramp-down times, the effective total dead time correction for physics events can be written as

$$t_{tlt} = \frac{t_{tlt}^{raw} - (1-f)}{f} \ , \tag{3.29}$$

where f is defined as the average beam current including beam downtimes divided by the average beam current not including beam downtimes. This correction factor can then be used along with the computer dead time correction factor to determine the electronic dead time correction factor using Eq. 3.25. A plot of the total dead time correction factors calculated for runs taken during the E12-10-008 experiment is shown in Fig 3.24. It was found that the total dead time determined using the EDTM was smaller than the corresponding computer dead time. This should not be possible because the total dead time includes the computer dead time, therefore the total dead time should be greater than or equal to the computer dead time. This observation indicates that there is an issue with how the EDTMs are counted. It was found that this issue is due to random coincidences causing non-EDTM events to be misidentified as EDTM events, which in turn causes the calculated total and electronic dead time correction factors to be unreliable, especially for runs with higher trigger rates. However, the data can be used to constrain the electronic dead time correction factor to less than 0.1% for most kinematic settings using the data from hEL_CLEAN runs, which have lower trigger rates. More reliable total and electronic dead time corrections can be extracted in the future with further analysis and more strict timing cuts. For now, the total dead time correction can be well approximated

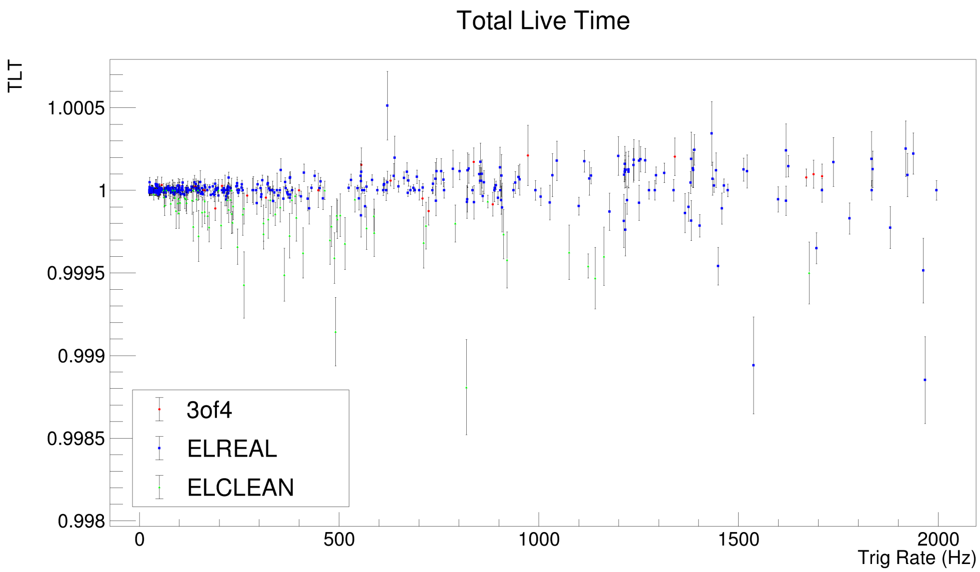

Figure 3.24: HMS total dead time correction factors as a function of prescaled trigger rate for runs taken during E12-10-008. The total dead time correction factors were generally greater than or equal to the corresponding computer dead time correction factors alone. We believe this to be due to random coincidences causing non-EDTM events that were written to disk to be misidentified as EDTM events.

by the computer dead time correction and a conservative 0.1% uncertainty to account for the effects of the electronic dead time.

Once reliable electronic dead time correction factors can be determined, we would like to calculate the electronic dead time τ from our determination of the electronic live time. The electronic dead time is taken to be (approximately) non-extendable (non-paralyzable), meaning that the dead time after an accepted trigger is a fixed value that is not extended if an additional event arrives during the dead time. With this, the fraction of time during which an event could not be recorded is given by $R_{meas}\tau$. Therefore, the fraction of time during which an event could be recorded is $1 - R_{meas}\tau$. With this information, t_{elt} can be written as

$$t_{elt} \equiv \frac{R_{meas}}{R_{true}} = \frac{1 - R_{meas}\tau}{1} = \frac{1}{1 + R_{true}\tau} \ . \tag{3.30}$$

Therefore, the electronic dead time τ for a pre-trigger can be determined by fitting the electronic dead time correction t_{elt} as a function of the measured rate of the pre-trigger output.

3.8 Spectrometer Momentum Offset

The central momentum of the HMS was determined from the magnet settings throughout the experiment and a value for the central momentum was recorded for each run. However, due to various factors, the measured central momenta may be offset from the true central momenta of the spectrometer.

We can leverage $e - p$ elastic scattering measurements from our ^{1}H target to accurately determine the HMS's central momentum offset, as the momentum of an electron that is elastically scattered from a stationary proton is fully constrained by the electron's initial momentum and deflection angle. The invariant mass of a scattering reaction, defined in terms of electron observables in Eq. 1.2, is equal to the proton mass for electrons elastically scattered from a proton. Therefore, if we set the kinematic acceptance of our spectrometer so that it covers the region of kinematic space where we expect to observe elastically scattered electrons, we would expect to see a peak in the invariant mass spectrum located near the proton mass, with some offset and variance due to radiative effects, ionization energy loss, and the finite resolution of the spectrometer. The effects that shift and widen the nominal invariant mass peak expected from elastically scattered electrons are well modeled in *SIMC*, one of the Hall C Monte Carlo programs [72].

To determine the central momentum offset of the HMS using simulated and measured invariant mass spectra at elastic kinematics, first, the elastic peaks for both the measured and simulated data sets are fit to Gaussian distributions. Next, the

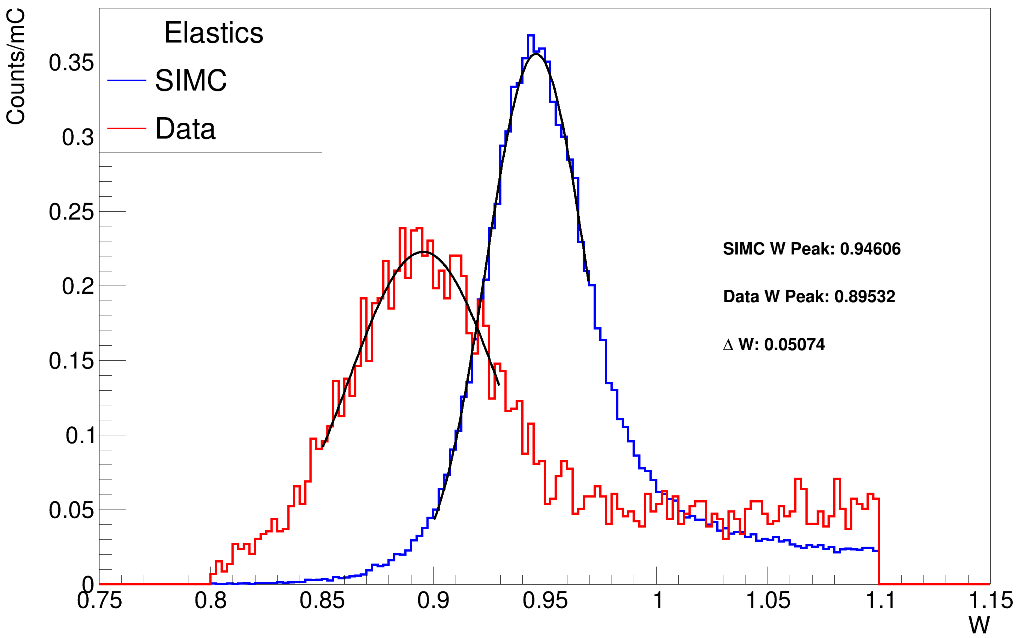

Figure 3.25: Measured and simulated invariant mass spectra at elastic kinematics without a spectrometer central momentum offset correction applied to the measured data. The elastic peak from SIMC is not equal to the proton mass due to ionization energy losses and radiative effects, which are discussed further in Sec. 3.14.1.

difference between the means of the two distributions, ΔW, is calculated. A plot of the uncorrected measured and simulated invariant mass spectra is shown in Fig. 3.25.

One can then use Eq. 1.2 to determine the spectrometer central momentum offset that needs to be applied to the data to reproduce the simulated invariant mass peak. Reanalyzing the measured data using the corrected spectrometer central momentum, we find that the locations of the measured and simulated elastic peaks now agree, shown in Fig. 3.26.

By varying the HMS scattering angle, elastic data were collected over the majority of the range of HMS central momentum settings that were used to collect DIS data at 20°. The kinematic settings used to collect elastic data are given in Tab. 3.3.

The E' offset was determined for all of the elastic kinematic settings, and the ratio between the nominal central momentum measured during data taking (P_{nom})

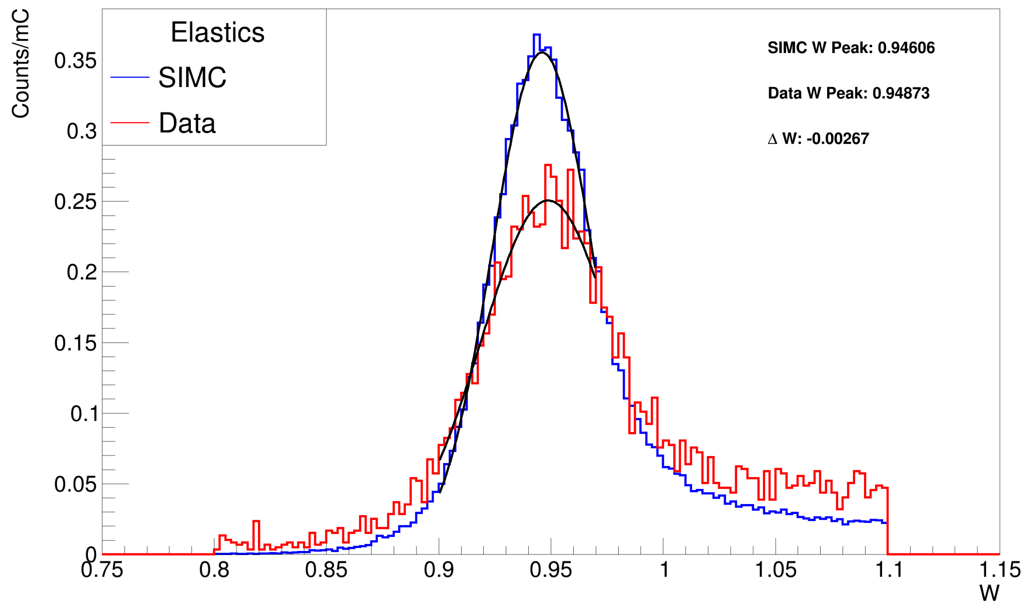

Figure 3.26: Measured and simulated invariant mass spectra at elastic kinematics with a spectrometer central momentum offset correction applied to the measured data.

and the central momentum determined from elastic scattering data (P_{true}) was fit as a function of the nominal central momentum with

$$\frac{P_{true}}{P_{nom}} = p_0 - p_1 e^{-0.5\left(\frac{x-p_2}{p_3}\right)^2}, \tag{3.31}$$

as shown in Fig. 3.27. This function was then used to determine the correct spectrometer central momentum when analyzing experimental data and generating simulated

Beam Energy (GeV)	HMS Angle (Degrees)	HMS Central Momentum (GeV)
10.544	39.08	-3.00
10.544	34.30	-3.57
10.544	30.05	-4.20
10.544	26.415	-4.78
10.544	23.61	-5.36
10.544	21.36	-5.878

Table 3.3: Kinematic settings used to collect elastic data with the HMS.

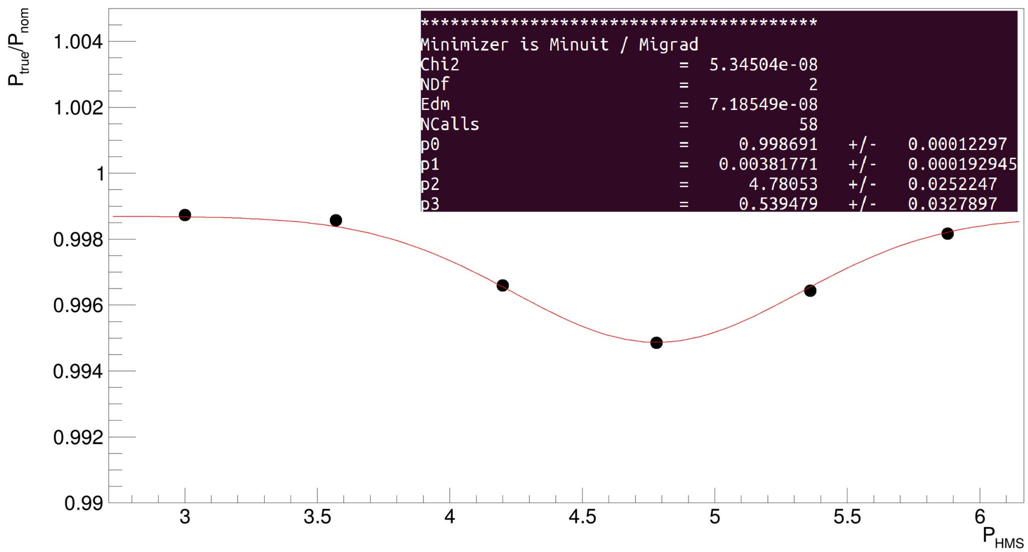

Figure 3.27: HMS central momentum offset as a function of the nominal central momentum set during data taking. A fit consisting of a uniform offset and a Gaussian distribution was found to match the data well. The momentum offset was found to increase up to an HMS central momentum of about 4.8 GeV, where the offset then decreases. The increase of the offset up to around 4.8 GeV is due to the saturation of the HMS magnets, which gets worse as the HMS central momentum setting increases. Above 5 GeV, the offset decreases because the code used to set the HMS magnets is configured to correct for the saturation effects at these higher momentum settings.

data. The drift chamber resolution was also determined using elastic data by adjusting the drift chamber resolution in the simulation until the widths of the measured and simulated elastic peaks matched. The drift chamber resolution was found to vary with the spectrometer's cental momentum. The variation was modeled by a fit to data which yielded the function

$$\sigma_{dcr} = 0.094 \cdot e^{-0.730 \cdot E'} + 0.045 \;, \tag{3.32}$$

where σ_{dcr} is the drift chamber resolution in centimeters. This function was then used to determine the drift chamber resolution for the HMS simulated data.

3.9 Cryogenic Target Corrections

In this section, we describe the corrections related to the cryogenic targets. These include correcting for the effects of the target cell wall, the contraction of the target cell at low temperatures, and density loss of the cryogenic target due to the energy deposited by the electron beam.

3.9.1 Cell Wall and Cell Contraction Corrections

The nominal lengths of the cryogenic target cells are measured from their exteriors at room temperature (~ 293 K). When these aluminum alloy cells are cooled from room temperature to 20 K, they contract. Using existing data on the thermal properties of aluminum, it is found that this temperature change causes the length of the cell to be reduced by approximately 0.4% [73]. In addition, the cell walls have finite thicknesses, which are provided in Tab. 2.6. Because the length of the cell is measured from the exterior of the cell walls, the thicknesses of the front and back walls of the cell must be subtracted from the measured length of the cell to determine the length of the cryogenic material inside the cell.

To account for events that were scattered from the walls of the cryogenic target rather than the target itself, we use the "dummy" target that was discussed in Sec. 2.6. First, for a given kinematic setting, the charge normalized yield of the dummy target is determined. This yield is broken into upstream and downstream dummy foil yields. These yields are then scaled by the relative thicknesses between the dummy foils and the corresponding cell walls and subtracted from the cryogenic target data, shown in Fig. 3.28. With the yield due to the cell walls now accounted for, only the yield from the cryogen itself remains.

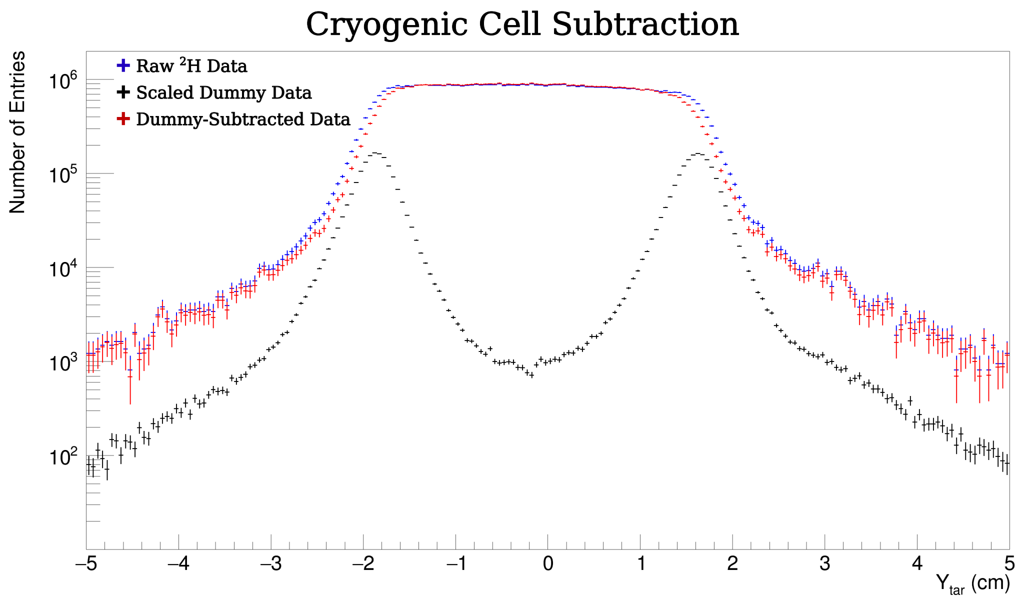

Figure 3.28: Cryogenic target yields before and after dummy subtraction along with the scaled dummy target yield. The dummy-subtracted data also includes the density fluctuation correction, discussed in the next section.

3.9.2 Density Loss Correction

As the electron beam passes through a cryogenic target, the deposited energy causes the cryogen to heat up and its density to decrease. The density of the target must be known to extract cross sections; therefore, to account for density loss due to heating from the electron beam in the analysis, dedicated data sets were taken on the cryogenic targets to measure the changes in the yield as a function of beam current to infer the change in target density.

Measurements were also made on the carbon target at the same beam currents to serve as the control data set. Since the thickness of the carbon target should not change appreciably due to heating from the electron beam, the dedicated carbon data allows for the identification and removal of any current-dependent changes to the target yields that are not due to changes in the target density. As shown in Fig. 3.29, the yield from the carbon target unexpectedly appears to decrease as the

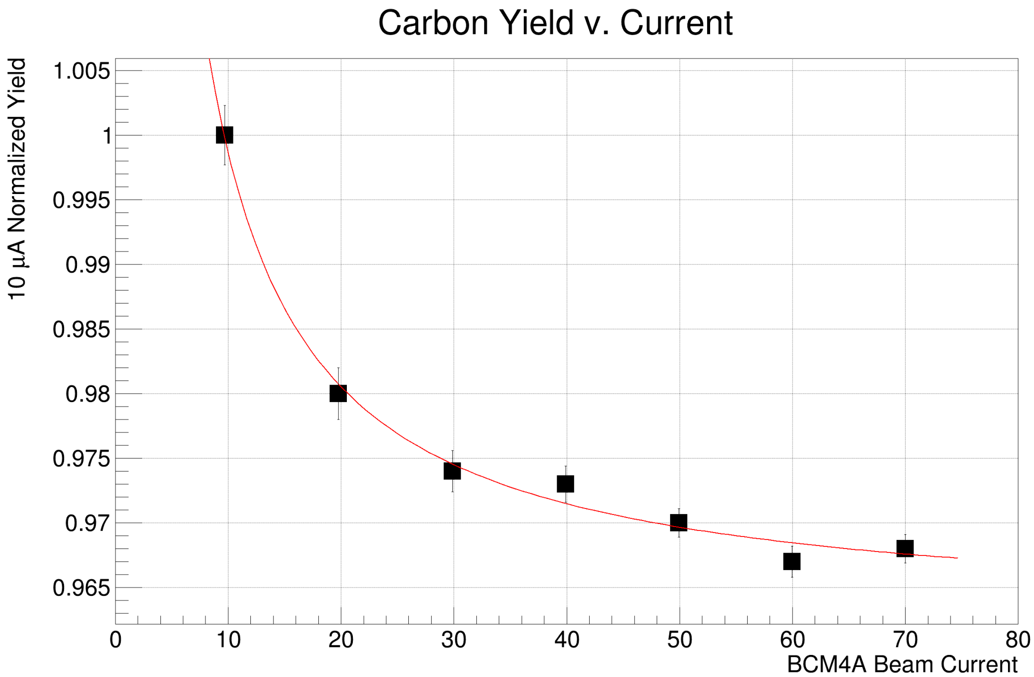

Figure 3.29: Charge normalized yield of the carbon target plotted as a function of the beam current. The yield appears to decrease as the beam current increases. Because the density of the carbon target should not significantly change due to heating from the beam, this effect can be explained by a 0.37 ± 0.03 μA beam current offset that persisted after the BCM calibration.

beam current increases.

This can be explained by a small beam current offset that persisted after the BCM calibration, discussed in Sec. 3.4. First, the definition of the measured electron yield can be written as

$$Y_{meas} = \frac{N}{Q_{meas}} = \frac{N}{I_{meas}\Delta t} \ , \tag{3.33}$$

where N is the number of detected electrons (corrected for efficiencies), Q_{meas} is the total accumulated charge as determined by a BCM, I_{meas} is the average measured beam current for the collected data, and Δt is the duration over which the data was collected. If there is a small offset ΔI in the beam current measured by the BCM such that $I_{true} = I_{meas} + \Delta I$, the true electron yield can be written as

$$Y_{true} = \frac{N}{Q_{true}} = \frac{N}{I_{true}\Delta t} = \frac{N}{(I_{meas} + \Delta I)\Delta t} \ . \tag{3.34}$$

Therefore, we can relate the measured and true electron yields as

$$Y_{meas} = Y_{true}(1 + \Delta I/I_{meas}) \ , \tag{3.35}$$

and fit the measured yields as a function of the measured beam current to determine the offset in the measured beam current. As shown in Fig. 3.29, this fit does a good job of describing the carbon data. The beam current offset for BCM4A extracted from this fit is 0.37 ± 0.03 μA. This offset is slightly larger than expected from the uncertainties in the analysis presented in Sec. 3.4. This relatively large offset may indicate that there is a systematic issue with how the BCMs are calibrated that causes such an offset to persist even after calibration.

With the BCM offset from the carbon data in hand, we can now determine how the yields of each of the cryogenic targets change as a function of the corrected beam current. In Fig. 3.30, normalized yield data for each of the targets used in this study is shown as a function of the corrected beam current, and the data for each of the cryogenic targets is fit to a first-order polynomial. Normalized yields and fits of both dummy-subtracted and non-dummy-subtracted data are shown for reference, however, only the former are used in the analysis, as the fractions of events that originate from the aluminum cell of the cryogenic targets vary across different kinematics.

A linear fit was found to model the data well for all cryogenic targets except ^{1}H, the density of which is not needed for the analysis presented here. These fits were then normalized to make the y-intercept equal to unity, as the density of a target

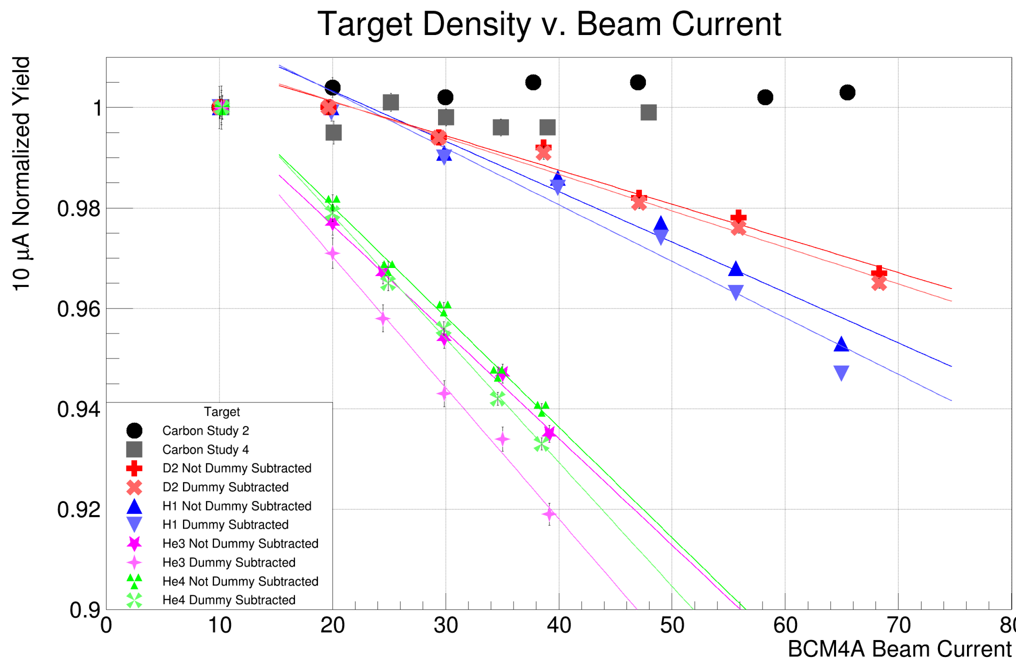

Figure 3.30: Relative yields with statistical error bars for the cryogenic and carbon targets, plotted as a function of the beam current. The two sets of data on the carbon target, labeled Carbon 2 and Carbon 4, are shown to verify the stability of the BCM offset over time. In addition, dummy-subtracted and non-dummy-subtracted data are shown for each of the cryogenic targets, as the density correction can be performed using either data set. A linear fit models the data well for all targets except for ^{1}H. None of the fits include the 10μA data point, as it is the most sensitive to any remaining offset in the measured BCM current. The slopes of these fits, normalized to make the y-intercept equal to 1, are provided in Tab. 3.4.

should be equal to its nominal value when the beam is turned off. The slopes of the normalized fits, measured in percent change in yield per 100 μA, are provided in Tab. 3.4.

The purpose of the density loss correction is to remove the impact the beam current has on the measured yields by scaling them to the value they would be if the beam current did not change the local density of the target along its path. This correction is applied on a run-by-run basis as a function of the time-averaged and offset-corrected beam current I_{avg} throughout the run, where the time averaging only

Target	Dummy-Sub. Slope (-%/100 μA)	Non-Sub. Slope (-%/100 μA)
^{1}H	10.98 ± 0.39	9.81 ± 0.34
^{2}H	7.17 ± 0.27	6.72 ± 0.25
^{3}He	25.55 ± 1.63	20.84 ± 1.28
^{4}He	24.00 ± 0.95	21.46 ± 0.85

Table 3.4: Slopes of the normalized fits to the dummy-subtracted and non-dummy-subtracted yields of the cryogenic targets as a function of beam current. These linear fits modeled the data well for all cryogenic targets except for ^{1}H.

includes times when the beam current was above 5 μA. For a given target, the density loss correction be can calculated as

$$C_{dens} = 1 - mI_{avg} \ , \tag{3.36}$$

where m is the slope of the normalized fit to the dummy-subtracted yields for that target. This correction is applied by dividing the measured yield by C_{dens}.

Analysis showed that the magnitude of the density loss varied along the length of the target. This may introduce effects that cannot be modeled by simply scaling the yield for a run by a single number. However, the impact of this variation on the momentum distribution of particles entering the spectrometer was found to be consistent with zero, therefore, the correction defined in Eq. 3.36 is sufficient.

3.10 Reconstructed Momentum Correction

The momentum of a particle that enters the spectrometer is calculated using the tracking and optics information. Looking at the ratio of the measured and Monte Carlo yields, a small dependence on δ, the particle momentum relative to the central momentum, was noticed. The same dependence was found for different targets and kinematic settings, shown in Fig. 3.31.

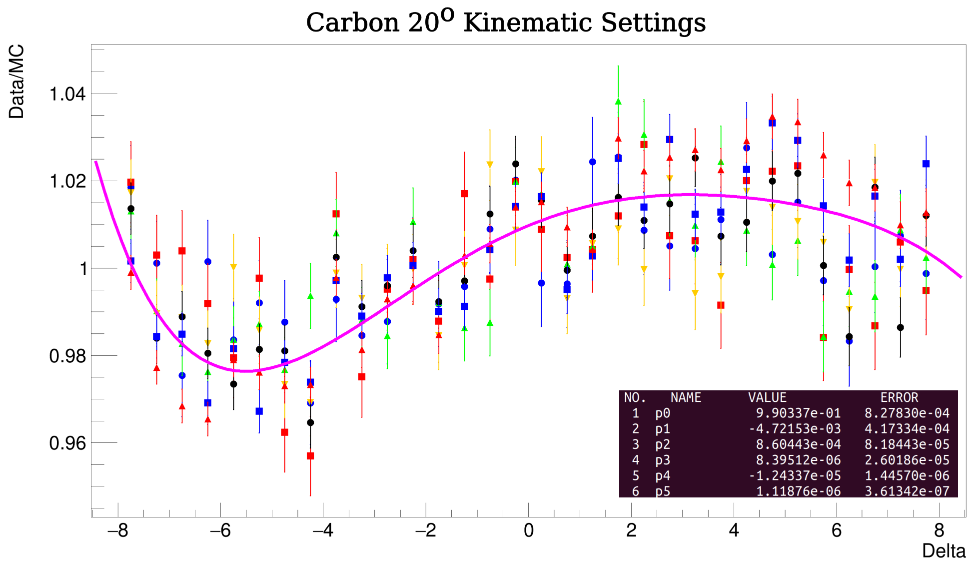

Figure 3.31: Data to Monte Carlo ratio binned in delta for the different 20° kinematic settings. The ratios are fit to the inverse of a fifth-order polynomial $f(\delta_{true})$to extract offsets in the momentum reconstruction.

This δ dependence has been observed since the first experiments using the HMS spectrometer [74]. While the precise cause has not been determined, this effect is likely due to small imperfections in the calibration of the momentum reconstruction. This causes the experimentally measured δ to be different than the true value used by the Monte Carlo. Instead, the measured δ is taken to be some function of the true δ from the Monte Carlo, $\delta_{exp} = g(\delta_{true})$.

To determine $g(\delta_{true})$, first, the data to Monte Carlo yield ratio, with each dataset binned as a function of its respective δ, was fit with an inverse fifth-order polynomial $f(\delta)$. This function was chosen as it fits the data well with relatively few parameters. With this fit function, the measured value of δ can be written in terms of the true Monte Carlo value as

$$\delta_{exp} = g(\delta_{true}) = \int \frac{1}{f(\delta)} d\delta \ . \tag{3.37}$$

With this equation, one can also determine the offset between the true and measured

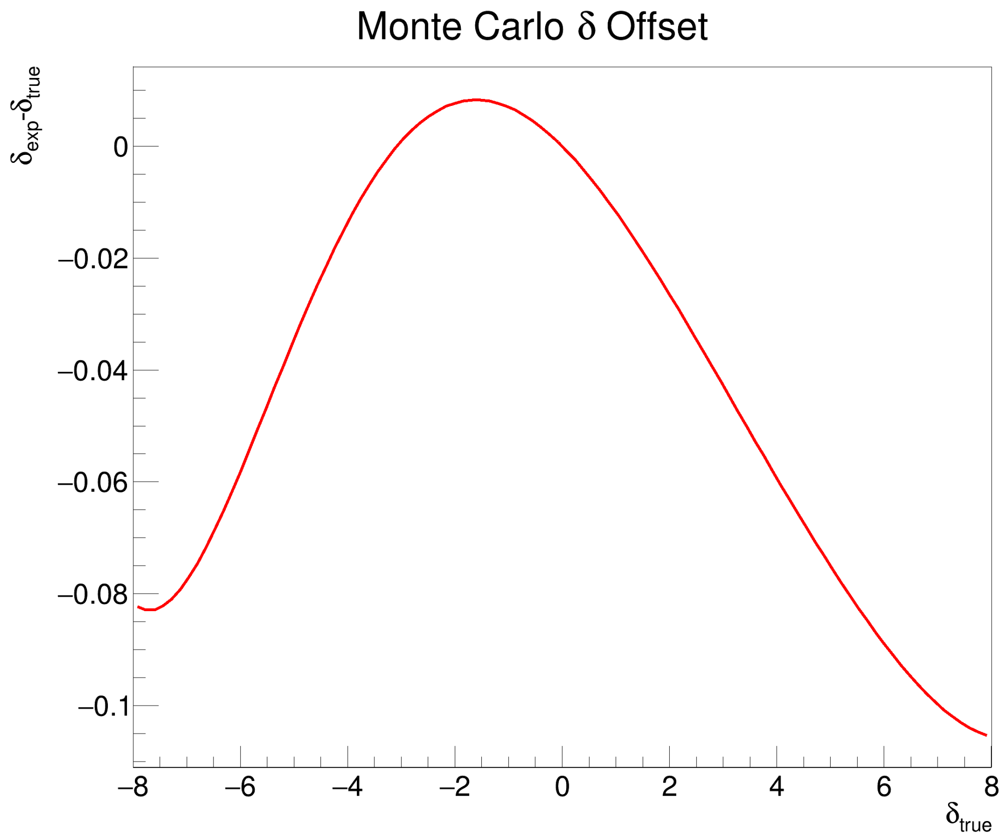

Figure 3.32: The offset between the reconstructed value of δ from the experimental data and the true value from the Monte Carlo. The correction is small, not much larger than 0.1% within the nominal momentum acceptance of the detector, and is on the order of the momentum resolution of the spectrometer. The momentum offset at the central momentum ($\delta_{true} = 0$) is set to 0 because the HMS central momentum offsets have already been determined and corrected for, as shown in Sec. 3.8.

values of δ, shown in Fig. 3.32. This offset does not get much larger than 0.1%, which is within reason as it is comparable to the spectrometer's momentum resolution. To account for the apparent discrepancy between the true and experimentally measured values of δ, this offset is applied on an event-by-event basis as a correction to the δ_{true} values from the Monte Carlo.

3.11 *yTar* Acceptance Correction

The Monte Carlo simulation may not perfectly model the acceptance of the HMS spectrometer. In particular, for the cryogenic targets, which are 10 cm long, we want to know how well the Monte Carlo acceptance function does to reproduce the measured data as a function of y_{tar}, the y-position of the event at the target in the spectrometer's rotated coordinate system.

To determine whether the Monte Carlo represents the y_{tar} acceptance of the spectrometer well, the data to Monte Carlo ratio of several kinematic settings with the spectrometer rotated to 20° was calculated for the aluminum target, which was located closest to the central axis of the spectrometer at $y_{tar} = -0.163$ cm, and the upstream and downstream (aluminum alloy) dummy targets, which were located at $y_{tar} = -1.858$ cm and $y_{tar} = 1.623$ cm, respectively. As shown in Fig. 3.33, these ratios for each of the targets were found to be consistent within uncertainty across multiple different momentum settings, however, the data to Monte Carlo ratios of the dummy targets, which are located at larger y_{tar}, further from the central axis of the spectrometer, were systematically smaller than that of the aluminum target.

To account for the y_{tar} dependence of the data to Monte Carlo ratio, the ratios for the aluminum and dummy targets shown in Fig. 3.33, were fit to a second-order polynomial, modeling the spectrometer's acceptance as a smooth, continuous function of y_{tar}. The Monte Carlo events were then scaled by the value of this fit at the corresponding y_{tar} value, bringing the data to Monte Carlo ratios of the aluminum and dummy targets into agreement with each other. This correction decreased the measured ^{2}H cross sections by 0.7% overall and was found to have little impact on the x_{Bj} dependence of the extracted results.

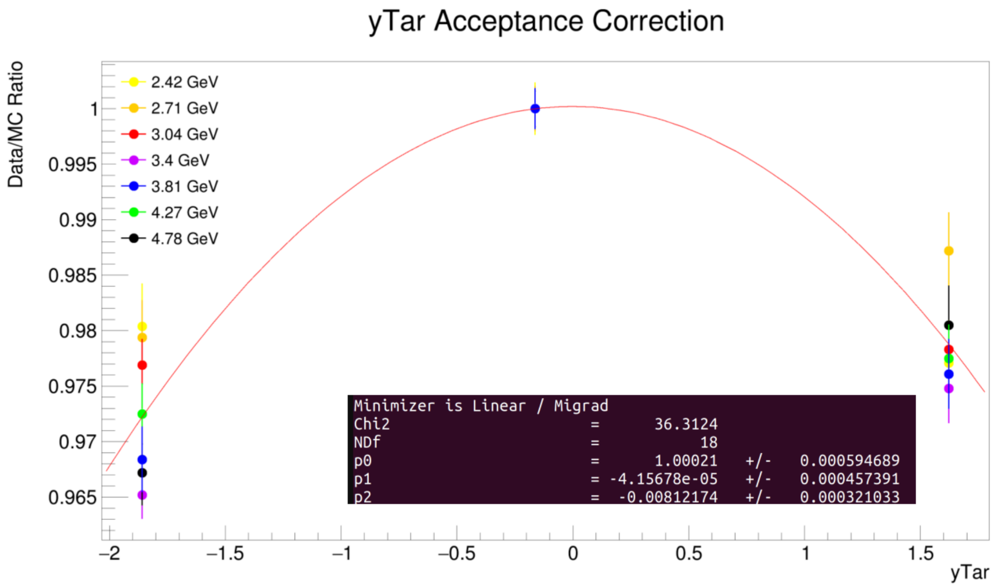

Figure 3.33: Data to Monte Carlo yield ratios for the upstream dummy ($y_{tar} = -1.858$ cm), downstream dummy ($y_{tar} = 1.623$ cm), and aluminum ($y_{tar} = -0.163$ cm) targets at 20° kinematic settings, normalized to the aluminum target ratios. The Monte Carlo appears to not model the $yTar$ acceptance of the spectrometer well, with the data to Monte Carlo yield ratio dropping by several percent for the dummy targets relative to the solid aluminum target, which is closer to the central axis of the spectrometer.

3.12 Background Subtraction

As discussed in Sec. 3.5, the PID cuts used to separate electrons from other particles also remove a small fraction of good electron events. These removed electron events are accounted for by determining the efficiencies of each of the PID cuts. In addition to removing a small number of good electron events, the PID cuts do not remove all of the events that we do not wish to count. These include pion events, as well as events from electrons that did not originate from the beam but were instead created through pair production by high-energy photons in the target, which predominantly result from the decay of π^0 mesons that are generated via photoproduction. These events, which should not be counted when determining the inclusive DIS cross section, are generally referred to as contamination.

3.12.1 Pion Contamination

While the Cherenkov and calorimeter PID cuts remove most of the pion events, a small fraction of pion events remain after both cuts. To get an estimate of how many pion events are getting through both PID cuts, we first form two sets of data with the spectrometer acceptance cuts applied: one with the nominal electron Cherenkov cut used in the analysis, and one with a very tight low-pass Cherenkov cut, requiring that the signal produced in the Cherenkov detector be less than one-tenth of the signal produced when a single photoelectron is emitted from the photocathode of one of the PMTs. The second data set is comprised primarily of pions and serves as a pion sample for the rest of this study.

For a specific type of particle at a given energy, the signal formed in the Cherenkov detector is independent of the signal formed in the calorimeter detector. Therefore, the shape of the calorimeter distribution of the pion sample is the same as the shape of the calorimeter distribution of the pions that passed the nominal electron Cherenkov PID cut. With this information, we can determine the calorimeter distribution of pions in the electron Cherenkov PID cut sample by scaling the calorimeter distribution of the pion sample to match it in the region between $0.1 < H.cal.etottracknorm < 0.4$, where most of the events in the Cherenkov PID cut sample are pions that passed the Cherenkov PID cut. The scaled pion sample provides an approximation of the distribution of pions in the sample of data with the electron Cherenkov PID cut applied. The nominal electron calorimeter cut of $H.cal.etottracknorm > 0.7$ is then applied to the scaled pion distribution to determine the number of pion events that pass both of the PID cuts. This is the estimated pion contamination. To get an

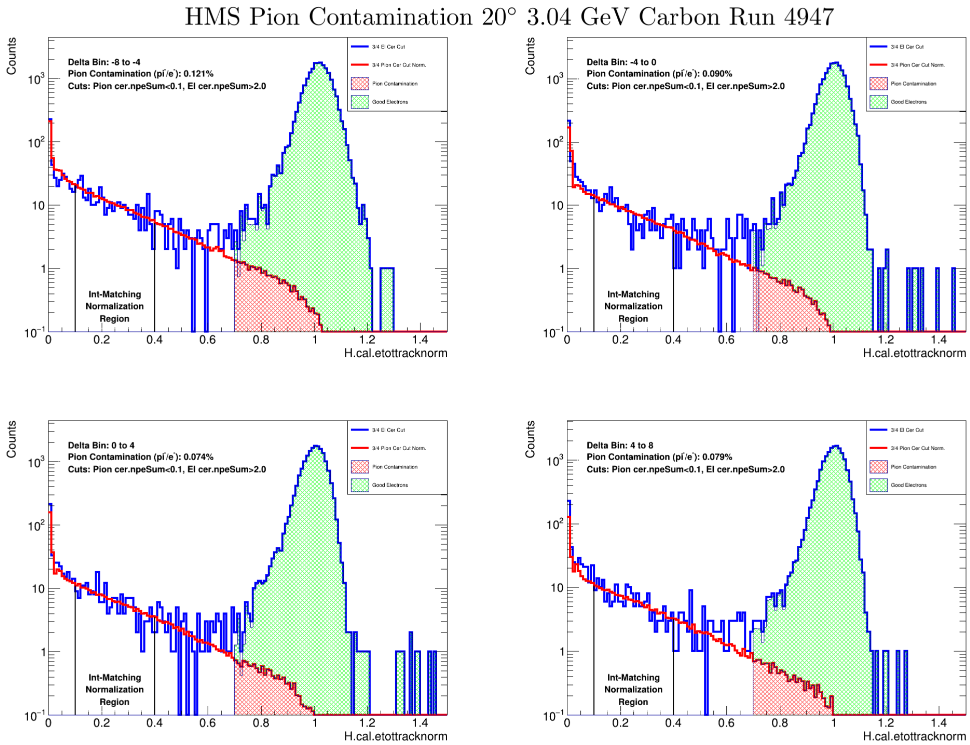

Figure 3.34: Plots showing how the pion contamination estimate is determined. First, two data sets are constructed with cuts on the Cherenkov detector response: one with the cut $H.cer.npeSum < 0.1$, as an estimate of the pion sample, and one with the Cherenkov electron PID cut used in the analysis, $H.cer.npeSum > 2.0$, given by the blue line. The pion sample is then normalized such that its integral in the range $0.1 < H.cal.etottracknorm < 0.4$ is the same as that of the sample with the nominal Cherenkov PID cut. This scaled sample is given by the red line. The red-shaded area represents the estimated pion contamination, and the green-shaded area represents the estimated electron count after the pion contamination has been subtracted.

accurate estimate of the number of electron events in a data set, the estimated pion contamination is subtracted from the data that passed both the Calorimeter and Cherenkov electron PID cuts. The calorimeter distributions of the data sets discussed here are illustrated in Fig. 3.34.

The pion contamination was determined as a fraction of the electron yield, shown for the 20° data in Fig. 3.35. At 20°, this fraction was found to be no larger than 1.5%, and as low as 0.02% for some targets just below the Cherenkov detectors pion

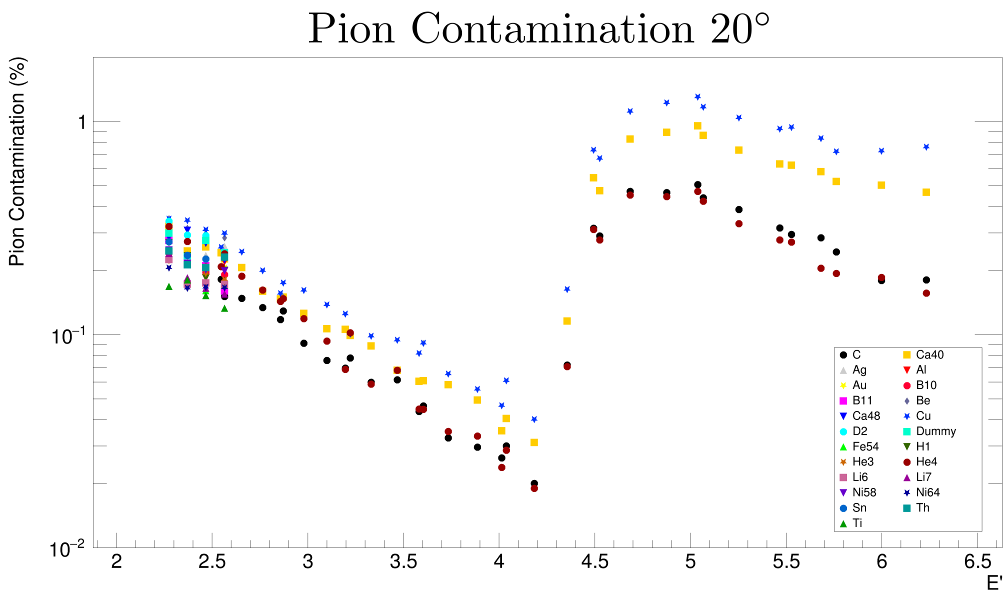

Figure 3.35: Pion contamination results for the 20° data, shown as a function of the measured particle momentum. The pion contamination is found to decrease as the momentum increases, until the pion threshold at a momentum around 4.2 GeV, where the Cherenkov detector loses its ability to distinguish between electrons and pions.

threshold, which is around 4.2 GeV. Above this threshold, the Cherenkov detector cannot be used to distinguish between electrons and pions as both produce Cherenkov radiation, causing the pion contamination to rise.

In addition, above the pion threshold, the procedure described above to determine the pion contamination does not work, as a pion sample can no longer be formed by applying a cut requiring little to no signal in the Cherenkov detector. To handle this problem for kinematic settings with momenta above 4.2 GeV, the pion sample is taken using a data set taken at the same angle and at the highest momentum setting below the Cherenkov detector's pion threshold.

3.12.2 Charge Symmetry of the Pion Background

The charged pions that we observe at positive and negative polarity settings (π^+ and π^-, respectively) are primarily produced via photoproduction:

$$\gamma + p \rightarrow X + \pi^+ \text{ , and}$$
$$\gamma + n \rightarrow X + \pi^- \text{ ,}$$

where X represents all additional outgoing particles. If these processes have similar cross sections and dominate the production of the pion that we observe, then the pion background can be approximated as charge symmetric. If this is the case, it would allow us to account for the pion contamination in the charge-symmetric background (CSB) correction described in the next section, removing the need to use the pion contamination results from the previous section, as well as removing the need to subtract the pion contamination from the positive polarity data before determining the charge-symmetric background correction.

We first need to check if we can reasonably approximate the pion background as being charge symmetric. This is done by calculating the difference between the positive and negative polarity pion yields at a given kinematic and normalizing it by the corresponding electron yield. As shown in Fig. 3.36, the background was found to be nearly charge symmetric, with observed asymmetry being at most a 0.1% of the measured electron yield for the 20° data. Therefore, the pion background was determined to be close enough to charge symmetric that no explicit pion contamination subtraction needs to be performed using the negative polarity data, as it can be accounted for in the charge-symmetric background correction by not subtracting the pion contamination from the positive polarity data, described in the next section.

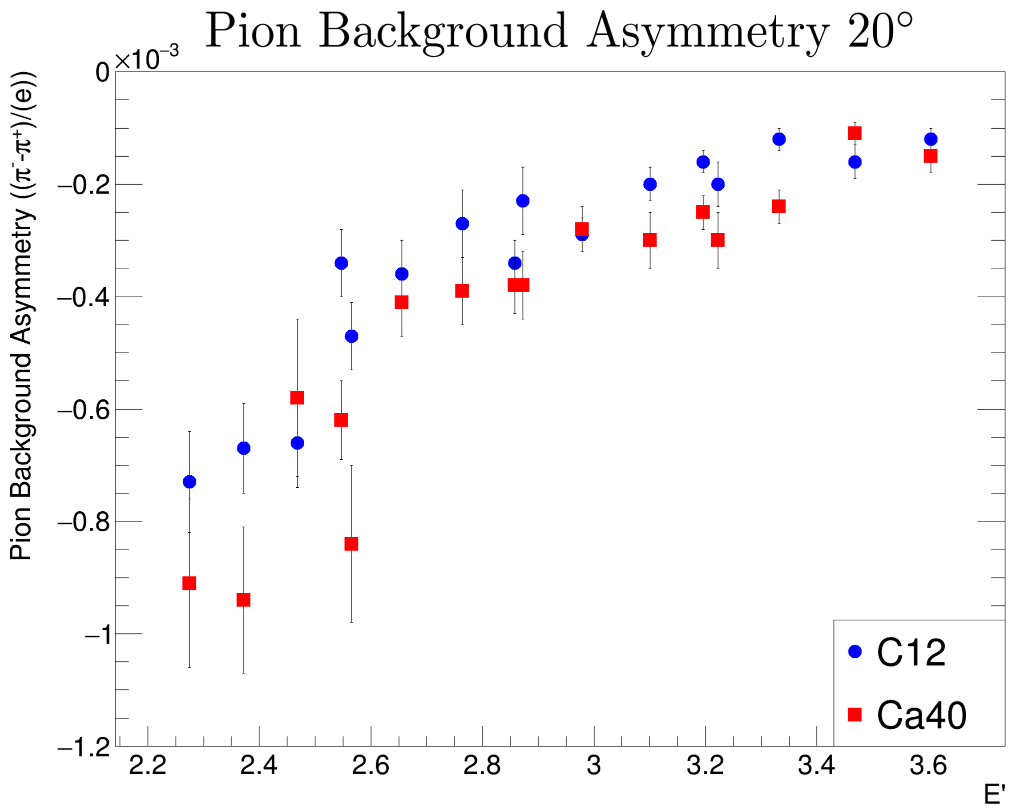

Figure 3.36: Charge asymmetry of pion yields, normalized by the corresponding electron yield, as a function of momentum at 20°. The largest observed asymmetry at this angle is only 0.1% of the corresponding electron yield.

3.12.3 Charge-Symmetric Background

e^+ e^- pairs can be formed via pair production from high-energy photons, forming a charge-symmetric background of positrons and electrons. These pair-produced electrons can enter the detector and are indistinguishable from electrons that originated from the electron beam. As these pair-produced electrons are not from the process that we are trying to measure (usually DIS) but are indistinguishable from the electrons that are, we need to remove them from our data. Fortunately, because there is a positron for each pair-produced electron, we can use the positive polarity data to determine the positron yield, subtract the positron yield from the total electron yield, and find the yield of electrons that we are interested in. In addition, because the pion background was found to be approximately charge symmetric, we chose not to subtract the pion contamination from positive polarity data, instead allowing the pion contamination in the positive polarity to be used to remove the pion contamination from the negative polarity data when the charge-symmetric background is subtracted.

Calorimeter spectra for positive and negative polarity data taken at the same absolute momentum and angle are shown in Fig. 3.37. The same cuts and normalization calculations are used for both the positive and negative polarity data sets in this study, however, the negative polarity data includes one additional cut to account for the fact that the hEL_CLEAN pre-trigger was used instead of the hEL_REAL pre-trigger to form the trigger for positive polarity data in this study, as the hEL_REAL rates at positive polarity kinematics were too high due to proton entering the detector stack. This additional cut on the negative polarity data requires that the hEL_CLEAN pre-trigger fired in addition to hEL_REAL, and can be written as $T.hms.hTRIG3\_tdcMultiplicity \geqslant 1$. This accounts for any differences in the electron efficiencies of the hEL_REAL and hEL_CLEAN pre-triggers.

The yield of the (approximately) charge-symmetric background can be written as

$$Y_{csb} = e^-_{bg} + \pi^-_{bg} = e^+_{bg} + \pi^+_{bg} \ , \tag{3.38}$$

where $e^{-(+)}_{bg}$ is the yield due to the electron (positron) background, and $\pi^{-(+)}_{bg}$ is the yield due to the pion background. The total yield of the negative polarity data can then be written as

$$Y_- = e^-_{beam} + e^-_{bg} + \pi^-_{bg} = e^-_{beam} + Y_{csb} \ , \tag{3.39}$$

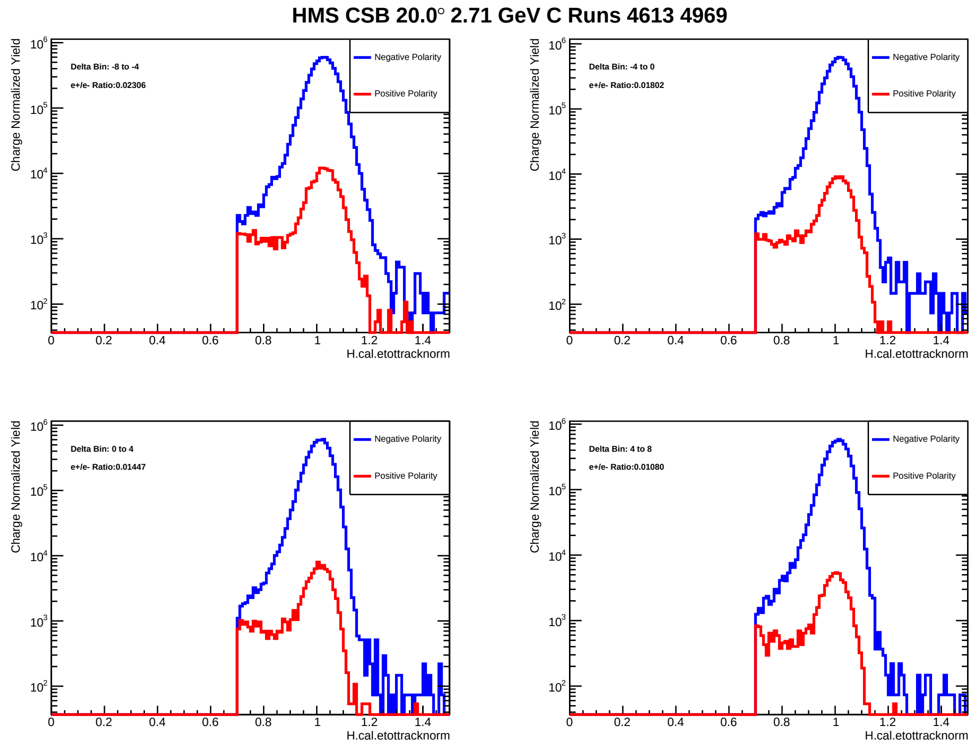

Figure 3.37: Calorimeter spectra for positive and negative polarity data taken at ± 2.71 GeV and 20°. The same electron PID cuts and acceptance cuts were applied to both data sets, and an additional cut requiring the hEL_CLEAN pre-trigger to fire was applied to the negative polarity data for comparison with the positive polarity data that used hEL_CLEAN to form the trigger.

where e^-_{beam} is the yield due to electrons from the beam, which is what we are trying to determine. The total yield of the positive polarity can also be written as

$$Y_+ = e^+_{bg} + \pi^+_{bg} = Y_{csb} \ . \tag{3.40}$$

We can then calculate the ratio of the charge-symmetric background yield to the yield of beam electrons as

$$R_{csb} = \frac{Y_{csb}}{e^-_{beam}} = \frac{Y_+}{Y_- - Y_+} \ . \tag{3.41}$$

The total negative polarity yield can be scaled using this ratio to determine the yield due to electrons from the beam with the equation

$$e^-_{beam} = Y_-(1 + R_{CSB})^{-1} \; . \tag{3.42}$$

The available positive polarity data does not cover the full range of kinematic settings over which negative polarity data was collected, therefore, we must extrapolate R_{csb} to all kinematic settings at which data was collected to correct for the charge-symmetric background in our data. At each spectrometer angle ($20°$, $26°$, and $35°$, R_{csb} was plotted against the spectrometer's central momentum. It was found that the function $f(x) = e^{a+bx}$ fit the existing data well and was therefore used to determine R_{csb} for all targets and kinematic settings. Fits of R_{csb} for all targets at $20°$ are shown in Fig. 3.38. In general, for a given target, the charge-symmetric background was found to decrease exponentially as a function of momentum and increase as a function of angle. In addition, the size of the charge-symmetric background was found to roughly correlate with target radiation lengths, with the thickest targets having the largest backgrounds.

As discussed in Sec. 3.12.1, there is a sudden increase in the pion contamination around $E' = 4.2$ GeV as the Cherenkov detector's pion threshold is crossed. This jump is not accounted for in the R_{csb} fits, as all positive polarity data was collected below $E' = 4.2$ GeV. Positive polarity data was not collected at higher momenta at $20°$ because pion and pair-produced electron backgrounds fall off rapidly as E' increases and are relatively tiny above $E' \approx 4.0$ GeV. Therefore, an additional uncertainty is applied in the cross section ratio results above 4.0 GeV to account for differences in the pion contamination between targets.

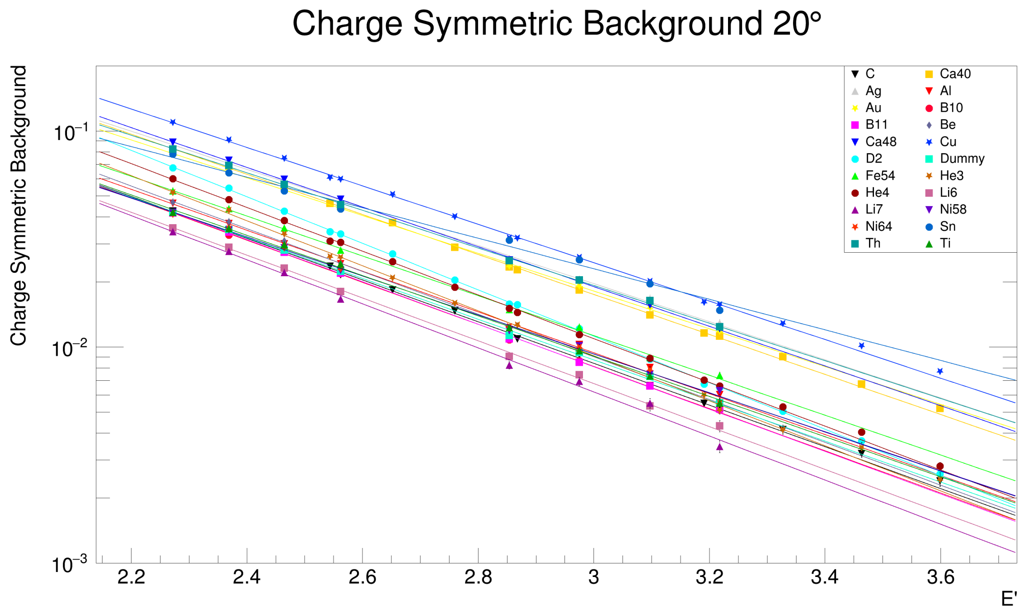

Figure 3.38: R_{csb} plotted as a function of the spectrometer's central momentum for the 20° data. Comparison with Fig. 3.35 shows that the charge symmetric background is primarily composed of pair-produced electrons at these kinematics as opposed to pions. A fit of the form $f(x) = e^{a+bx}$ was found to model the charge-symmetric background well for all targets except for tin (Sn). This occurred because the Tin target deformed over the course of the experiment, causing the target thickness to change from kinematic setting to kinematic setting. At this time, it is unknown whether it will be reasonably possible to extract any meaningful results from the data collected on the tin target.

3.13 Experimentally Measured Yield

The experimentally measured yield Y_{exp} is defined as the number of beam electrons that scattered from the target within a specified kinematic range, normalized by the total charge of the beam electrons that were incident on the target. Starting with the raw number of events that passed the electron PID cuts $N_{e^-}^{raw}$, one can apply the corrections described previously in this chapter and calculate the experimentally measured yield as

$$Y_{exp} = N_{e^-}^{raw} \frac{f_{ps}}{(1 + R_{csb}) \cdot Q \cdot t_{tlt} \cdot \epsilon_{track}^{e^-} \cdot \epsilon_{cal} \cdot \epsilon_{cer}} , \tag{3.43}$$

where f_{ps} is the prescale factor, R_{csb} is used to remove the charge-symmetric background (see Sec. 3.12.3), Q is the total charge of the beam electrons that were incident on the target, t_{tlt} is the total live time which is given by the computer live time for our analysis (Sec. 3.7), $\epsilon_{track}^{e^-}$ is the electron tracking efficiency (Sec. 3.6), ϵ_{cal} is the calorimeter PID cut efficiency (Sec. 3.5.1), and ϵ_{cer} is the Cherenkov detector PID cut efficiency (Sec. 3.5.2). When determining the yield for a cryogenic target such as ^{2}H, the yield due to the target cell is subtracted and a boiling correction is applied, as discussed in Sec. 3.9. For solid targets such as ^{48}Ca that are contaminated with a small percentage of different nuclei, the yield from these contaminating nuclei is subtracted from the total yield, isolating the contribution from the primary nucleus.

3.14 Born Cross Section Model

From the electron yields, cross sections are extracted using the Monte Carlo ratio method. This method, as well as the Monte Carlo simulation code used in this analysis, are described in more detail in later sections. Now, we will cover the Born cross section models which, after radiative corrections are applied, are used to weight the events from the Monte Carlo simulation.

The results presented in this work use a hybrid model to estimate Born cross sections. In this model, the total Born cross section is divided into separate quasielastic and inelastic components that each have their own model. The total model Born cross section can be written in terms of the model inelastic and quasielastic cross sections (σ_{IN} and σ_{QE}) as

$$\sigma_{born}^{model} = \sigma_{IN}^{model} + \sigma_{QE}^{model} \ . \tag{3.44}$$

The quasielastic cross section is determined from a fit [75] of empirical data that uses equations derived from a superscaling treatment of electron scattering [76]. The inelastic cross section is determined using an updated version of the deuterium fit given in Ref. [75], which has been used in the analysis of experiments such as that described in Ref. [77], with an EMC effect applied for heavier nuclei.

Initially, the model Born cross sections often do not agree well with the measured Born cross sections. To account for their differences, small perturbations are applied to the model to bring the model Born cross sections into agreement with the measured values. This is important because the model Born cross section is used as input into the radiative correction model, and an incorrect model Born cross section results in an inaccurate determination of the radiative correction. This in turn causes the extracted Born cross section to become incorrect. By iteratively applying small changes to the Born cross section model to bring it into agreement with the measured result, a more accurate radiative correction, and therefore a more accurate measured Born cross section, is obtained. The results shown here were extracted using cross section models that have not yet been fully iterated in this fashion.

3.14.1 Radiative Corrections

Radiative corrections are applied to the model Born cross sections described in the previous section before they are used to weight the Monte Carlo events. The radiated cross sections σ_{rad} account for additional interactions, beyond the single-photon exchange quantified by the Born cross section, that electrons may have as they travel through the target material and into the detector. These radiated cross sections, where additional interactions are accounted for, reflect what is observed in the experiment.

Radiative corrections can be divided into two main categories: internal and external. Internal radiative corrections handle the effects of processes such as vacuum polarization, vertex corrections, and internal Bremsstrahlung, which occur in the field of the primary scattering nucleus and are not accounted for in the Born approximation. On the other hand, external radiative corrections account for energy lost by the electrons in processes such as bremsstrahlung or ionization as they enter and exit the target material and travel to the detector hut. External radiative corrections are functions of the thickness of the materials that the electron must travel through before and after scattering. Therefore, to keep the size of external radiative corrections small, thin targets are used, and the total thickness of the material between the target and the detector (scattering chamber and spectrometer windows, air) is kept to a minimum.

The radiative corrections used in this analysis were calculated using the *rc_externals* program. This program is derived from the software used for radiative corrections at SLAC. This program is based on the formalism described in Ref. [78], and its implementation is described in Refs. [79] and [7]. Figure 3.39 shows radiative correction factors ($\sigma_{rad}/\sigma_{born}$) for several targets at 20° as a function of x_{Bj}, while Fig. 3.40 shows the corresponding model born and radiated cross sections.

3.14.2 Coulomb Corrections

Electrons accelerate in the Coulomb field of a target nucleus before and after scattering from it. This causes the energy of the incoming and outgoing electrons at the interaction vertex to be larger than if the Coulomb force were not present. In addition, the Coulomb attraction results in a focusing of the wavefunction of the incoming electron towards the to-be-struck nucleus. Because both of these effects impact the

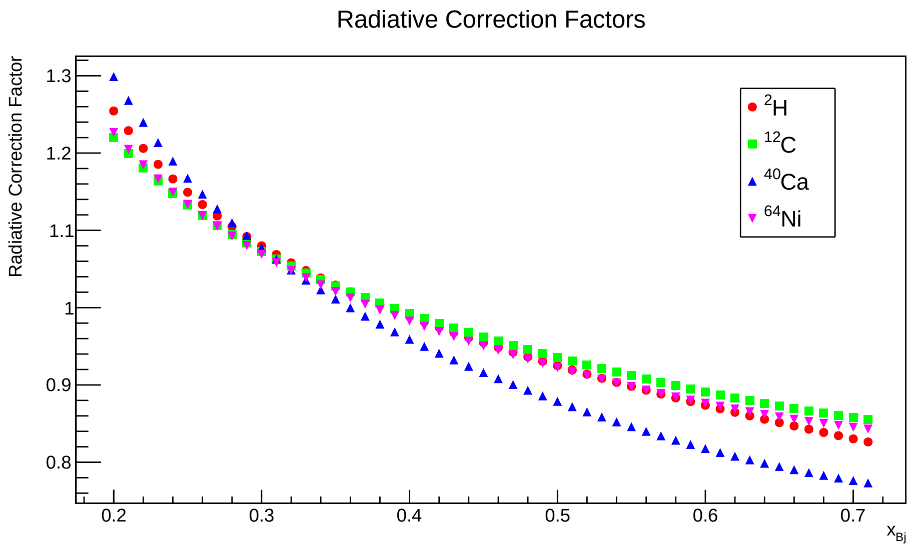

Figure 3.39: Radiative correction factors ($\sigma_{rad}/\sigma_{born}$) for several targets at 20° as a function of x_{Bj}. The radiative correction factor decreases with x_{Bj} in the EMC effect region. Note that the radiative correction factors generally change faster with x_{Bj} for thicker targets.

measured cross section, they must be corrected for in the analysis.

In this analysis, where the scattered electron's initial and final state energies are several GeV, Coulomb corrections are determined using the improved Effective Momentum Approximation (EMA) which accounts for these two effects [80]. First, the enhancement of the electron's kinetic energy at the scattering vertex is calculated. Approximating nuclei as uniformly charged spheres with charge Z and radius R_0, the change in potential seen by a particle falling radially into the sphere from infinitely far away is given by

$$\Delta V(z) = V(\infty) - V(z) = -\frac{Z\hbar\alpha c}{2R_0}\left(3 - \frac{z^2}{R_0^2}\right) \ , \tag{3.45}$$

for $z < R_0$, where α is the Sommerfeld constant, $\hbar$ is the Planck constant, and c is the speed of light in vacuum. If the electron scatters at the center of the sphere, the

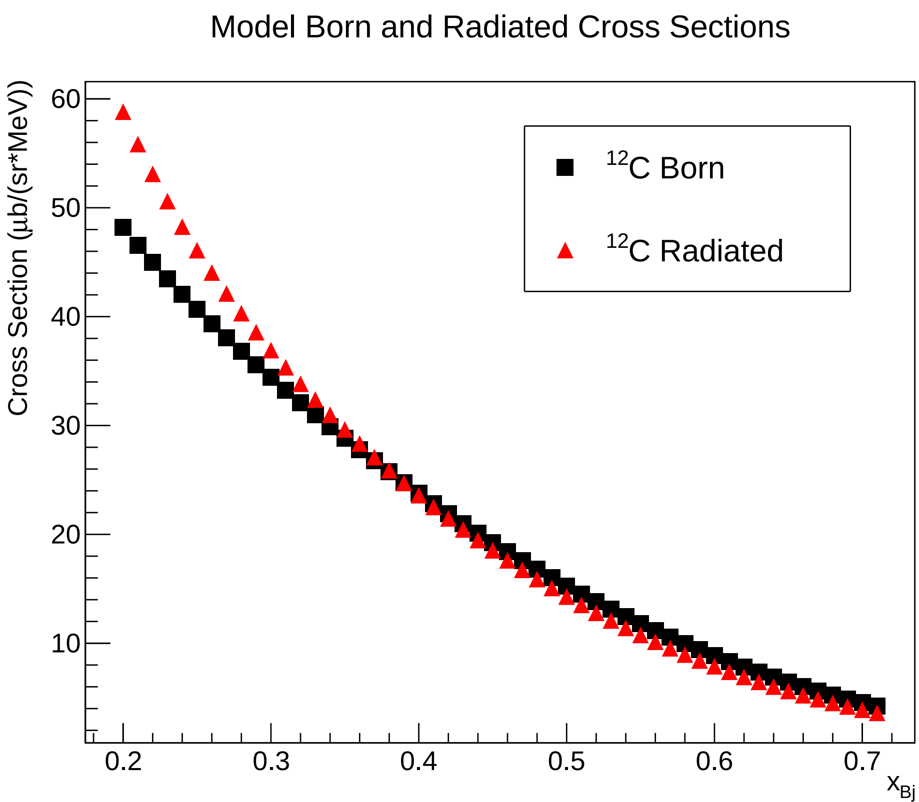

Figure 3.40: Model born and radiated cross sections for the ^{12}C target at 20°.

kinetic energy it gains due to the Coulomb field is given by

$$\Delta E(0) = -\Delta V(0) = V_0 = \frac{3(Z-1)\hbar\alpha c}{2R_0} \ , \tag{3.46}$$

where $Z - 1$ is used in place of Z to account for the fact that Coulomb corrections are typically not performed for $Z = 1$ nuclei (^{1}H, ^{2}H), and ^{2}H forms the denominator of EMC ratios, which we are trying to calculate. Now, not every electron will scatter from the geometric center of a nucleus. Consequently, the energy enhancement calculated in Eq. 3.46 is an overestimate of the true value. It has been found that an effective potential between 0.75 and 0.8 V_0 provides reasonable results [80]. In this study, the central value of this range was used, such that

$$\Delta E = -0.775 V_0 \ . \tag{3.47}$$

The RMS charge radius R_0 for a given nucleus is required to calculate V_0 to determine ΔE as given by Eq. 3.47. For heavy nuclei, this is determined with

$$R_0 = 1.1 A^{1/3} + 0.86 A^{-1/3} \text{ fm} \ , \tag{3.48}$$

where A is the mass number of the corresponding nucleus [81]. Charge radii are not required for the $Z = 1$ ^{1}H and ^{2}H targets as Coulomb corrections are not applied for those nuclei, and measured RMS charge radii from Ref. [82] are used for ^{3}He and ^{4}He. RMS Charge radii and the corresponding effective vertex energy enhancements for the nuclei measured in E12-10-008 are shown in Tab. 3.5.

Next, the focusing of the incident electron wave function due to the Coulomb field must be accounted for. The focusing factor appears in the incoming (outgoing) distorted electron wave function as $k'_{i(f)}/k_{i(f)}$, where $k'_{i(f)}$ is the effective incoming (outgoing) electron momentum at the interaction vertex after being enhanced in the Coulomb field, and $k_{i(f)}$ is the incoming (outgoing) electron momentum if the Coulomb field were not present. At highly relativistic energies, these focusing factors can be written as

$$\frac{k'_{i(f)}}{k_{i(f)}} = \frac{E_{i(f)} + \Delta E}{E_{i(f)}} \ , \tag{3.49}$$

where E_i is the energy of the incoming electron and E_f is the energy of the outgoing electron. In the EMA, the incoming focusing factor appears quadratically in the cross section.

The Coulomb correction factor to the cross section can then be given by the ratio

Nucleus	R_0 (fm)	ΔE (MeV)
^{3}He	1.97	0.85
^{4}He	1.68	1.0
^{6}Li	2.47	1.36
^{7}Li	2.55	1.31
^{9}Be	2.70	1.875
^{10}B	2.77	2.42
^{11}B	2.83	2.37
^{12}C	2.89	2.92
^{27}Al	3.59	5.60
^{40}Ca	4.01	7.93
^{48}Ca	4.23	7.52
^{48}Ti	4.23	8.31
^{54}Fe	4.39	9.53
^{58}Ni	4.48	10.1
^{64}Cu	4.59	10.2
^{64}Ni	4.62	9.78
^{108}Ag	5.42	14.2
^{119}Sn	5.59	14.7
^{197}Au	6.55	19.9
^{232}Th	6.90	21.6

Table 3.5: RMS charge radii and Coulomb energy enhancements for the targets studied in E12-10-008. For targets that are not isotopically enriched, the natural abundance-weighted average mass number rounded to the nearest integer is used in the calculation of the RMS charge radius.

of Born cross sections with and without Coulomb-corrected electron vertex energies multiplied by the inverse square of the incoming focusing factor, written as

$$f_{coulomb} = \frac{\sigma(E,E')}{\sigma(E+\Delta E, E'+\Delta E)}\left(\frac{E}{E+\Delta E}\right)^2 . \tag{3.50}$$

Coulomb corrections for several targets at 20° are shown as a function of x_{Bj} in Fig. 3.41. It should be noted that, while there is a general consensus that the improved EMA is valid for quasielastic scattering, it is unclear whether it is also appropriate for DIS. To address this, an experiment has been proposed at Jefferson Lab that would

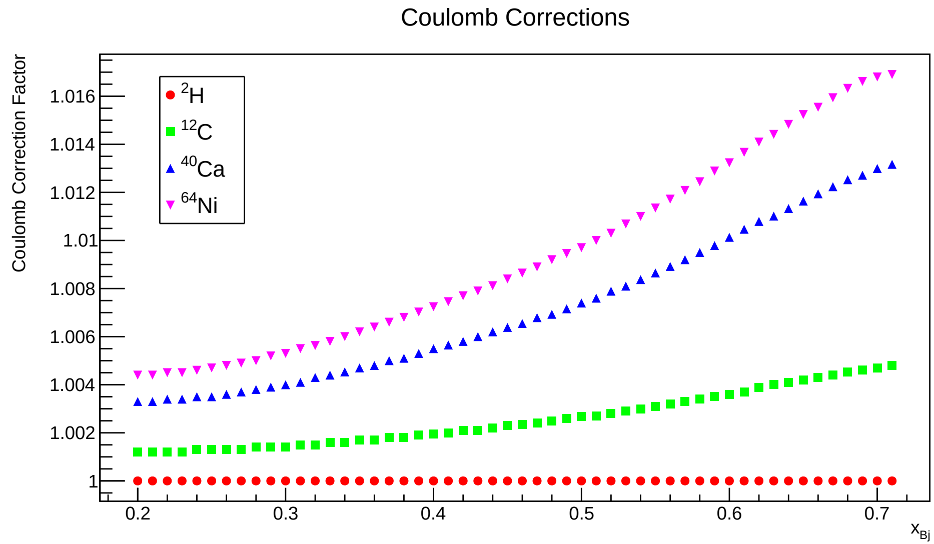

Figure 3.41: Coulomb corrections for several targets at 20° as a function of x_{Bj}. Coulomb corrections generally increase with the number of protons in the nucleus. They also monotonically increase with x_{Bj} in the EMC effect region ($0.3 < x_{Bj} < 0.7$).

use an electron beam alongside a new positron beam to study Coulomb corrections in the DIS regime [83].

3.15 Simulated Yield

The Monte Carlo simulation code used in Hall C for inclusive scattering analysis is *mc-single-arm* [84]. This program consists of three main parts:

1. An event generator that randomly produces events distributed uniformly in δ, x'_{tar}, and y'_{tar} over a given kinematic range. The beam-target interaction point is randomly selected over the target length and rastered beam spot size.

2. Multiple scattering is calculated in the target, target cell walls, scattering chamber window, air, and spectrometer entrance window, and events are propagated through the spectrometer collimator, magnets, and into the detector hut.

Events that fail to pass through the collimator or are otherwise prevented from entering the detector hut are flagged.

3. Events are transported through the detector stack to check if they hit each of the detectors. The event position at each of the drift chambers is randomly shifted according to the drift chamber resolution, and kinematic quantities (δ, y_{tar}, y'_{tar}, and x'_{tar}) are reconstructed using the optics matrix from the simulated variables in the detector, that is, the same way as for real measured data.

Once the events have been simulated by the Monte Carlo, they are each weighted as

$$w = \sigma_{rad} \cdot f_{ps} \cdot f_{yTar} \frac{\Delta x'_{tar} \cdot \Delta y'_{tar} \cdot \Delta\delta \cdot \rho \cdot l \cdot N_A}{e \cdot M \cdot N_{events}} , \tag{3.51}$$

where σ_{rad} is the radiated cross section described in Sec. 3.14.1, f_{ps} is the Monte Carlo phase space correction which will be discussed in Sec. 3.15.1, f_{yTar} is the y_{Tar} acceptance correction discussed in Sec. 3.11, $\Delta x'_{Tar}$, $\Delta y'_{Tar}$, and $\Delta\delta$ are the sizes of the generation ranges of the corresponding kinematic variables (for example, if the simulation generates events in the range $-10\% < \delta < 10\%$, then $\Delta\delta = 20\%$), ρ is the mass density of the target material, l is the length of the target along the beam direction, N_A is Avagadros number, e is the electric charge of an electron, M is the molar mass of the target material, and N_{events} is the total number of simulated events. The simulated yield can then be determined by adding the weights for all events in a given kinematic bin. The corrected value for δ is used when binning for comparison with experimental data as opposed to the reconstructed value of δ from the Monte Carlo, as discussed in Sec. 3.10.

3.15.1 Monte Carlo Event Generation Correction

The Hall C single arm Monte Carlo program, *mc-single-arm*, generates events uniformly along the length of the target and in x'_{tar}, y'_{tar} and δ. The quantities x'_{tar} and y'_{tar} are defined as

$$x'_{tar} = \frac{dx}{dz} \ , \tag{3.52}$$

$$\text{and} \quad y'_{tar} = \frac{dy}{dz} \ , \tag{3.53}$$

where the positive z-direction points along the central axis of the spectrometer, the positive x-direction points downwards, and the positive y-direction points spectrometer-left. Because events are generated uniformly in x'_{tar} and y'_{tar}, they are not generated uniformly in a spherical coordinate system. With the small angular acceptance of the HMS, this effect is very small because $\tan(\theta) \approx \theta$ at small angles; however, it is non-zero and should be corrected. This is accomplished to first order by first constructing the Jacobian

$$J = \begin{bmatrix} \frac{d\cos(\theta)}{dx'_{tar}} & \frac{d\cos(\theta)}{dy'_{tar}} \\ \frac{d\phi}{dx'_{tar}} & \frac{d\phi}{dy'_{tar}} \end{bmatrix} \ , \tag{3.54}$$

where θ is the polar angle and ϕ is the azimuthal angle. The determinant of the Jacobian is then calculated, which, after simplification, comes to

$$\det J = \frac{1}{(1 + {x'_{tar}}^2 + {y'_{tar}}^2)^{3/2}} \ . \tag{3.55}$$

The Jacobian determinant is calculated for each event generated by the Monte Carlo and is included in its normalization factor through multiplication.

3.16 Born Cross Section Extraction

With the measured and simulated electron yields determined, the next phase of the analysis process is to extract measured Born cross sections. The first step in this extraction is to take ratios of the measured and simulated electron yields. These ratios provide information about how close the model Born cross section is to the measured Born cross section. With a first pass of ratios determined, the Born cross section model is then iterated to bring the measured and simulated yields into better agreement such that the yield ratios, and therefore the ratios of measured Born cross sections to model Born cross sections, are close to unity. This iteration process is important because yield ratios that are far from unity are not equal to the measured-to-model Born cross section ratios, as the radiative corrections used to weight the simulated yield have been determined with incorrect model Born cross sections, and therefore cannot be used to extract measured Born cross sections.

Once the model has been iterated such that the ratio of measured and simulated yields is 1.0 within uncertainties, the measured Born cross section is extracted by weighting the yield ratio by the model Born cross section and the Coulomb correction, written as

$$\sigma_{born}^{meas} = \frac{Y_{Data}}{Y_{MC}(\sigma_{rad}^{model})} \cdot \sigma_{born}^{model} \cdot f_{coulomb} \tag{3.56}$$

where Y_{Data} is the electron yield extracted from the data, $Y_{MC}(\sigma_{rad}^{model})$ is the electron yield from the Monte Carlo simulation which is weighted by the radiated cross section, and $f_{coulomb}$ is the Coulomb correction defined in Sec. 3.14.2. Figure 3.42 shows the measured and simulated yields and their ratio for the ^{12}C target at one kinematic setting.

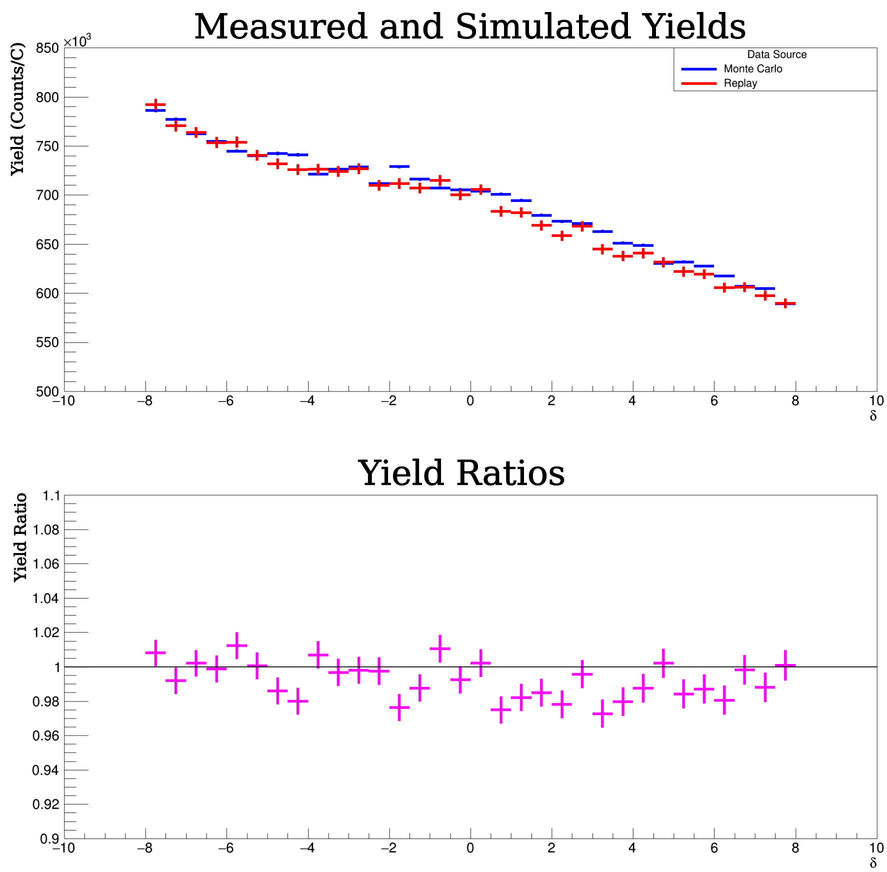

Figure 3.42: (Top) Measured and simulated electron yields for the ^{12}C target at an HMS angle of 20° and central momentum of 3.4 GeV plotted as functions of δ, which is the electron momentum measured relative to the spectrometer's central momentum in percent. (Bottom) The ratio of the measured and simulated electron yields (shown above) as functions of δ, illustrating the relative behavior of the two yields.

3.17 Calculating EMC Ratios

The final step in the analysis process is to extract per-nucleon Born cross section (EMC) ratios of our measured target nuclei to ^{2}H using the measured Born cross sections. Now, the denominator in an EMC ratio is the per nucleon cross section of ^{2}H, which, having equal numbers of protons and neutrons, is an isoscalar nucleus. Protons and neutrons are known to have different cross sections. Therefore, in order to study how the DIS cross section of an average nucleon in a target nucleus is modified relative to deuterium, one must account for any difference between the relative numbers of protons and neutrons in the target nucleus and deuterium.

Given the per nucleon cross section ratio between a target nucleus of charge Z and mass number A, and ^{2}H, the isoscalar corrected ratio can be written as

$$\left(\frac{\sigma_A}{\sigma_{^2\mathrm{H}}}\right)_{iso} = \left(\frac{\sigma_A}{\sigma_{^2\mathrm{H}}}\right)\frac{\frac{1}{2}(\sigma^n + \sigma^p)}{\frac{1}{A}(Z\sigma^p + (A-Z)\sigma^n)}\ , \tag{3.57}$$

which can be written in terms of the structure function ratio F_2^n/F_2^p as

$$\left(\frac{\sigma_A}{\sigma_{^2\mathrm{H}}}\right)_{iso} = \left(\frac{\sigma_A}{\sigma_{^2\mathrm{H}}}\right)\frac{\frac{1}{2}(F_2^n/F_2^p + 1)}{\frac{1}{A}(Z + (A-Z)F_2^n/F_2^p)}\ . \tag{3.58}$$

While there are several models for the ratio F_2^n/F_2^p from fits of empirical data, the results presented here use that which is described in Ref. [85] for the deuteron, which takes into account the effects of "smearing". Figure 3.43 shows the F_2 ratio for the "free" nucleon at $Q^2 = 12$ GeV^2. A new fit from the CJ collaboration [86] that includes more recently published measurements, such as those from the MARATHON collaboration [87], is being considered for the extraction of final results.

3.18 Systematic Uncertainties

The systematic uncertainties for the preliminary results presented here are based on those used in the analysis of the published results from the commissioning run for this experiment (E12-10-008) [31]. A detailed discussion of these uncertainties can be found in Ref. [88]. Uncertainties used in this analysis are summarized in Tab. 3.6. The uncertainties on the measured EMC ratios are divided into three main categories: point-to-point, x_{Bj}-correlated, and scale (normalization).

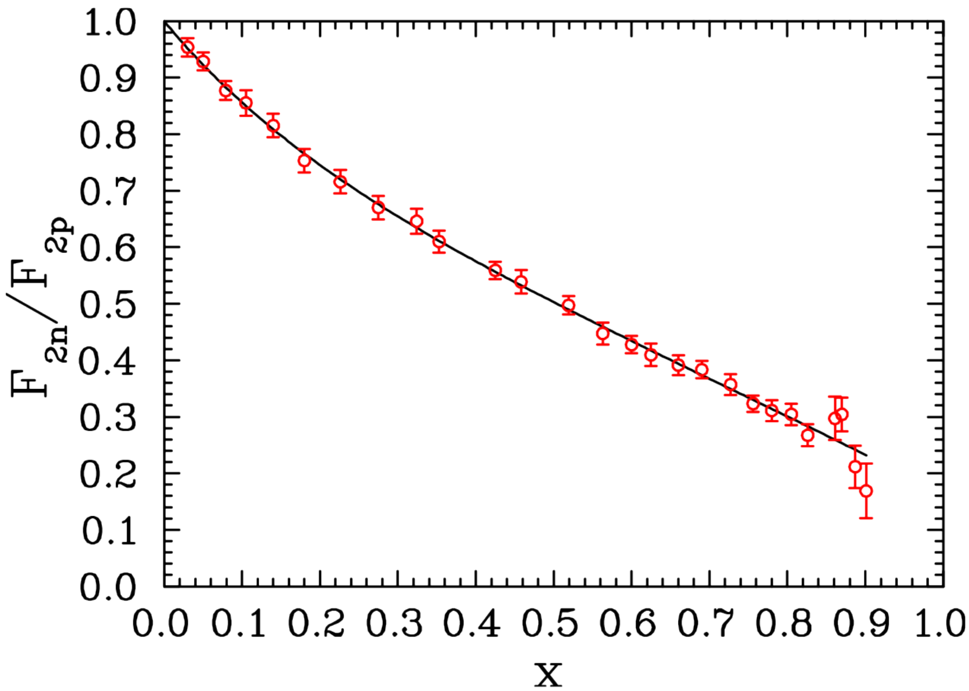

Figure 3.43: Figure from [85]. F_2 ratio at $Q^2 = 12$ GeV from the model described therein for the "free" nucleon. The F_2 ratio used in this analysis is that of that deuteron.

- **Point-to-Point:**

  Point-to-point uncertainties are considered independent from one kinematic point to the next. They include uncertainties associated with the radiative corrections procedure and detector efficiencies.

- x_{Bj} **Correlated:**

  x_{Bj} correlated uncertainties vary in magnitude with x_{Bj}, but impact all points in the same direction. These uncertainties stem from the precision of measurements related to x_{Bj}, such as the incoming and outgoing electron momenta and the angle of the outgoing electron.

- **Scale (Normalization):**

Scale or normalization uncertainties affect all data points uniformly, scaling them by a constant multiplicative factor. These arise due to uncertainties in quantities such as the measured target thicknesses.

Source	Absolute Uncertainty	Relative Uncertainty	$\delta\sigma/\sigma$ (%)	$\delta R/R$ (%) point-to-point	$\delta R/R$ (%) scale	$\delta R/R$ (%) correlated
HMS Momentum	0.1%	0.01%	0.1-2.5	-	-	0.1-1.0
Beam Energy	0.1%	0.005%	0.1-0.5	-	-	0.0-0.5
θ	0.5 mr	0.2 mr	0.5-3	-	-	0.01-0.5
Beam Charge	0.40%	0.35%	0.53	0.35	-	-
^{2}H Heating	0.19%	0.05%	0.19	0.05	0.19	-
Tracking Efficiency	1.0%	0.04%	1.0	-	-	-
Trigger Efficiency	-	0.02%	0.02	-	-	-
Dead Time	0.1%	-	0.1	0.14	-	-
CSB	0.1%	-	0.1	0.14	-	-
Pion Contamination	-	0.1-0.3%	-	0.1-0.3	-	-
Radiative Corrections	1.0%	0.5%	1.1	0.55	0.5	-
y_{Tar} Acceptance	0.4%	-	0.4	-	0.4	-
Detector Efficiency	0.1%	-	0.1	0.14	-	-
Target Thickness	0.13-1.18%	-	0.13-1.18	-	0.13-1.18	-
Cryo Cell Subtraction	0.95%	-	0.95	-	0.95	-

Table 3.6: Summary of the experimental systematic uncertainties. The pion contamination uncertainty is applied above the Cherenkov pion threshold, where the CSB fit (see Sec. 3.12.3) cannot be applied.

Chapter 4

Results and Discussion

This chapter presents preliminary results from analysis of the data collected during experiment E12-10-008. These include measurements of cross section (EMC) ratios covering a kinematic range of $0.18 < x_{Bj} < 1.0$ and $2.8 < Q^2 < 8.1$ GeV^2, and EMC slopes in ^{12}C, ^{27}Al, ^{40}Ca, ^{48}Ca, ^{48}Ti, ^{54}Fe, ^{58}Ni, ^{64}Ni, and ^{197}Au. These results are discussed in the context of theoretical predictions and previous experimental data, which are covered in Ch. 1. Finally, several measurements of the EMC effect which will or may be performed in the coming decade are discussed.

4.1 Cross Section Ratios

This section covers the measured EMC ratios, defined in Eq. 3.58, that were determined using data collected using the HMS at 20.00°, spanning a kinematic range of $0.18 < x_{Bj} < 1.0$ and $2.8 < Q^2 < 8.1$ GeV^2. In addition, the EMC slopes calculated from these ratios will be presented. The cross section ratios were calculated in 1% bins in δ for each spectrometer momentum setting and rebinned into bins of size 0.025 in x_{Bj}. At 20.00°, the HMS central momentum was set to ten different values to collect data covering the full kinematic range specified above: 2.42 GeV, 2.71 GeV, 3.04 GeV, 3.40 GeV, 3.81 GeV, 4.27 GeV, 4.78 GeV, 5.36 GeV, 5.878 GeV, and 6.60 GeV. However, one should note that most of the data collected at the 6.60 GeV setting falls outside of the specified kinematic range, going to $x_{Bj} > 1$, and is used for studies of

SuperFast Quarks (SFQs) [53].

The measured EMC ratios for the targets listed at the beginning of this chapter are shown in Figs. 4.1-4.9 with error bars representing combined statistical and point-to-point systematic uncertainties. These ratios are shown alongside previous world data with consistent Coulomb and isoscalar corrections applied, and a fit to the SLAC E139 results [23]; no Coulomb corrections and different isoscalar corrections were used back when the SLAC fit was obtained, resulting in some difference between the SLAC fit and results shown in the figures. An error band illustrating the x_{Bj}-correlated uncertainties is shown in Fig. 4.1. This is only included for the carbon data, as these uncertainties are largely target-independent. Normalization uncertainties are indicated in parentheses next to the experiment name in the legend of each figure. The ratios for each target show the EMC effect's general characteristic shape as a function of x_{Bj}. However, while previous measurements of EMC ratios show that they decrease approximately linearly in the range $0.3 < x_{Bj} < 0.7$, reaching a local minimum around $x_{Bj} = 0.725$, our preliminary results show that the EMC ratios only decrease linearly to $x_{Bj} = 0.6$, remaining relatively flat in the range $0.6 < x_{Bj} < 0.7$. This appears to be the case for the published commissioning data for our experiment [31] (labeled XEM18) as well. For nuclei such as ^{48}Ca and ^{48}Ti, there appears to be an anomalously large offset at low-mid x_{Bj} between our data and the SLAC fit. It is unclear if this offset is the result of an anomalously large error in the normalization of our data, or if it is a genuine feature of the EMC effect for these nuclei. Finally, it should be noted that our data are not expected to agree with the SLAC fit above $x_{Bj} > 0.9$ due to the differing kinematics of the two experiments, which result in different quasielastic contributions around $x_{Bj} = 1$.

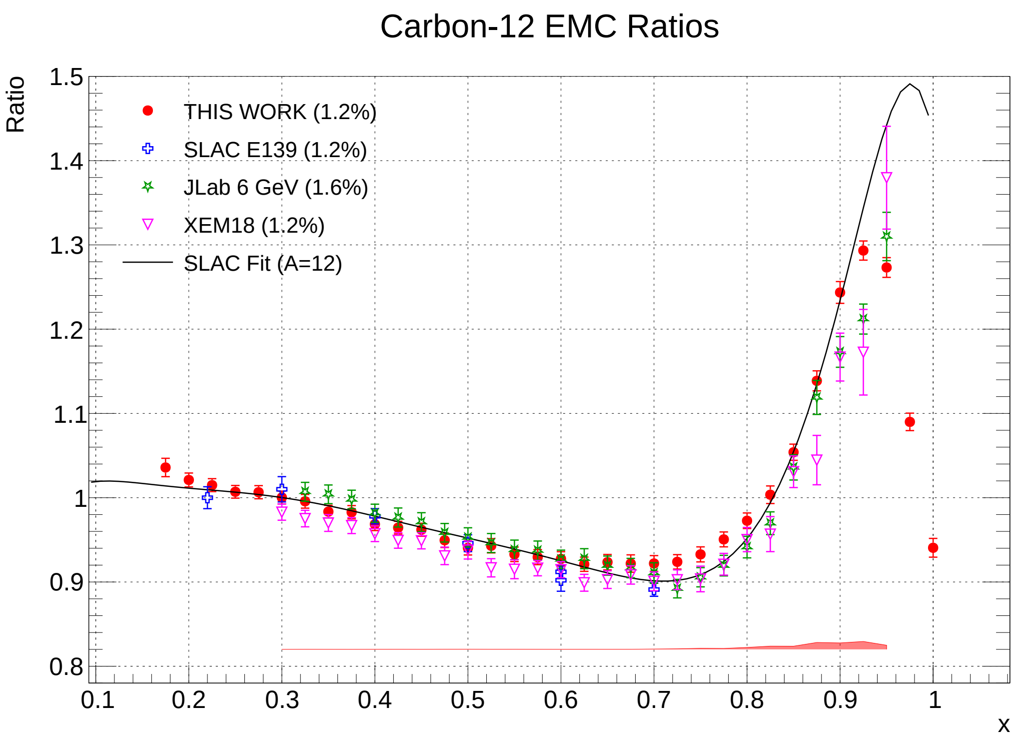

Figure 4.1: EMC ratios from this work for ^{12}C are shown alongside a fit to the SLAC E139 results [23] and results from the JLab 12 GeV commissioning data (open magenta triangles) [31], the JLab 6 GeV results (open green stars) [29], and the results from SLAC E139 (open blue plus signs) [23]. The normalization uncertainty of each of the experiments is shown in parentheses next to the experiment name in the legend, and the x_{Bj}-correlated uncertainties for our experiment are given by the red band. The x_{Bj}-correlated uncertainties are largely target-independent and will only be shown for this target.

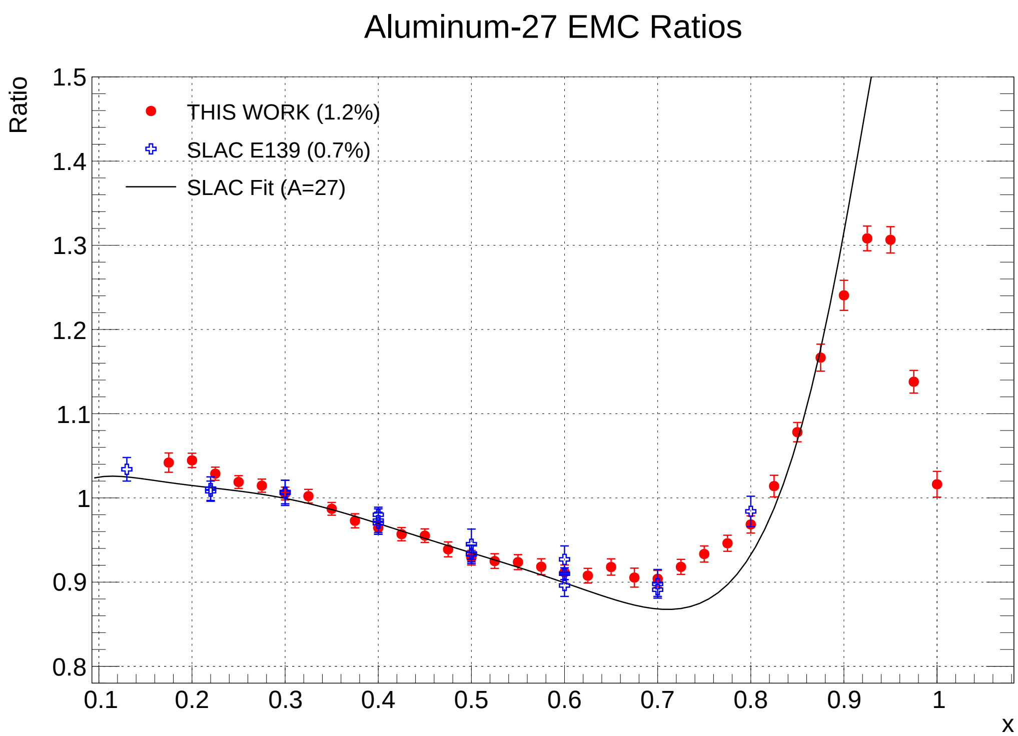

Figure 4.2: EMC ratios from this work for ^{27}Al are shown alongside a fit to the SLAC E139 results [23] and results from SLAC E139 (open blue plus signs) [23]. The normalization uncertainty of each of the experiments is shown in parentheses next to the experiment name in the legend.

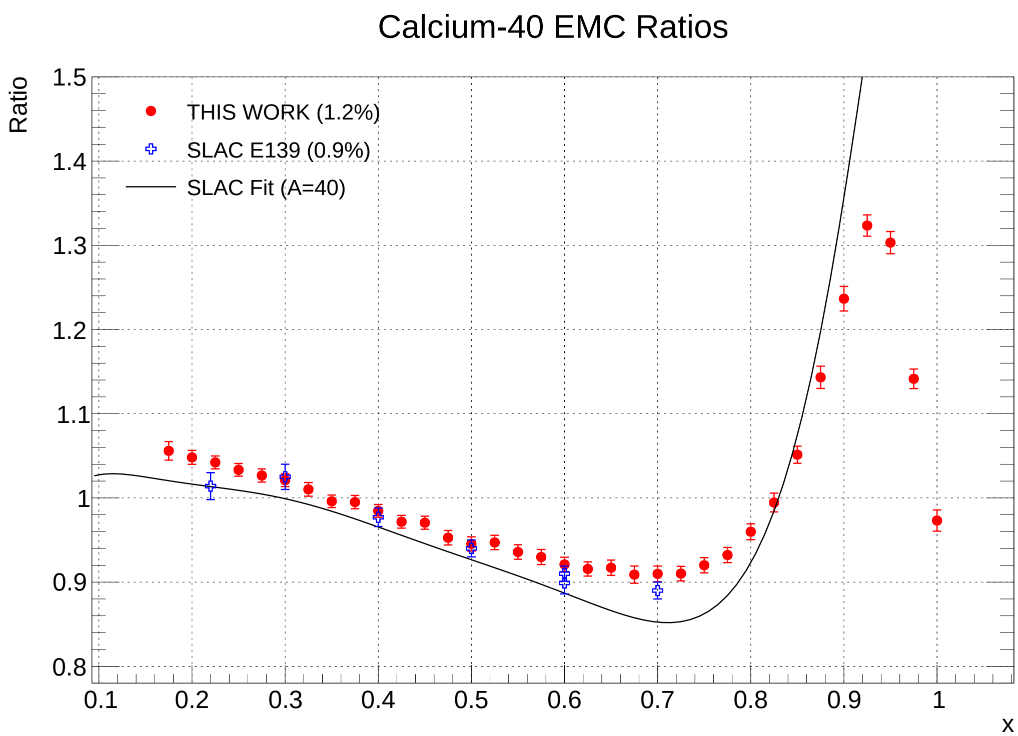

Figure 4.3: EMC ratios from this work for ^{40}Ca are shown alongside a fit to the SLAC E139 results [23] and results from SLAC E139 (open blue plus signs) [23]. The normalization uncertainty of each of the experiments is shown in parentheses next to the experiment name in the legend.

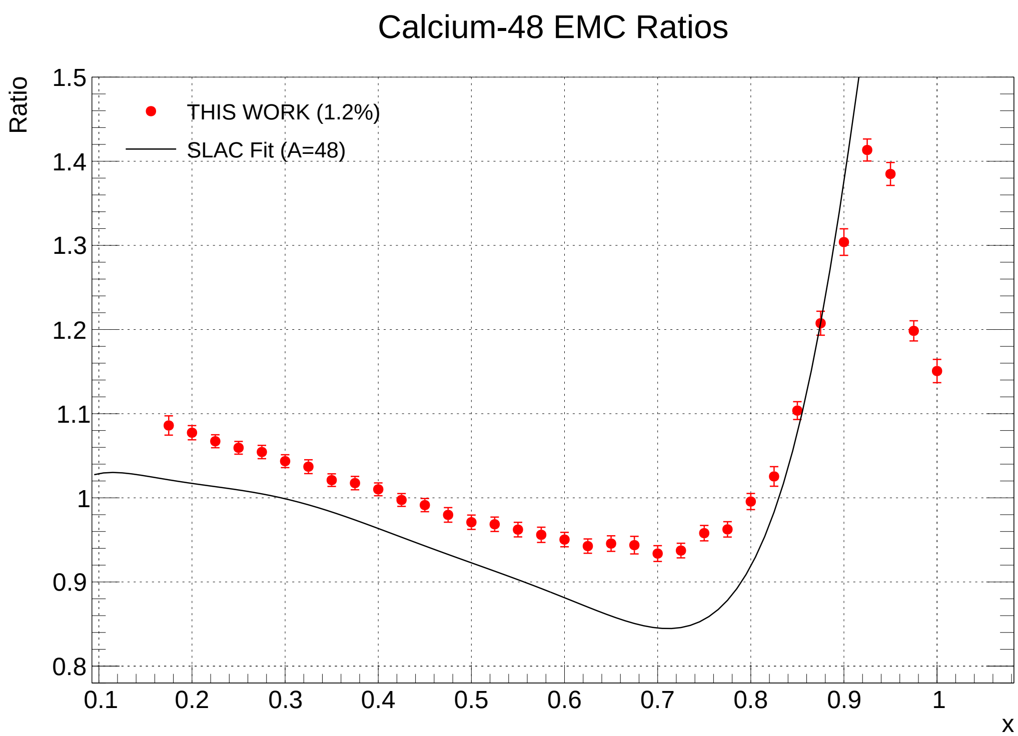

Figure 4.4: EMC ratios from this work for ^{48}Ca are shown alongside a fit to the SLAC E139 results [23]. The normalization uncertainty of our experiment is shown in parentheses next to the experiment name in the legend.

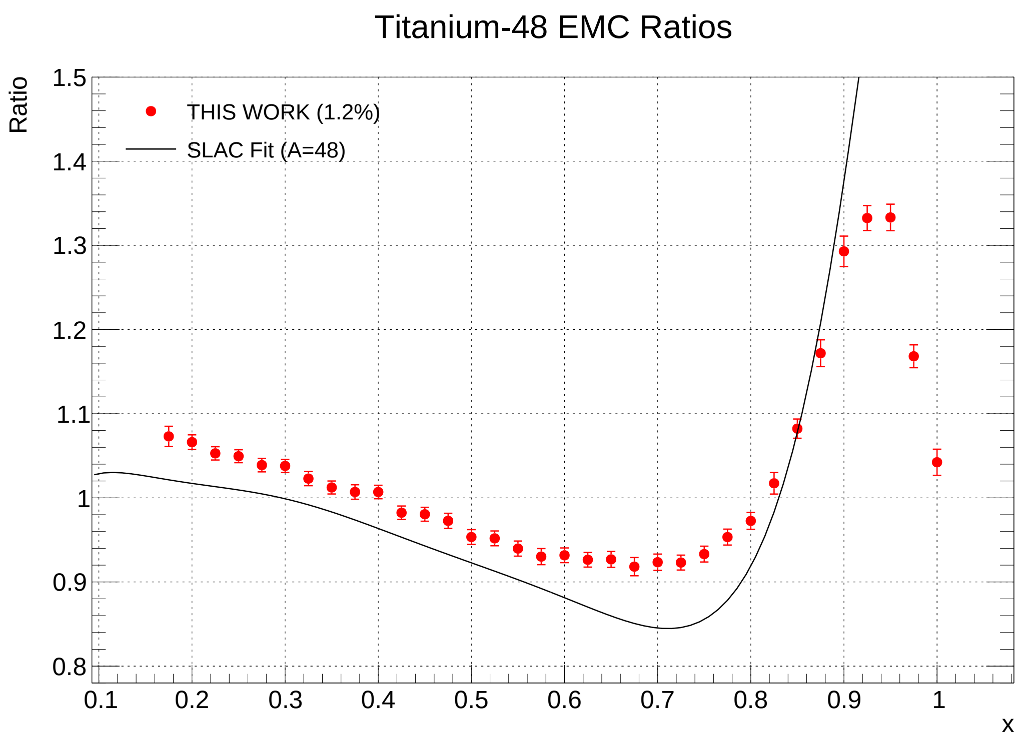

Figure 4.5: EMC ratios from this work for ^{48}Ti are shown alongside a fit to the SLAC E139 results [23]. The normalization uncertainty of our experiment is shown in parentheses next to the experiment name in the legend.

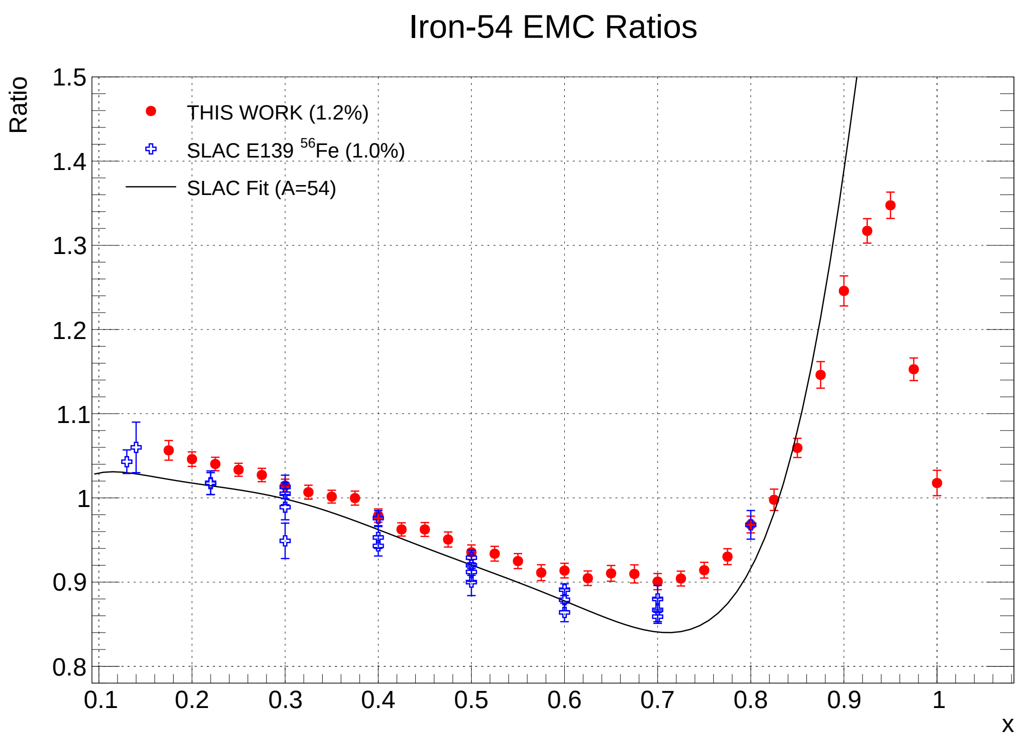

Figure 4.6: EMC ratios from this work for ^{54}Fe are shown alongside a fit to the SLAC E139 results [23] and ^{56}Fe results from SLAC E139 (open blue plus signs) [23]. The normalization uncertainty of each of the experiments is shown in parentheses next to the experiment name in the legend.

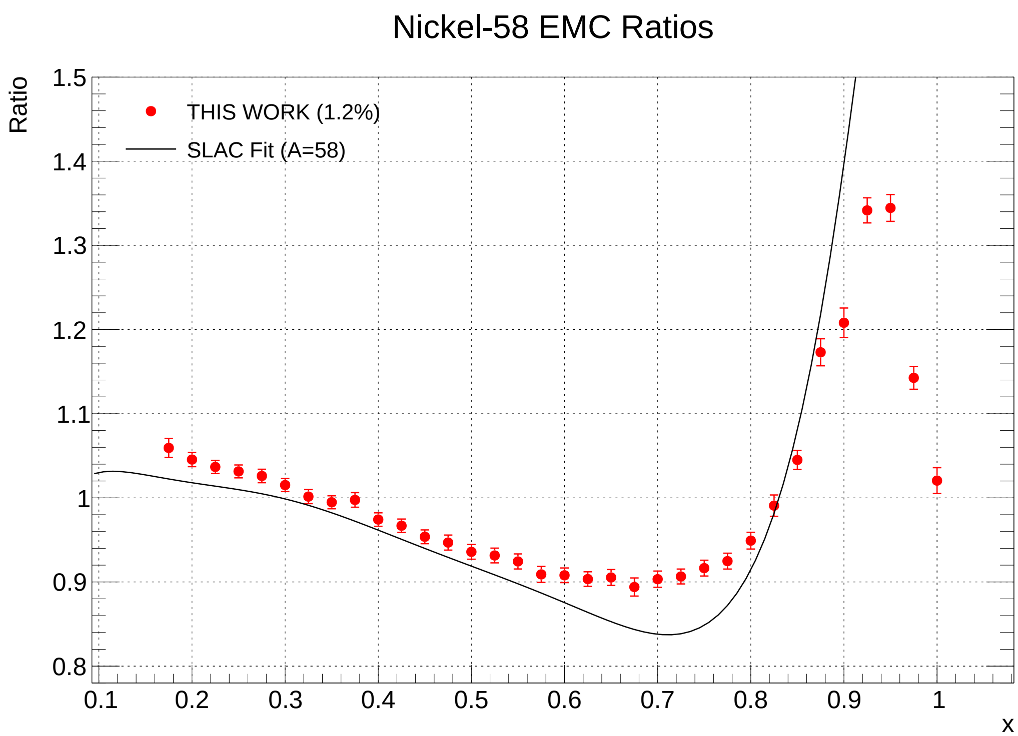

Figure 4.7: EMC ratios from this work for ^{58}Ni are shown alongside a fit to the SLAC E139 results [23]. The normalization uncertainty of our experiment is shown in parentheses next to the experiment name in the legend.

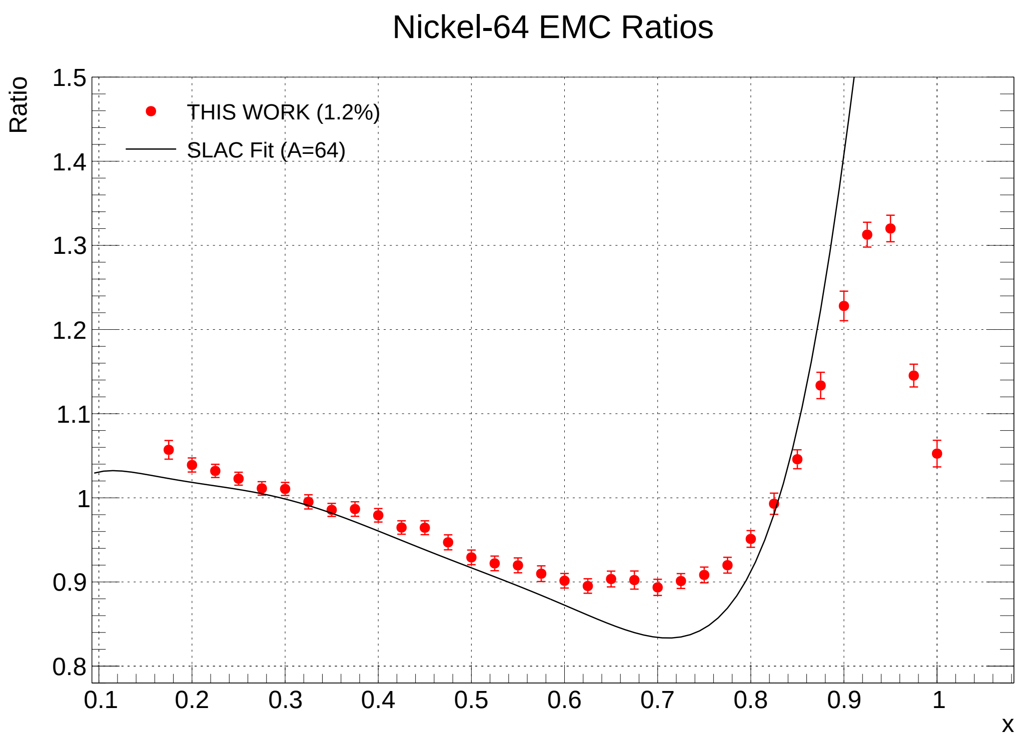

Figure 4.8: EMC ratios from this work for ^{64}Ni are shown alongside a fit to the SLAC E139 results [23]. The normalization uncertainty of our experiment is shown in parentheses next to the experiment name in the legend.

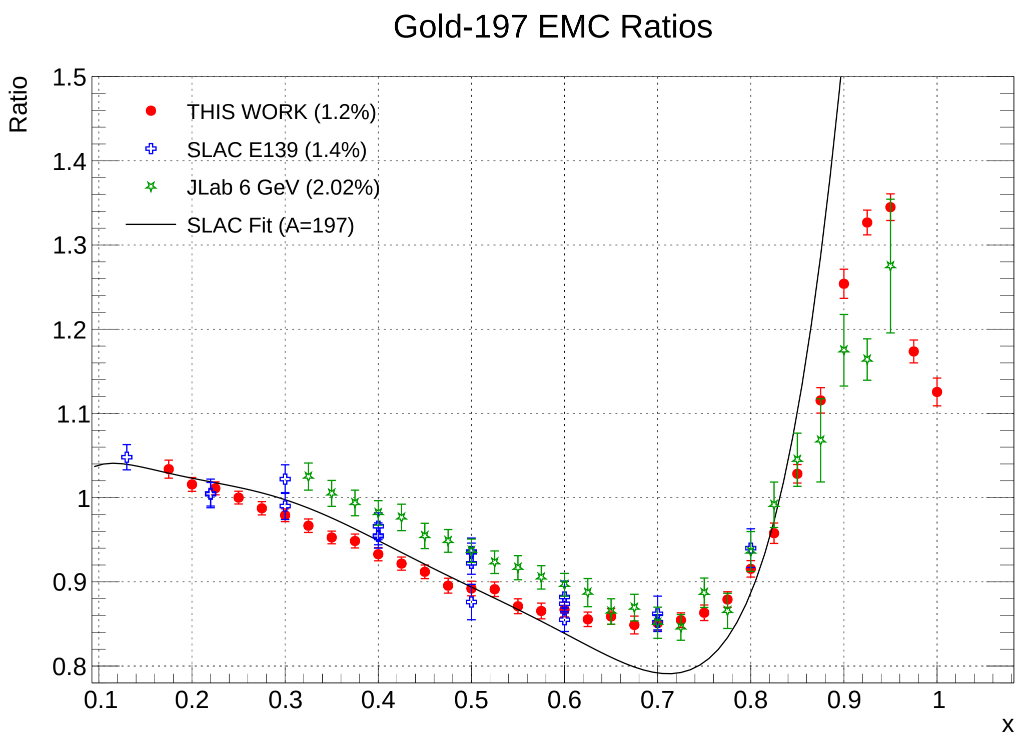

Figure 4.9: EMC ratios from this work for ^{197}Au are shown alongside a fit to the SLAC E139 results [23] and the results from JLab 6 GeV experiment (open green stars) [29] and SLAC E139 (open blue plus signs) [23]. The normalization uncertainty of each of the experiments is shown in parentheses next to the experiment name in the legend. While the SLAC E139 data agree reasonably well with this work, the JLab 6 GeV data appear to be systematically higher between $0.3 < x_{Bj} < 0.6$ before converging with our results at larger x_{Bj}.

While a couple of potential causes have already been investigated, the reason for this discrepancy remains unclear. Initially, the cross section model was considered to be a likely culprit, as early iterations of the model did not agree well with the measured data in certain kinematic regions. However, after several iterations of two different cross section models, the discrepancy remained, suggesting that it is not the source of the issue. The impact of the charge-symmetric background (CSB) was also studied, as the CSB correction did not account for the increase in the pion background above the Cherenkov detector's pion threshold. However, the impact of this on the measured cross section ratio is only a few tenths of a percent, an order of magnitude smaller than the observed discrepancy. In addition, this impact was already accounted for in the error budget. Therefore, the CSB was also determined not to be the cause.

There are several other reasons why this discrepancy may be occurring. It may be an effect of the HMS magnets saturating at large field settings ($E' > 5$ GeV). If this is the case, this could be checked by comparing the results from the data collected using the HMS detector to those from the SHMS detector, which has a dipole magnet that is nominally able to operate at higher field settings without saturation, optics data available at higher momenta, and which also took limited data sets at EMC effect kinematics for comparison with the results from the HMS detector. The initial detector calibrations for the SHMS detector have not yet been completed, which has prevented this study from being performed up to this point. If it is found that the results extracted from the SHMS data agree with the HMS results, then it is unlikely that the HMS magnet saturation is the cause of the discrepancy. Another possibility is that this observation is due to a previously unnoticed Q^2 dependence of the EMC effect.

A summary of the EMC slopes determined from the analyzed data is provided in Tab. 4.1. These slopes have been extracted from linear fits of the EMC ratios performed over two different ranges: $0.3 < x_{Bj} < 0.7$, and $0.3 < x_{Bj} < 0.6$. The first is a standard range that has been used to quantify the EMC effect in previous experiments and analyses, and the second was selected due to the flattening of the EMC ratio in the range $0.6 < x_{Bj} < 0.7$ in our preliminary data.

Nucleus	EMC Slope (0.3–0.6)	EMC Slope (0.3–0.7)
^{12}C	0.266 ± 0.027	0.216 ± 0.017
^{27}Al	0.339 ± 0.028	0.269 ± 0.017
^{40}Ca	0.331 ± 0.027	0.291 ± 0.017
^{48}Ca	0.327 ± 0.028	0.280 ± 0.017
^{48}Ti	0.382 ± 0.029	0.313 ± 0.017
^{54}Fe	0.385 ± 0.028	0.314 ± 0.017
^{58}Ni	0.378 ± 0.029	0.316 ± 0.017
^{64}Ni	0.365 ± 0.028	0.314 ± 0.017
^{197}Au	0.414 ± 0.028	0.341 ± 0.017

Table 4.1: Preliminary EMC slopes from this work with total error bars. Slopes are extracted from a linear fit performed over two ranges: $0.3 < x_{Bj} < 0.6$ and $0.3 < x_{Bj} < 0.7$. The slopes from the fit over the larger range are systematically lower than the slopes from the fit over the smaller range because the cross section ratio flattens out over the range $0.6 < x_{Bj} < 0.7$.

4.2 A-Dependence of the EMC Effect

Now that the sizes of the EMC effect in several nuclei have been quantified, we can investigate how these results compare with various predictions to gain some insight into its underlying cause.

We will first look at the A-dependence of the EMC effect. It has been predicted that the size of the EMC effect should generally scale with $A^{-1/3}$ for heavy ($A > 12$) nuclei [89], and recent studies have found this prediction to hold surprisingly well, even for some lighter nuclei [42]. The argument for this scaling can be summarized by several key points. The density distributions of heavy nuclei have been found to have an approximately universal shape, and the density in the nuclear interior is relatively constant in these nuclei. The portion of the scattering cross section that comes from the interior of the nucleus then scales with A. The density of the surface of these nuclei also has an approximately universal shape. The portion of the scattering cross section that comes from the surface of the nucleus scales as R^2, or $A^{2/3}$. Dividing the individual interior and surface portions of the scattering cross section by A to obtain the per-nucleon cross section, we see that it should consist of a constant term plus a term that scales with $A^{-1/3}$ due to the surface contribution to the cross section, where the nuclear density is lower than in the interior. This argument does not hold for light nuclei because the nearly universal shape of the nuclear density distribution that is seen in heavy nuclei, which is essential to the argument described above, is not seen in lighter nuclei.

Figure 4.10 shows measurements of the size of the EMC effect in various nuclei as a function of $A^{-1/3}$. For nuclei measured in past experiments, our preliminary results are generally consistent within one to two standard deviations of the previous measurements. In addition, our preliminary results generally support the conclusion of previous analyses: that the EMC effect in heavy ($A > 12$) nuclei scales well with $A^{-1/3}$.

Given that the $A^{-1/3}$ dependence holds for arbitrarily heavy nuclei, we can perform a linear fit to the world EMC slope data for $A > 12$ nuclei as a function of $A^{-1/3}$ and extrapolate this fit to $A^{-1/3} = 0$ to find the EMC slope for a hypothetical infinitely heavy nucleus. Performing this fit and extrapolating to $A^{-1/3} = 0$, we find the EMC slope of a hypothetical infinitely heavy nucleus to be 0.537 ± 0.020, provided that the $A^{-1/3}$ scaling continues to hold.

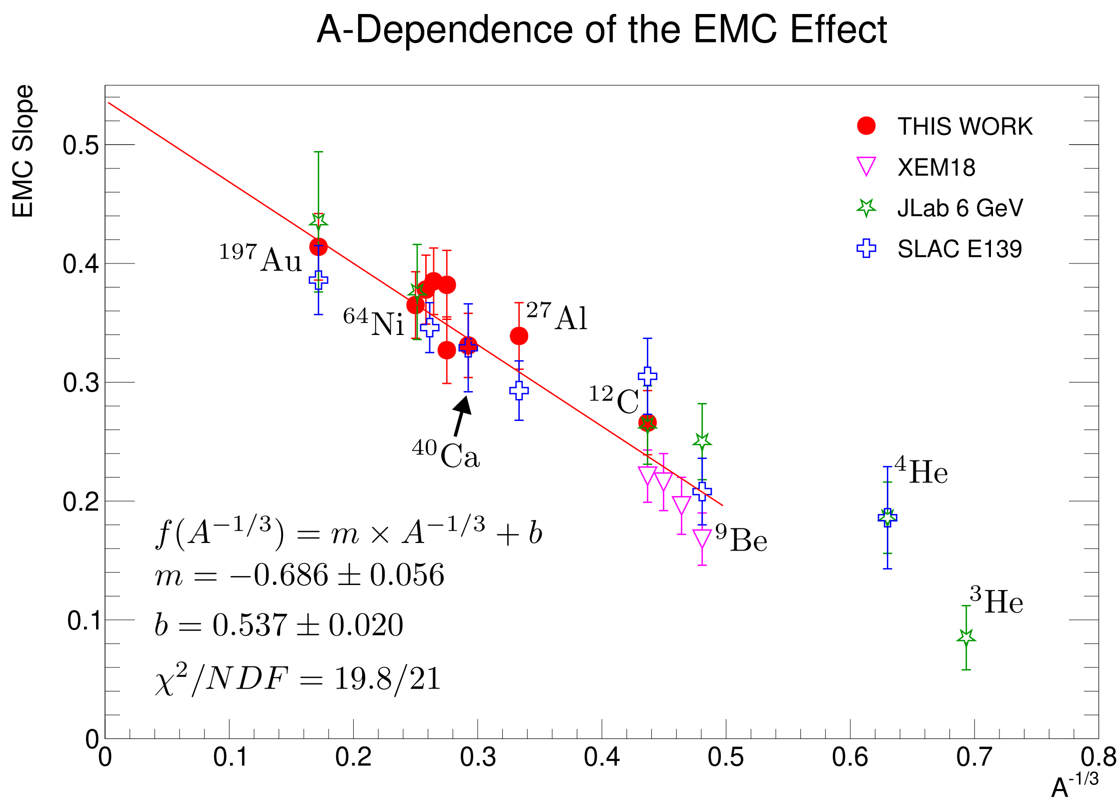

Figure 4.10: Measured EMC slopes of various nuclei shown as a function of $A^{-1/3}$. Preliminary EMC slopes from our experiment, E12-10-008, are determined from a linear fit of the EMC ratios over the range $0.3 < x_{Bj} < 0.6$, given in Tab. 4.1, while $0.3 < x_{Bj} < 0.7$ is the fit range used for the other data sets. Our preliminary results (closed red circles), are shown alongside results from the JLab 12 GeV commissioning data (open magenta triangles) [31], the JLab 6 GeV results (open green stars) [29], and the results from SLAC (open blue plus signs) [23]. The EMC slopes for the JLab 6 GeV and SLAC data are drawn from Ref. [30], while the 12 GeV commissioning results are drawn directly from the original publication [31]. The world data above $A \geqslant 9$ is fit, and results are shown in the bottom left corner of the plot.

4.3 Isospin-Dependence of the EMC Effect

Now we will investigate the isospin-dependence of the EMC effect, focusing on targets with mass numbers in the range $40 \leqslant A \leqslant 64$. As introduced in Sec. 1.6, a description of how isospin-dependent effects impact nuclear structure functions is essential to determining nuclear PDFs and reliably extracting fundamental quantities from measurements that depend on these PDFs; however, existing data are not sensitive to any potential isospin dependence. Our measurements, particularly those on the ^{40}Ca and ^{48}Ca targets, are the most sensitive to date for determining the isospin-dependence of the EMC effect.

Now, it is important to note that the extraction of the isospin dependence of the EMC effect is particularly sensitive to the F_2^n/F_2^p model used to determine the isoscalar corrections that are applied to the EMC ratios, which were discussed in Sec. 3.17. The preliminary results presented here use the F_2^n/F_2^p model including smearing in deuterium described in Ref. [85].

In an attempt to isolate the isospin dependence of the EMC effect, we naively hypothesize that the size of the EMC effect for nuclei with mass numbers in the range $40 \leqslant A \leqslant 64$ scales only with isospin and A. We then subtract the naive A-dependence of the EMC slopes from the measured values for each of our target nuclei. To determine this naive A-dependence, we fit our measured EMC slopes for ^{12}C and ^{40}Ca, the two isoscalar nuclei we studied, as a function of $A^{-1/3}$. For each target, we then subtract the value of the fit at the corresponding mass number A, leaving the residual EMC slope with the naive A-dependence removed. Figure. 4.11 presents our preliminary results for the size of the EMC effect in nuclei over the range $40 \leqslant A \leqslant 64$, with the naive A-dependence removed, plotted as a function of the neutron-to-proton ratio N/Z in these nuclei.

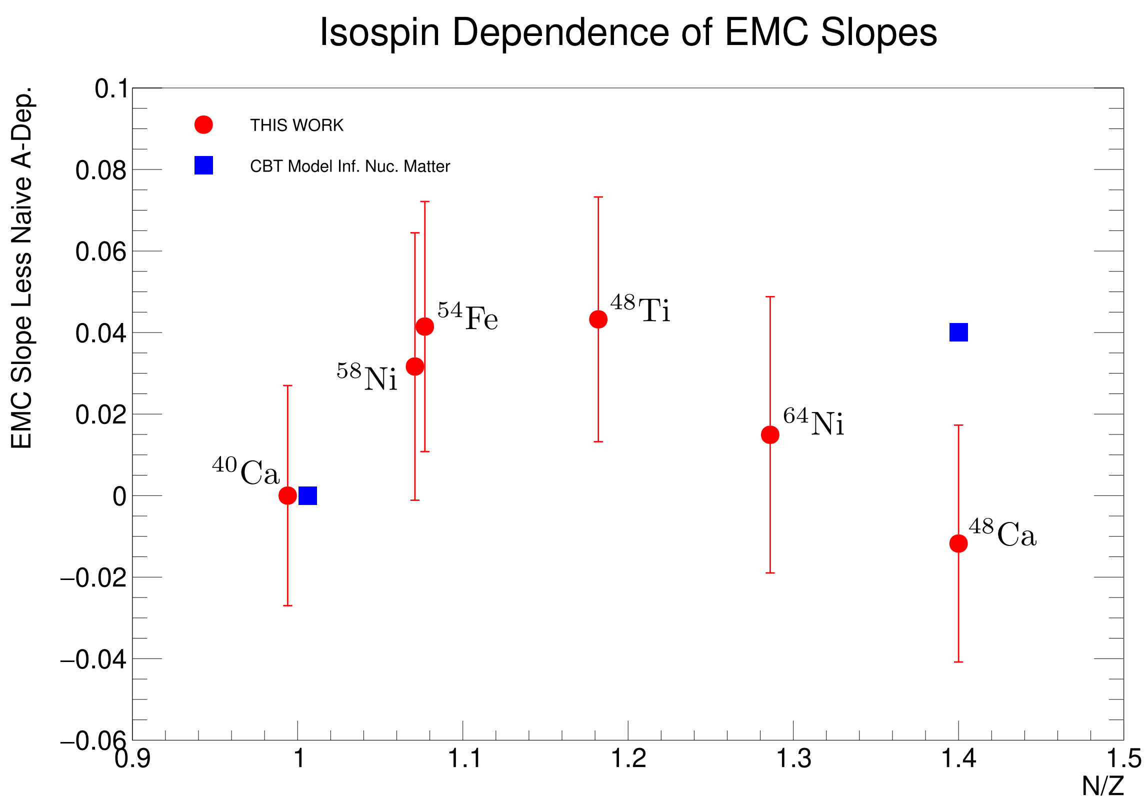

Figure 4.11: EMC slopes from this work determined from fits over the range $0.3 < x_{Bj} < 0.6$ with their naive A-dependence removed for nuclei with mass numbers in the range $40 \leqslant A \leqslant 64$ are plotted as a function of N/Z and shown alongside EMC slopes from fits over the same x_{Bj} range of theoretical predictions for $N/Z = 1$ and $N/Z = 1.4$ nuclear matter [90] from the CBT model described in Ref. [32].

The ^{40}Ca and ^{48}Ca targets provide the largest lever arm to measure isospin dependence, as they have very different neutron-to-proton ratios and similar numbers of nucleons. The observation that the EMC slopes of ^{40}Ca and ^{48}Ca are very similar suggests that the EMC effect does not have a significant isospin dependence. This conclusion is further supported by the similarity between the slopes of ^{58}Ni and ^{64}Ni. However, if the EMC effect is only A-dependent with no isospin-dependence at all, it is then difficult to explain the difference between the measured EMC slopes of the ^{48}Ca and ^{48}Ti targets, as they have the same number of nucleons. This may suggest that some other property of these nuclei, apart from A and isospin, has an effect on the size of the EMC effect in these nuclei. Alternatively, it is possible that isospin dependence of the EMC effect causes it to increase with N/Z until ^{54}Fe and ^{48}Ti ($N/Z \simeq 1.15$) before turning over and decreasing as N/Z increases. In the CBT model, such a turnover is expected, though it is predicted to occur around $N/Z \simeq 1.66$ [32].

The precision of these results could be improved by taking the cross section ratio of the $A > 40$ targets directly with ^{40}Ca, removing the additional uncertainty introduced by the cryogenic ^{2}H target. Additional studies are needed to draw stronger conclusions about the exact nature of the isospin dependence of the EMC effect, though these preliminary findings do not seem to indicate that the EMC effect has significant isospin dependence.

4.4 Future Directions

The experiment described in this dissertation, E12-10-008, studied the EMC effect via measurements of inclusive DIS cross sections. Alongside the results presented here, which focus on the isospin-dependence of the EMC effect, data for the additional targets listed in Tabs. 2.4 and 2.5 and at 26.00° and 35.00° have been collected and are being analyzed in parallel. In addition, there are several proposed experiments that will use methods other than inclusive, unpolarized DIS to study the EMC effect. Here, I will highlight a few of the EMC effect-related measurements that have been proposed at Jefferson Lab.

An experiment utilizing the CLAS12 spectrometer [91] in Hall B of Jefferson Lab is proposed that plans to make the first measurements of the spin-dependent EMC effect [92]. This is accomplished using a polarized ^{7}LiD target, where it is presently understood that almost all of the spin of the ^{7}Li is carried by a single proton. One can then extract the modification of that polarized proton rather than the average over all of the nucleons in that nucleus.

There is an experimental proposal that leverages the Solenoidal Large Intensity Device (SoLID) [93] to study the isospin dependence of the EMC effect through measurements of the parity-violating electroweak asymmetry A_{PV} in DIS (PVEMC) [94]. SoLID is a planned large-acceptance, high-luminosity spectrometer that is currently under development. Provided continued funding, SoLID is expected to be installed in Hall A of Jefferson Lab following the Super Bigbite Spectrometer (SBS) [95] and Measurement Of a Lepton-Lepton Electroweak Reaction (MOLLER) [96] experimental programs.

The main observable of the PVEMC experiment is the parity-violating electroweak asymmetry A_{PV} of electron DIS off a ^{48}Ca target, defined as

$$A_{PV} = \frac{\sigma_R - \sigma_L}{\sigma_R + \sigma_L} = \frac{G_F Q^2}{4\sqrt{2}\pi\alpha}[Y_1 \cdot a_1(x_{Bj}) + Y_3(y) \cdot a_3(x_{Bj})] \ , \tag{4.1}$$

where σ_R and σ_L are the scattering cross sections for right-handed and left-handed electrons, G_F is the Fermi constant, α is the Sommerfeld constant, $Y_{1(3)}$ are kinematic factors, and $a_{1(3)}$ are related to the nuclear PDF of ^{48}Ca [94]. The isospin-dependent EMC effect would affect the x_{Bj}-dependence of value a_1, see Fig. 4.12 for projected uncertainties for this experiment compared with several models. Therefore, measuring A_{PV} of ^{48}Ca will provide insight into the isospin-dependence of the EMC effect.

4.5 Conclusion

In conclusion, we have presented preliminary EMC ratios from data collected by the HMS during experiment E12-10-008 for ^{12}C, ^{27}Al, ^{40}Ca, ^{48}Ca, ^{48}Ti, ^{54}Fe, ^{58}Ni, ^{64}Ni,

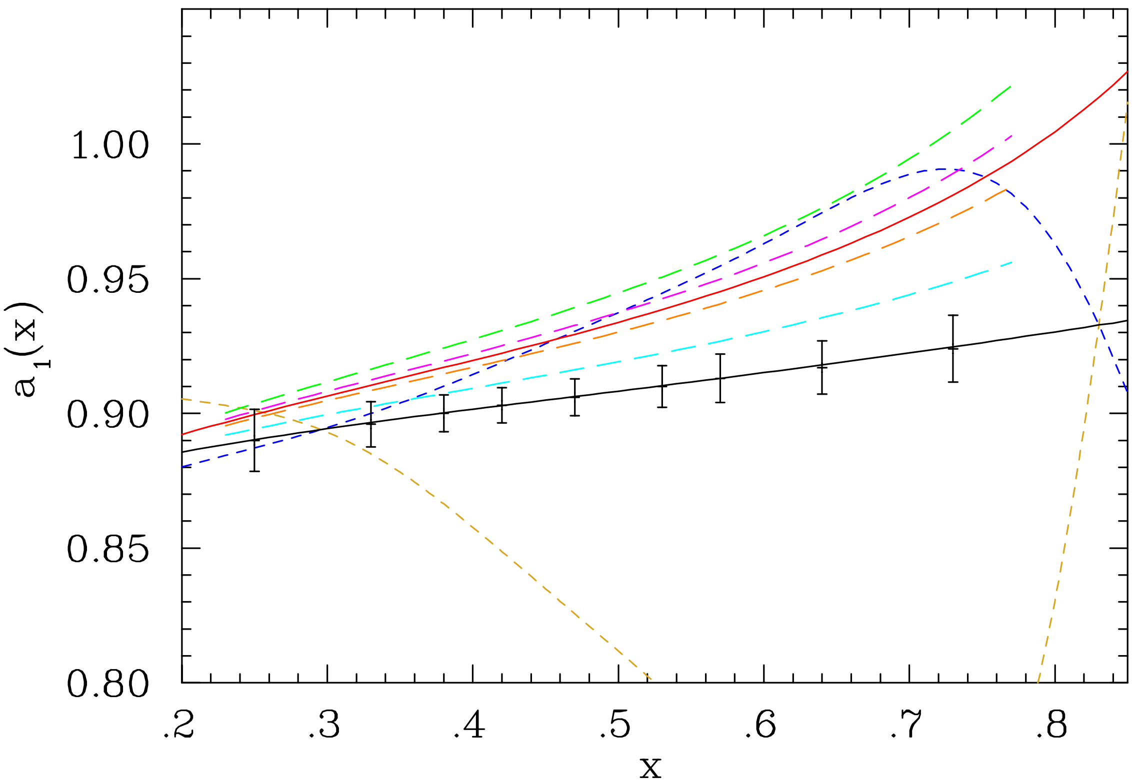

Figure 4.12: Figure from [94]. Projected uncertainties for the SoLID PVEMC experiment are shown alongside models that predict an isospin-dependent EMC effect. The solid black line is the SLAC E139 fit [23], which is isospin-independent. The solid red line is the prediction from the CBT model [32]. The other model curves are described in Ref. [94].

and ^{197}Au in the kinematic range $0.18 < x_{Bj} < 1.0$ and $2.8 < Q^2 < 8.1$ GeV^2. EMC slopes have been extracted to quantify the size of the EMC effect in these nuclei, and the A and isospin dependencies of this effect have been studied by parameterizing the EMC slopes as functions of $A^{-1/3}$ and the neutron-to-proton ratio N/Z.

Our preliminary results do not appear to indicate significant isospin-dependence of the EMC effect, though a more careful study is needed once all results are confirmed. In addition, we find the EMC effect scales reasonably well with $A^{-1/3}$ for $A \geqslant 9$ nuclei. Once the SHMS data is analyzed, it will be interesting to see if the flattening-out of the EMC ratio between $0.6 < x_{Bj} < 0.7$ that is seen in the 20.00° HMS data is also observed, or if the depletion of the EMC ratio continuous to $x_{Bj} \approx 0.7$ as found in previous measurements. In the latter case, it is likely that the flattening-out observed in the HMS data is due to saturation of HMS's magnets at high momenta. Otherwise, if the HMS and SHMS data are found to yield consistent results, it is possible that this flattening of the EMC ratio is a genuine feature of the EMC effect in our Q^2 range that has gone unnoticed thus far.

Additional data are needed to elucidate the exact nature of the EMC effect and its isospin dependence. This will be accomplished as the SHMS data and additional HMS data collected during E12-10-008 are analyzed, and other planned measurements are carried out, including those using the SoLID and CLAS12 spectrometers in Halls A and B of Jefferson Lab.

Bibliography

[1] J. J. Aubert et al. "The ratio of the nucleon structure functions F_2^n for iron and deuterium". In: *Phys. Lett. B* 123 (1983), pp. 275–278. DOI: 10.1016/0370-2693(83)90437-9.

[2] D. Gaskell et al. *Detailed studies of the nuclear dependence of F_2 in light nuclei.* 2009. URL: http://www.jlab.org/exp_prog/proposals/10/PR12-10-008.pdf.

[3] X. Zheng. "Precision Measurement of Neutron Spin Asymmetry A$_1^n$ at Large xbj Using CEBAF at 5.7 GeV". PhD thesis. Massachusetts Inst. of Technology (MIT), Cambridge, MA (United States), 2002. DOI: 10.2172/824895.

[4] E. D. Bloom et al. "High-Energy Inelastic e p Scattering at 6-Degrees and 10-Degrees". In: *Phys. Rev. Lett.* 23 (1969), pp. 930–934. DOI: 10.1103/PhysRevLett.23.930.

[5] M. Breidenbach et al. "Observed behavior of highly inelastic electron-proton scattering". In: *Phys. Rev. Lett.* 23 (1969), pp. 935–939. DOI: 10.1103/PhysRevLett.23.935.

[6] J. D. Bjorken. "Asymptotic Sum Rules at Infinite Momentum". In: *Phys. Rev.* 179 (1969), pp. 1547–1553. DOI: 10.1103/PhysRev.179.1547.

[7] S. Dasu et al. "Measurement of kinematic and nuclear dependence of $R = \sigma_L/\sigma_T$ in deep inelastic electron scattering". In: *Phys. Rev. D* 49 (1994), pp. 5641–5670. DOI: 10.1103/PhysRevD.49.5641.

[8] L. H. Tao et al. "Precision measurement of $R = \sigma_L/\sigma_T$ on hydrogen, deuterium and beryllium targets in deep inelastic electron scattering". In: *Z. Phys. C* 70 (1996), pp. 387–390. DOI: 10.1007/s002880050117.

[9] P. Solvignon, D. Gaskell, and J. Arrington. "Coulomb Distortion in the Inelastic Regime". In: *AIP Conf. Proc.* 1160.1 (2009). Ed. by L. Elouadrhiri et al., pp. 155–159. DOI: 10.1063/1.3232024. arXiv: 0906.0512 [nucl-ex].

[10] L. L. Frankfurt and M. I. Strikman. "QCD and Short Range Nuclear Phenomena". In: *Nucl. Phys. B* 181 (1981), pp. 22–60. DOI: 10.1016/0550-3213(81)90505-8.

[11] G. Berlad, A. Dar, and G. Eilam. "A Quark-parton Model of Nuclear Production". In: *Phys. Rev. D* 22 (1980), p. 1547. DOI: 10.1103/PhysRevD.22.1547.

[12] A. Bodek and J. L. Ritchie. "Fermi Motion Effects in Deep Inelastic Lepton Scattering from Nuclear Targets". In: *Phys. Rev. D* 23 (1981), p. 1070. DOI: 10.1103/PhysRevD.23.1070.

[13] J. Ashman et al. "Measurement of the Ratios of Deep Inelastic Muon - Nucleus Cross-Sections on Various Nuclei Compared to Deuterium". In: *Phys. Lett. B* 202 (1988), pp. 603–610. DOI: 10.1016/0370-2693(88)91872-2.

[14] G. Bari et al. "A Measurement of Nuclear Effects in Deep Inelastic Muon Scattering on Deuterium, Nitrogen and Iron Targets". In: *Phys. Lett. B* 163 (1985), p. 282. DOI: 10.1016/0370-2693(85)90238-2.

[15] M. Arneodo et al. "Accurate measurement of F_2^d/F_2^p and $R^d - R^p$". In: *Nucl. Phys. B* 487 (1997), pp. 3–26. DOI: 10.1016/S0550-3213(96)00673-6. arXiv: hep-ex/9611022.

[16] P. Amaudruz et al. "Precision measurement of the structure function ratios F_2^{He}/F_2^D, F_2^C/F_2^D and F_2^{Ca}/F_2^D". In: *Z. Phys. C* 51 (1991), pp. 387–394. DOI: 10.1007/BF01548560.

[17] P. Amaudruz et al. "Precision measurement of structure function ratios for ^{6}Li, ^{12}C and ^{40}Ca". In: *Z. Phys. C* 53 (1992), pp. 73–78. DOI: 10.1007/BF01483873.

[18] P. Amaudruz et al. "A Reevaluation of the nuclear structure function ratios for D, He, ^{6}Li, C and Ca". In: *Nucl. Phys. B* 441 (1995), pp. 3–11. DOI: 10.1016/0550-3213(94)00023-9. arXiv: hep-ph/9503291.

[19] M. Arneodo et al. "The A dependence of the nuclear structure function ratios". In: *Nucl. Phys. B* 481 (1996), pp. 3–22. DOI: 10.1016/S0550-3213(96)90117-0.

[20] A. Bodek et al. "Electron Scattering from Nuclear Targets and Quark Distributions in Nuclei". In: *Phys. Rev. Lett.* 50 (1983), p. 1431. DOI: 10.1103/PhysRevLett.50.1431.

[21] A. Bodek et al. "A Comparison of the Deep Inelastic Structure Functions of Deuterium and Aluminum Nuclei". In: *Phys. Rev. Lett.* 51 (1983), p. 534. DOI: 10.1103/PhysRevLett.51.534.

[22] R. G. Arnold et al. "Measurements of the A-Dependence of Deep Inelastic electron Scattering from Nuclei". In: *Phys. Rev. Lett.* 52 (1984), p. 727. DOI: 10.1103/PhysRevLett.52.727.

[23] J. Gomez et al. "Measurement of the A-dependence of deep inelastic electron scattering". In: *Phys. Rev. D* 49 (1994), pp. 4348–4372. DOI: 10.1103/PhysRevD.49.4348.

[24] K. Ackerstaff et al. “Nuclear effects on $R = \sigma_L/\sigma_T$ in deep inelastic scattering”. In: *Phys. Lett. B* 475 (2000). [Erratum: Phys.Lett.B 567, 339–346 (2003)], pp. 386–394. DOI: 10.1016/S0370-2693(99)01493-8. arXiv: hep-ex/9910071.

[25] A. Airapetian et al. “Measurement of $R = \sigma_L/\sigma_T$ in deep inelastic scattering on nuclei”. In: (Oct. 2002). arXiv: hep-ex/0210068.

[26] J. Arrington et al. “Low Q scaling, duality, and the EMC effect”. In: *Phys. Rev. C* 73 (2006), p. 035205. DOI: 10.1103/PhysRevC.73.035205. arXiv: nucl-ex/0307012.

[27] A. C. Benvenuti et al. “Nuclear Effects in Deep Inelastic Muon Scattering on Deuterium and Iron Targets”. In: *Phys. Lett. B* 189 (1987), pp. 483–487. DOI: 10.1016/0370-2693(87)90664-2.

[28] F. Gross and S. Liuti. “Role of nuclear binding in the EMC effect”. In: *Phys. Rev. C* 45 (1992), pp. 1374–1381. DOI: 10.1103/PhysRevC.45.1374.

[29] J. Seely et al. “New measurements of the EMC effect in very light nuclei”. In: *Phys. Rev. Lett.* 103 (2009), p. 202301. DOI: 10.1103/PhysRevLett.103.202301. arXiv: 0904.4448 [nucl-ex].

[30] J. Arrington et al. “Measurement of the EMC effect in light and heavy nuclei”. In: *Phys. Rev. C* 104.6 (2021), p. 065203. DOI: 10.1103/PhysRevC.104.065203. arXiv: 2110.08399 [nucl-ex].

[31] A. Karki et al. “First Measurement of the EMC effect in ^{10}B and ^{11}B”. In: *Phys. Rev. C* 108.3 (2023), p. 035201. DOI: 10.1103/PhysRevC.108.035201. arXiv: 2207.03850 [nucl-ex].

[32] I. C. Cloet, W. Bentz, and A. W. Thomas. “Isovector EMC effect explains the NuTeV anomaly”. In: *Phys. Rev. Lett.* 102 (2009), p. 252301. DOI: 10.1103/PhysRevLett.102.252301. arXiv: 0901.3559 [nucl-th].

[33] Y. Nambu and G. Jona-Lasinio. “Dynamical Model of Elementary Particles Based on an Analogy with Superconductivity. 1.” In: *Phys. Rev.* 122 (1961). Ed. by T. Eguchi, pp. 345–358. DOI: 10.1103/PhysRev.122.345.

[34] Y. Nambu and G. Jona-Lasinio. “Dynamical model of elementary particles based on an analogy with superconductivity. II.” In: *Phys. Rev.* 124 (1961). Ed. by T. Eguchi, pp. 246–254. DOI: 10.1103/PhysRev.124.246.

[35] G. P. Zeller et al. “A Precise Determination of Electroweak Parameters in Neutrino Nucleon Scattering”. In: *Phys. Rev. Lett.* 88 (2002). [Erratum: Phys.Rev.Lett. 90, 239902 (2003)], p. 091802. DOI: 10.1103/PhysRevLett.88.091802. arXiv: hep-ex/0110059.

[36] R. Schiavilla et al. “Tensor Forces and the Ground-State Structure of Nuclei”. In: *Phys. Rev. Lett.* 98 (2007), p. 132501. DOI: 10.1103/PhysRevLett.98.132501. arXiv: nucl-th/0611037.

[37] L. L. Frankfurt et al. “Evidence for short range correlations from high Q^2 (e, e-prime) reactions”. In: *Phys. Rev. C* 48 (1993), pp. 2451–2461. DOI: 10.1103/PhysRevC.48.2451.

[38] K. S. Egiyan et al. “Measurement of 2- and 3-nucleon short range correlation probabilities in nuclei”. In: *Phys. Rev. Lett.* 96 (2006), p. 082501. DOI: 10.1103/PhysRevLett.96.082501. arXiv: nucl-ex/0508026.

[39] N. Fomin et al. "New measurements of high-momentum nucleons and short-range structures in nuclei". In: *Phys. Rev. Lett.* 108 (2012), p. 092502. DOI: 10.1103/PhysRevLett.108.092502. arXiv: 1107.3583 [nucl-ex].

[40] L. B. Weinstein et al. "Short Range Correlations and the EMC Effect". In: *Phys. Rev. Lett.* 106 (2011), p. 052301. DOI: 10.1103/PhysRevLett.106.052301. arXiv: 1009.5666 [hep-ph].

[41] O. Hen, E. Piasetzky, and L. B. Weinstein. "New data strengthen the connection between Short Range Correlations and the EMC effect". In: *Phys. Rev. C* 85 (2012), p. 047301. DOI: 10.1103/PhysRevC.85.047301. arXiv: 1202.3452 [nucl-ex].

[42] J. Arrington et al. "A detailed study of the nuclear dependence of the EMC effect and short-range correlations". In: *Phys. Rev. C* 86 (2012), p. 065204. DOI: 10.1103/PhysRevC.86.065204. arXiv: 1206.6343 [nucl-ex].

[43] R. Subedi et al. "Probing Cold Dense Nuclear Matter". In: *Science* 320 (2008), pp. 1476–1478. DOI: 10.1126/science.1156675. arXiv: 0908.1514 [nucl-ex].

[44] D. de Florian et al. "Global Analysis of Nuclear Parton Distributions". In: *Phys. Rev. D* 85 (2012), p. 074028. DOI: 10.1103/PhysRevD.85.074028. arXiv: 1112.6324 [hep-ph].

[45] H. Paukkunen and C. A. Salgado. "Compatibility of neutrino DIS data and global analyses of parton distribution functions". In: *JHEP* 07 (2010), p. 032. DOI: 10.1007/JHEP07(2010)032. arXiv: 1004.3140 [hep-ph].

[46] H. Paukkunen and C. A. Salgado. "Agreement of Neutrino Deep Inelastic Scattering Data with Global Fits of Parton Distributions". In: *Phys. Rev. Lett.*

110.21 (2013), p. 212301. DOI: 10.1103/PhysRevLett.110.212301. arXiv: 1302.2001 [hep-ph].

[47] I. Schienbein et al. “PDF Nuclear Corrections for Charged and Neutral Current Processes”. In: *Phys. Rev. D* 80 (2009), p. 094004. DOI: 10.1103/PhysRevD.80.094004. arXiv: 0907.2357 [hep-ph].

[48] K. Kovarik et al. “Nuclear Corrections in Neutrino-Nucleus DIS and Their Compatibility with Global NPDF Analyses”. In: *Phys. Rev. Lett.* 106 (2011), p. 122301. DOI: 10.1103/PhysRevLett.106.122301. arXiv: 1012.0286 [hep-ph].

[49] K. F. Muzakka et al. “Compatibility of neutrino DIS data and its impact on nuclear parton distribution functions”. In: *Phys. Rev. D* 106.7 (2022), p. 074004. DOI: 10.1103/PhysRevD.106.074004. arXiv: 2204.13157 [hep-ph].

[50] S. Kulagin and R. Petti. “Global study of nuclear structure functions”. In: *Nucl. Phys. A* 765 (2006), pp. 126–187. DOI: 10.1016/j.nuclphysa.2005.10.011. arXiv: hep-ph/0412425.

[51] S. Kulagin and R. Petti. “Neutrino inelastic scattering off nuclei”. In: *Phys. Rev. D* 76 (2007), p. 094023. DOI: 10.1103/PhysRevD.76.094023. arXiv: hep-ph/0703033.

[52] M. Hirai, S. Kumano, and T. -H. Nagai. “Determination of nuclear parton distribution functions and their uncertainties in next-to-leading order”. In: *Phys. Rev. C* 76 (2007), p. 065207. DOI: 10.1103/PhysRevC.76.065207. arXiv: 0709.3038 [hep-ph].

[53] J. Arrington et al. *Inclusive Scattering from Nuclei at $x > 1$ in the quasielastic and deeply inelastic regimes.* 2006. URL: http://www.jlab.org/exp_prog/proposals/06/PR12-06-105.pdf.

[54] C. W. Leemann, D. R. Douglas, and G. A. Krafft. "The Continuous Electron Beam Accelerator Facility: CEBAF at the Jefferson Laboratory". In: *Ann. Rev. Nucl. Part. Sci.* 51 (2001), pp. 413–450. DOI: 10.1146/annurev.nucl.51.101701.132327.

[55] Hall C Staff and Users. *2019 Version: Jefferson Lab Hall C Standard Equipment Manual*. 2023. URL: https://hallcweb.jlab.org/safety-docs/current/Standard-Equipment-Manual.pdf.

[56] R. Kazimi et al. "Operational Results of Simultaneous Four-Beam Delivery at Jefferson Lab". In: *10th International Particle Accelerator Conference*. 2019, WEPMP053. DOI: 10.18429/JACoW-IPAC2019-WEPMP053.

[57] K. B. Unser. "The Parametric current transformer: A Beam current monitor developed for LEP". In: *AIP Conf. Proc.* 252 (1992). Ed. by W. Barry and P. Kloeppel, pp. 266–275. DOI: 10.1063/1.42124.

[58] J. R. Arrington. "Inclusive Electron Scattering From Nuclei at $x > 1$ and High Q^2". PhD thesis. California Institute of Technology, 1998. eprint: nucl-ex/0608013.

[59] Saint-Gobain Crystals. *BC-400,BC-404,BC-408,BC-412,BC-416 Premium Plastic Scintillators*. 2008. URL: https://www.hep.phy.cam.ac.uk/~lester/teaching/SparkChamber/SGC_BC400_404_408_412_416_Data_Sheet.pdf.

[60] M. E. Christy et al. *SHMS Drift Chambers*. Hall C Reference. 2016. URL: https://hallcweb.jlab.org/document/howtos/shms_drift_chambers.pdf.

[61] L. Tang et al. *HMS Drift Chambers*. Hall C Reference. 2017. URL: http://hallcweb.jlab.org/document/howtos/hms_drift_chambers.pdf.

[62] C. Grupen and B. Shwartz. *Particle Detectors*. 2nd. Cambridge University Press, 2008. ISBN: 978-0-521-84006-4.

[63] H. Mkrtchyan et al. "The lead-glass electromagnetic calorimeters for the magnetic spectrometers in Hall C at Jefferson Lab". In: *Nucl. Instrum. Meth. A* 719 (2013), pp. 85–100. DOI: 10.1016/j.nima.2013.03.070. arXiv: 1204.6413 [physics.ins-det].

[64] Jefferson Lab Data Acquisition Support Group. *CODA Documentation*. 2024. URL: https://coda.jlab.org/.

[65] Jefferson Lab. *FADC250 User's Manual*. URL: https://hallcweb.jlab.org/document/vendor_manuals/FADC250UsersManual.pdf.

[66] CAEN. *V1190-VX1190 A/B Multihit TDCs*. Revision 13. 2012. URL: https://hallcweb.jlab.org/document/vendor_manuals/V1190_REV13.pdf.

[67] *EPICS Documentation*. 2024. URL: https://www.jlab.org/accelerator/controls/epics.

[68] D. Meekins. *Hall C Target Configuration Novemeber 28, 2022*. 2022. URL: https://logbooks.jlab.org/entry/4112532.

[69] Z. Wolters. *BCM Calibrations*. 2023. URL: https://hallcweb.jlab.org/elogs/X%3E1+%26+EMC/223.

[70] Z. Wolters. *BCM Gains and Offsets Chi Squared Test*. 2023. URL: https://hallcweb.jlab.org/elogs/X%3E1+%26+EMC/229.

[71] C. Morean. "Short Range Correlation measurements in the quasielastic region with an 11 GeV beam". PhD thesis. University of Tennessee, Knoxville, 2023.

[72] Hall C Staff and Users. *simc_gfortran*. https://github.com/JeffersonLab/simc_gfortran. 2024.

[73] R. J. Corruccini and J. J. Gniewek. *Thermal Expansion of Technical Solids at Low Temperatures: A Compilation From the Literature*. National Bureau of Standards, 1961.

[74] V. Tvaskis. "Longitudinal - Transverse Separation of Deep-Inelastic Scattering at Low Q^2 on Nucleons and Nuclei". PhD thesis. Amsterdam U., 2004. DOI: 10.2172/915446.

[75] P. E. Bosted and V. Mamyan. "Empirical Fit to electron-nucleus scattering". In: (Mar. 2012). arXiv: 1203.2262 [nucl-th].

[76] C. Maieron, T. W. Donnelly, and I. Sick. "Extended superscaling of electron scattering from nuclei". In: *Phys. Rev. C* 65 (2002), p. 025502. DOI: 10.1103/PhysRevC.65.025502. arXiv: nucl-th/0109032.

[77] D. Biswas et al. "New Measurements of the Deuteron to Proton F_2 Structure Function Ratio". In: (Sept. 2024). arXiv: 2409.15236 [hep-ex].

[78] L. W. Mo and Y.-S. Tsai. "Radiative Corrections to Elastic and Inelastic e p and mu p Scattering". In: *Rev. Mod. Phys.* 41 (1969), pp. 205–235. DOI: 10.1103/RevModPhys.41.205.

[79] Sridhara Rao Dasu. "Precision Measurment of x, Q^2 and A-Dependence of $R = \sigma_L/\sigma_T$ and F_2 in Deep Inelastic Scattering". PhD thesis. University of Rochester, 1988.

[80] A. Aste, C. von Arx, and D. Trautmann. "Coulomb distortion of relativistic electrons in the nuclear electrostatic field". In: *Eur. Phys. J. A* 26 (2005), pp. 167–178. DOI: 10.1140/epja/i2005-10169-0. arXiv: nucl-th/0502074.

[81] A. Aste and J. Jourdan. "Improved effective momentum approximation for quasielastic (e,e-prime) scattering off highly charged nuclei". In: *EPL* 67 (2004), pp. 753–759. DOI: 10.1209/epl/i2004-10113-x. arXiv: nucl-th/0403075.

[82] I. Sick. "Zemach moments of ^{3}He and ^{4}He". In: *Phys. Rev. C* 90.6 (2014), p. 064002. DOI: 10.1103/PhysRevC.90.064002. arXiv: 1412.2603 [nucl-ex].

[83] N. Fomin, D. Gaskell, W. Henry, et al. *Measurement of Deep Inelastic Scattering from Nuclei with Electron and Positron Beams to Constrain the Impact of Coulomb Corrections in DIS*. 2023. URL: https://www.jlab.org/exp_prog/proposals/23/PR12+23-003.pdf.

[84] Hall C Staff and Users. *mc-single-arm*. https://github.com/JeffersonLab/mc-single-arm. 2024.

[85] J. Arrington et al. "Neutron Structure Functions". In: *J. Phys. G* 36 (2009), p. 025005. DOI: 10.1088/0954-3899/36/2/025005. arXiv: 0805.3116 [nucl-th].

[86] S. Li et al. "Extraction of the neutron F_2 structure function from inclusive proton and deuteron deep-inelastic scattering data". In: *Phys. Rev. D* 109.7 (2024), p. 074036. DOI: 10.1103/PhysRevD.109.074036. arXiv: 2309.16851 [hep-ph].

[87] D. Abrams et al. "Measurement of the Nucleon F_2^n/F_2^p Structure Function Ratio by the Jefferson Lab MARATHON Tritium/Helium-3 Deep Inelastic Scattering Experiment". In: *Phys. Rev. Lett.* 128.13 (2022), p. 132003. DOI: 10.1103/PhysRevLett.128.132003. arXiv: 2104.05850 [hep-ex].

[88] A. Karki. "Precise measurement of the nuclear dependence of the EMC effect in light nuclei". PhD thesis. Mississippi State University, 2022.

[89] I. Sick and D. Day. “The EMC effect of nuclear matter”. In: *Phys. Lett. B* 274 (1992), pp. 16–20. DOI: 10.1016/0370-2693(92)90297-H.

[90] Ian Cloet. *Private Communication*. 2013.

[91] V. D. Burkert et al. “The CLAS12 Spectrometer at Jefferson Laboratory”. In: *Nucl. Instrum. Meth. A* 959 (2020), p. 163419. DOI: 10.1016/j.nima.2020.163419.

[92] W. K. Brooks, S. Kuhn, et al. *The EMC Effect in Spin Structure Functions*. 2014. URL: https://www.jlab.org/exp_prog/proposals/14/PR12-14-001.pdf.

[93] J. Arrington et al. “The solenoidal large intensity device (SoLID) for JLab 12 GeV”. In: *J. Phys. G* 50.11 (2023), p. 110501. DOI: 10.1088/1361-6471/acda21. arXiv: 2209.13357 [nucl-ex].

[94] J. Arrington et al. *First Measurement of the Flavor Dependence of Nuclear PDF Modification Using Parity-Violating Deep Inelastic Scattering*. 2022. URL: https://misportal.jlab.org/pacProposals/proposals/1757/attachments/152040/Proposal.pdf.

[95] *Super Bigbite Spectrometer*. URL: http://hallaweb.jlab.org/12GeV/SuperBigBite/.

[96] J. Benesch et al. “The MOLLER Experiment: An Ultra-Precise Measurement of the Weak Mixing Angle Using Moller Scattering”. In: (Nov. 2014). arXiv: 1411.4088 [nucl-ex].